
Site U1388¹

Expedition 339 Scientists²

Chapter contents

Background and objectives	1
Operations	2
Lithostratigraphy	3
Biostratigraphy	6
Paleomagnetism	8
Physical properties	9
Geochemistry	11
Stratigraphic correlation	12
References	13
Figures	16
Tables	55

Background and objectives

Integrated Ocean Drilling Program (IODP) Site U1388 (36°16.142'N; 6°47.648'W) is located on an extensive sandy sheeted drift of the proximal sector (Sector 1; proximal scour and ribbons sectors defined by Hernández-Molina et al., 2003, and Llave et al., 2007) of the contourite depositional system (CDS) close to the Gibraltar Gateway (Figs. F1, F2, F3). This site represents an opportunity for recovering part of the late Pliocene and Pleistocene succession close to the gateway in order to identify key paleoceanographic changes in Mediterranean Outflow Water (MOW) and to evaluate the influence of the gateway. Site U1388 is 6.5 km southwest of the oil company exploratory well MPC-1 (dry well), where samples older than Quaternary were recovered in 1982.

This sector is located in the southeastern area between Cádiz and the Strait of Gibraltar and is characterized by a smooth contourite terrace oriented alongslope between 500 and 800 meters below sea level (mbsl) (Figs. F1, F2; see also Fig. F15 in the “Expedition 339 summary” chapter [Expedition 339 Scientists, 2013a]). It was first described by Kenyon and Belderson (1973) and later by Nelson et al. (1993), Habgood (2002), and Habgood et al. (2003), all of whom consider it as the proximal part of the CDS. It is an extensive area (~100 km long and 30 km wide) dominated by an abrasional surface with high backscatter intensity (Fig. F2).

Several erosive scour alignments with a northwest–southeast orientation, smooth V-shaped expression, and truncated reflectors are evident in seismic profiles (Fig. F4). In the northwest part of this sector, distinct depositional features at the surface include a sequence of longitudinal bedforms (also oriented northwest–southeast), ripple marks, sand ribbons, and sediment waves (Kenyon and Belderson, 1973; Nelson et al., 1993; Hanquiez et al., 2007).

Oil company data show an exceptionally thick (~815 m) sandy sheeted drift (see Fig. F15 in the “Expedition 339 summary” chapter [Expedition 339 Scientists, 2013a]) composed of sand-rich horizons that average 12–15 m in thickness (Buitrago et al., 2001) intercalated with finer grained sediments. In addition, a sand bank was identified by Akhmetzhanov et al. (2002) and Akhmetzhanov (2003) at the southeast boundary of this sector.

The Gibraltar Gateway has a very special role in Mediterranean–Atlantic water mass exchange, which is associated with the high-

¹Expedition 339 Scientists, 2013. Site U1388. In Stow, D.A.V., Hernández-Molina, F.J., Alvarez Zarikian, C.A., and the Expedition 339 Scientists, *Proc. IODP, 339*: Tokyo (Integrated Ocean Drilling Program Management International, Inc.). doi:10.2204/iodp.proc.339.106.2013

²Expedition 339 Scientists' addresses.



est bottom current velocities known anywhere in the study region (nearly 300 cm/s). This is also one of the most important oceanic gateways worldwide, enabling overflow and circulation of MOW to the Atlantic Ocean (e.g., Serra, 2004; Legg et al., 2009; Serra et al., 2010). The proximal sector within the CDS of the Gulf of Cádiz results from MOW generating strong and turbulent bottom currents, which contour the slope between 300 and 1000 mbsl (Kenyon and Belderson, 1973; Habgood et al., 2003; Hernández-Molina et al., 2003, 2006, 2011). Its velocity decreases from a maximum of 240 cm/s immediately west of the Gibraltar Gateway to ~75–100 cm/s near the northern end of the Cádiz sand sheet (Fig. F5). Beneath the highest velocity zone there is a broad abrasional surface and erosive scours, but as current velocity decreases, sand ribbons and wave fields develop. MOW divides into an upper and lower core at the northwest end of this sector, as described by Madelain (1970).

Objectives

The major objective for Site U1388 was to recover a sedimentary contourite record for the late Pliocene to the Holocene deposited under the influence of the overflow of MOW close to the Gibraltar Gateway (Stow et al., 2011b). This record will allow us to investigate

- The influence of the Gibraltar Gateway through the Pliocene and Pleistocene,
- MOW paleoceanography and its global climate significance, and
- The effects of long- and short-term climate and sea level changes on the sediment architecture of the contourite drift.

Specific objectives for Site U1388 include

- Drilling through the sheeted drift succession and into late Pliocene sediments and hence dating the most important intervals for sandy contourite sedimentation in the Gulf of Cádiz;
- Evaluating the nature of change in the patterns of sedimentation and microfauna from the late Pliocene through the Holocene;
- Documenting the possible effects of the Gibraltar Gateway through the Pliocene and Pleistocene and hence determining the input variation of MOW influx;
- Reconstructing the main MOW paleoceanographic events for the Pliocene and Pleistocene and identifying the role of MOW in the dynamics of North Atlantic Deep Water;

- Focusing on the diagnostic criteria for sand-rich contourite deposits on sheeted drifts and the inferred environmental changes;
- Evaluating the correlation and influence of cold/warm periods with MOW variation;
- Determining the sedimentary stacking pattern of the sandy sheeted drift in relation to changes in sea level and other forcing mechanisms, thereby determining the potential role of variations in cross-sectional area of the Gibraltar Gateway;
- Evaluating periods of sheeted drift construction, nondeposition (hiatuses), and erosion;
- Evaluating the sandy contourite deposition in relation to sea level variation; and
- Calibrating and therefore understanding the sedimentary cyclicity evident on the sandy contourite deposits, thereby characterizing their sedimentary expression and regional extent.

In addition to these objectives, improved knowledge of sand-rich contourite deposits will have significant implications, both in the establishment of a facies model for sandy contourites (Stow and Faugères, 2008; Viana, 2008) as well as in consideration of their potential as a future deepwater hydrocarbon exploration target (Buitrago et al., 2001; Llave et al., 2005; Akhmetzhanov et al., 2007; Viana et al., 2007; Viana, 2008; Stow et al., 2011a; Brackenridge et al., 2011).

Operations

The 55 nmi transit from Site U1387 to Site U1388 (proposed Site GC-04D) was accomplished in ~5 h at an average speed of 11 kt. At 0745 h, 18 December 2011, the vessel was positioned on the new location.

The operations plan for Site U1388 called for advanced piston corer (APC)/extended core barrel (XCB)/rotary core barrel (RCB) coring in three holes and conducting downhole logging operations in Holes U1388B and U1388C. The first two holes were to be cored with the APC to refusal and then with the XCB to ~350 mbsf. The third hole was to be cored with the RCB from 350 to 1300 meters below seafloor (mbsf). Ultimately, three holes were drilled (Table T1), but the coring objectives were not achieved because of hardware failure caused by a difficult sandy formation. In Hole U1388A, APC Core 339-U1388A-1H advanced only 3.4 m (107.6% recovery) because a thick sand layer at the sediment surface prevented the core from penetrating any further. Hole U1388B was cored using the XCB to 225.7 mbsf with 47.2% recovery. Hole U1388C was drilled

without coring to 205 mbsf and then cored using the RCB to 229 mbsf. Overall recovery at Site U1388 was 120.54 m (47.6%): 3.64 m (107.6% recovery) with the APC, 106.54 m (47.2% recovery) with the XCB, and 10.36 m (43.17% recovery) with the RCB. The site was terminated earlier than planned because of formation instability.

Hole U1388A

An APC/XCB bottom-hole assembly (BHA) with a 9/8 inch polycrystalline diamond bit, lockable float valve, seal bore drill collar, and nonmagnetic drill collar was assembled and deployed. Following a 1.3 h underwater camera survey of the seafloor over a 30 m grid pattern, Hole U1388A was spudded with the APC at 1500 h. The calculated seafloor depth from the recovery of the first core was 675.1 meters below rig floor (mbrf; 663.6 mbsl), which was 0.7 m deeper than the corrected depth given by the precision depth recorder. The second attempt at a piston core appeared to be an incomplete stroke. The core winch operator spent ~3 h attempting to recover the stuck core barrel. The Kinley cutter was deployed to cut the coring line above the sinker bars when it was not possible to jar off the core barrel. The only course of action remaining was to recover the drill string and extricate the core barrel on the surface. The drill string was retrieved by 2400 h, 18 December. The reason why the core barrel couldn't be recovered was obvious; most of the BHA was full of sand that apparently "U-tubed" when the driller advanced into the formation to position the bit for the next piston core (2H).

Hole U1388B

The BHA was cleared of sand and deployed to 669.9 mbrf. The vessel offset 20 m east of the previous hole. The underwater camera displayed what appeared to be man-made debris on the seafloor and precipitated another 10 m offset to the east. The strategy for the second hole of the site was to core an XCB hole to depth and use the information acquired from that pilot hole to assess if and where the APC could be deployed in subsequent holes. The driller tagged seafloor at 674.4 mbrf (662.9 mbsl) at 0645 h. The camera system was recovered, and the top drive was picked up. Hole U1388B was spudded with the XCB at 0835 h, 19 December, and advanced to 225.7 mbsf by 0745 h, 20 December. While coring this interval, extensive cutting shoe damage suggested that the distribution of fluid flow between the cutting shoe and the polycrystalline diamond bit was not optimum for this formation. Rather than continue coring in this fashion and considering that the objectives of this site were deeper in the formation,

XCB coring was terminated at 225.7 mbsf. The average recovery for this hole was 47.2%. The driller pumped a 5 bbl slug of heavy mud prior to making a connection for Cores 1X through 12X (110.9 mbsf) to avoid a recurrence of the sand backflowing into the BHA. A 20 bbl sepiolite flush was made at 216.1 mbsf. The drill string was pulled clear of the seafloor at 0925 h and on deck at 1155 h, 20 December.

Hole U1388C

A four-stand RCB BHA with a new CC-4 Rock Bit International bit and mechanical bit release was made up and run in to 668.0 mbrf. After a short underwater camera survey confirmed that the location of the hole was clear of debris, the driller tagged the seafloor at 674.0 mbrf (662.5 mbsl). The underwater camera was recovered, the top drive was picked up, and Hole U1388C was spudded with the RCB at 1915 h, 20 December. The hole was washed to 205.0 mbsf, where rotary coring was initiated. At 119.8 and 167.6 mbsf, 20 bbl Hi-Vis mud sweeps were circulated. Rotary coring advanced from 205.0 to 229.0 mbsf, where the drill string became firmly stuck in the formation with no rotation and limited circulation. The drill string required 1.5 h to free the pipe utilizing overpulls of as much as 120,000 lb and adjusting rotary current limits as high as 1050 A. Once the pipe came free, more mud (both Hi-Vis and 10.5 ppg) was pumped to clear out some of the sand that had collapsed on the BHA. The drill string was pulled free of the seafloor at 1330 h and on deck by 1725 h, 21 December. The formation was considered too unstable to safely core, and the decision was made to move to the next planned site of the expedition. Total time at Site U1388 was 3.2 days, which was 10 days less than the allotted time. The vessel departed for Site U1389 at 1730 h, 21 December.

Lithostratigraphy

Drilling at Site U1388 penetrated a ~225 m thick sedimentary section with significant variations in recovery among the three holes drilled (Figs. F6, F7). The shipboard lithostratigraphic program involved detailed visual logging of all archive sections, visual assessment of sediment color, petrographic analysis of smear slides (no shipboard thin sections were created), and X-ray diffraction (XRD) analysis of 22 powdered bulk samples and 6 clay fraction samples. Bulk XRD samples generally were taken once per core, and the clay fractions of those samples were analyzed once per four cores. Sediment from Holes U1388A–U1388C was sampled regularly for smear slides during visual core descriptions. Hand-drawn logs showing the recovered sediment sequence, in-

cluding the distribution and structure of bedding, are included in the DRAWLOG folder in **“Supplementary material.”**

Total carbonate content of these cores, based on shipboard analyses, ranges from 18 to 30.1 wt%, with an average of 25.1 wt% assuming that all inorganic carbon was calcium carbonate (Fig. F8). These results are consistent with abundances of biogenic and detrital carbonate estimated from smear slides, so lithologic names determined from smear slide analysis have been used without modification through this text, the accompanying summary diagrams, and the visual core description sheets.

The sediments recovered in all three holes at Site U1388 are considered to represent a single lithologic unit. Because of hole stability problems and the presence of sandy sediment, however, not all of Unit I was fully sampled. Following core recovery problems after Core 339-U1388A-1A (see **“Operations”**), Hole U1388B was spudded with the XCB and recovery was generally poor until Core 339-U1388B-12X. Drilling in Hole U1388C used rotary drilling to recover sediments that overlapped with the base of Hole U1388B.

The sediment at Site U1388 is classified as one lithologic unit (Fig. F7). Unit I is a Holocene to Pleistocene sequence (see **“Biostratigraphy”**) with interbedded nannofossil mud, mud with biogenic carbonate, silty mud with biogenic carbonate, silty sand with biogenic carbonate, sandy silt with biogenic carbonate, and sand. The thickest sand bed (3.64 m) is at the sediment surface (all of Core 339-U1388A-1H) and is primarily fine sand with shell fragments; however, grain size approaches coarse sand to granule-grade in horizons where shell fragments are common. Most of the coarser beds recovered deeper in the section are silty muds, muddy sands, and silty sands. These are predominantly medium to thick bedded with occasional very thick beds (the thickest observed is ~7.5 m thick). In contrast, the finer sediments are muds with biogenic carbonate.

The character of sediment physical properties, including natural gamma radiation (NGR), magnetic susceptibility, color reflectance parameters, and density, records the distribution of these various lithologies and sediment components (see **“Physical properties”**). Characteristics of the sedimentary sequence cored at Site U1388, together with some of these additional properties, are summarized in Figure F9.

Unit I description

Intervals: 339-U1388A-1H-1, 0 cm, through 1H-CC, 61 cm; 339-U1388B-1H-1, 0 cm, through

24X-CC, 36 cm; 339-U1388C-2R-1, 0 cm, through 4R-1, 88 cm

Depths: Hole U1388A = 0–3.64 mbsf (bottom of hole [BOH]), Hole U1388B = 0–225.73 mbsf (BOH), Hole U1388C = 205–224.98 mbsf (BOH)

Age: Holocene–Pleistocene

Lithologies and bedding

The major lithologies in Unit I are silty mud with biogenic carbonate, silty sand with biogenic carbonate, and mud with biogenic carbonate. Secondary lithologies are calcareous sand and sand with biogenic carbonate; sandy silt and sandy mud, both with biogenic carbonate; and nannofossil mud and calcareous silty mud. Most of Unit I contains 10–25 wt% carbonate, although some coarser sandy layers contain >25 wt% carbonate because of abundant shell fragments.

Uncertainty about the lithologies of the unrecovered intervals has implications for the ability to define lithologic units and subunits at Site U1388. Sandy beds (including calcareous sand, sand with biogenic carbonate, silty sand with biogenic carbonate, sandy silt with biogenic carbonate, and sandy mud with biogenic carbonate) and silty beds (including silty mud with biogenic carbonate) form ~75% of the sediment recovered above ~100 mbsf and ~25% of the sediment recovered below that level (Figs. F7, F10). However, the overall rate of sediment recovery was much lower above ~100 mbsf, so the sandy and silty beds that were recovered average 15%–20% of the total depth intervals cored below ~5 mbsf. We attribute the poor recovery at this site to the use of XCB coring in unconsolidated sands, but note that our interpretation of the lithologic sequence would change if the unrecovered sediments above 100 mbsf are different from the sediments recovered by coring in that interval. Sandy units are quite difficult to recover using the XCB because there is no closure on the bottom of the pipe, so this part of the section would be quite coarse if all unrecovered sediments above 100 mbsf are sandy. However, if all the unrecovered sediment in this hole was mud (weakly consolidated muds are also difficult to recover using XCB coring), then the percentage of sandy and silty beds relative to total thickness cored would be nearly identical at 17.4% above 100 mbsf and 16.7% below 100 mbsf (Fig. F10). Although the latter may not be a likely scenario, we are forced to conclude that it is not possible to divide Unit I based on visual observations of the recovered sediment alone. Additional studies will be needed to determine whether Unit I can be further divided.

The coarsest bed in Unit I is the ~3.64 m thick bed of fine sand recovered in Core 339-U1388A-1H. This

bed has layers of coarse sand to granules, with shell debris, at intervals 339-U1388A-1H-1, 139–148 cm; 1H-2, 111–116 cm; 1H-3, 0–13 cm; and 1H-3, 20–30 cm. Sediment in Holes U1388B and U1388C is not as coarse as that in Hole U1388A, with the coarsest beds in Holes U1388B and U1388C described as silty sand. As sampled in Holes U1388B and U1388C, Unit 1 predominantly is medium to thick bedded, with some coarse-grained beds as thick as ~7.5 m. The finer grained beds are muds with biogenic carbonate and range in thickness from ~0.5 to >15 m. The contacts between lithologies are generally gradational and bioturbated, although some of the coarser grained beds have sharp to erosional lower contacts.

Structures and texture

Only Core 339-U1388A-1H was recovered by APC. All cores in Hole U1388B were recovered by XCB and as such have been biscuited to some extent, thus obscuring sedimentary structures. Shell fragments are common in coarser grained layers, especially in many of the coarser beds (e.g., Sections 339-U1388B-7X-1A and 339-U1388A-1H-2A), perhaps related to the movement of large bedforms.

Normally graded and inversely graded beds are present in Unit I. Many of the coarser beds have gradational upper and lower contacts, exhibit bi-gradational bedding, and are considered to be of contourite origin. Figure F11 shows a typical silty contourite, 24 cm thick, in Section 339-U1388B-13X-3. Another typical bi-gradational sequence is present in Core 339-U1388B-23X that is ~3.5 m thick and also interpreted as a contourite. Other beds exhibit normal grading and sharp to erosional lower contacts (Fig. F12) and are interpreted as turbidites. Beds with inverse grading are also present (Figs. F13, F14, F15) and generally are medium to thick to very thick bedded. These reverse-graded beds exhibit a variety of upper and lower contacts, ranging from erosional to gradational. Because of this variability in contact type, the deposition of these beds is most likely a result of current activity. In general, the contacts between other beds also range from sharp to gradational and bioturbated, but it is not generally clear whether biscuiting had occurred at those contacts.

Parallel laminated sands are present in interval 339-U1388B-20X-5, 50–105 cm (Fig. F16), formed by alternating lighter and darker laminations each 2–6 mm thick. The principal difference between the light and dark sand laminations appears to be a lower mud content in the light-colored sands. We interpret these as primary parallel laminations formed by currents, although the role of drilling disturbance in their formation is not known.

Deposits originating from sediment failure are also noted at this site. A possible debrite is identified at interval 339-U1388B-10X-2, 41–121 cm, and a possible slump is identified at interval 339-U1388B-24X-5, 33–54 cm (Fig. F17). These deformed, thinly bedded sediments have inclined contacts between muddy and sandy intervals, as well as possible muddy intraclasts in a more sandy matrix.

An analysis of the number of contourite and turbidite beds observed (Fig. F7) suggests that turbidite and contourite beds are distributed throughout the recovered section. The number of silt-dominated and sand-dominated beds per core shows some variation, with more beds per meter observed at ~120–140 mbsf (Cores 339-U1388B-14X and 15X). Sandy contourite beds are also somewhat more common in this depth range.

Burrows are common secondary sedimentary structures, although bioturbation is generally sparse to slight. In many cases, burrows have a sandy fill similar to the overlying or underlying bed. One possible subvertical burrow found near a lithologic contact is >1 cm wide and 28 cm long (interval 339-U1388B-6X-2, 7–35 cm) and is filled with clean medium-grained sand that is coarser than either the overlying or underlying unit.

Composition

The results of smear slide analysis showing sediment composition and grain size are given in Table T2. These observations indicate that detrital carbonate is more common in lithologies with intermediate grain sizes (silty sand, sandy silt, and silty mud) than in the finer (mud with nannofossils) or coarser grained sediments (sand). Biogenic silica is rarely observed. A diverse suite of minerals from a variety of source rocks is present in many samples (Fig. F18).

Several well-preserved gastropods are present in Unit I (Fig. F19). These species can be found living on the Iberian shelf today, but it is not certain if they can live in deeper water. However, the gastropods recovered at this site were found in a variety of lithologies—in a silty sand contourite, a mud, and the surface sand layer (Fig. F19, top, center and bottom, respectively)—suggesting that the shells were found in situ.

Color

Sediment colors are generally described as light to dark gray near the surface, greenish gray or grayish brown in Cores 339-U1388C-3R through 4R, and varying downhole between greenish gray, dark greenish gray, and very dark greenish gray. The most common color is dark greenish gray.

Bulk mineralogy

XRD analysis was conducted on 22 powdered bulk samples, which generally were taken once per core the first time a particular stratigraphic level was sampled. Six samples were analyzed for clay fraction mineralogy, chosen as a subset of the suite of bulk mineralogy samples (Table T3; Figs. F20, F21). The bulk XRD results indicate that the mineral composition varies considerably above ~50 mbsf and is somewhat more uniform through the rest of the cored interval. The samples at 2.6 mbsf in Hole U1388A (Sample 339-U1388A-1H-2, 115–116 cm) and 36.3 mbsf in Hole U1388B (Sample 339-U1388B-5X-CC, 31–32 cm) produce high-intensity peaks at characteristic angles for plagioclase, K-feldspar, and illite. Hornblende has peak intensities similar to those from other sites, and a sample at 138.7 mbsf in Hole U1388B has a fairly large intensity for a pyroxene (augite) peak. The sample processed for clay minerals at 2.65 mbsf in Hole U1388A is sandy and contains no clay minerals. Unglycolated samples from other depths show peaks for illite, kaolinite, and chlorite, as well as an elevated baseline between the chlorite and illite peaks. When glycolated, the baseline in this interval decreases and a more intense peak appears at lower angles on the diffractogram, indicating that poorly crystalline clays have expanded to the characteristic d-spacing of 17.8 Å, typical of smectite expanded with glycol.

Discussion

Unit I contains a significant number of sandy beds, with thicknesses up to several meters, as well as many intervals of mud with biogenic carbonate that exceed 15 m thick. The latter provide relatively good age control (see “[Biostratigraphy](#)”). Full understanding of sedimentation at this site is hampered by partial recovery. Based on the recovered material, however, both contourites and turbidites have been identified in relatively similar numbers, and both contourites and turbidites are distributed through the entire length of Unit I. These relatively similar abundances and stratigraphic distributions indicate that both alongslope and downslope processes were important for delivering sediment to Site U1388 throughout the time indicated by the cored record.

Some details in the record at Site U1388 do suggest that the relative importance of alongslope vs. downslope flow changed through time. For example, the number of contourite beds increases in Cores 339-U1388B-14X and 15X, possibly caused by changes in current strength at that time. Also, some intervals containing lighter colored sand laminae may indicate sediment reworking by currents and re-

moval of the fine fraction. The presence of two apparent mass transport units (a debrite and a slump) reinforce the importance of downslope transport.

Given the evidence for sustained activity of both alongslope currents and downslope processes, the possibility existed for numerous interactions between downslope and alongslope currents during deposition of Unit I. This range of interactions may help explain the irregular development of sharp contacts at the bases or tops of sandy sequences, as well as the deposition of inversely graded beds. Some normally graded and sharp-based (base-cut-out) beds could be also contourites, as in Site U1389 (see “[Lithostratigraphy](#)” for Site U1389 [Expedition 339 Scientists, 2013d]), and further detailed studies are necessary to differentiate them from turbidite beds. Several of the intervals investigated by optical and XRD techniques have relatively high percentages of rock-forming minerals other than quartz, suggesting an immature mineral assemblage and the possibility of relatively direct sediment supply to Site U1388 through downslope processes.

Biostratigraphy

Sediments recovered at Site U1388 include silty sands and sands (see “[Lithostratigraphy](#)”). Marine microfossil and nannofossil abundance was therefore lower than at the previous sites. Several samples are barren or almost barren, especially of foraminifers. Preservation, on the other hand, was often very good to good, with only few samples showing moderate preservation. A rare occurrence of pteropods was observed in Sample 339-U1388B-22X-CC. Ostracods were not studied at Site U1388, and only two samples from Hole U1388B were analyzed for pollen. The total pollen and spores concentrations were similar to those from previous Sites U1386 and U1387, ranging between 15,000 and 34,000 grains/cm³. The preservation was moderate to poor. Microcharcoal particles and dinocysts were also observed.

The deepest reliable biostratigraphic event is the last occurrence (LO) of *Pseudoemiliania lacunosa* (0.46 Ma), placed at 170 mbsf in Hole U1388B (Table T4). The estimated sedimentation rate between this nannofossil event and the one above is 60 cm/k.y. If this sedimentation rate is extrapolated to the base of Hole U1388B, the basal age is ~0.56 Ma, which is in good agreement with the absence of the benthic foraminifer “*Stilostomella* extinction” event occurring between 0.58 and 0.70 Ma. The Holocene/Pleistocene boundary could not be defined, but based on the planktonic foraminifer assemblage, Sample 339-U1388A-1H-CC likely dates from the Holocene.

Calcareous nannofossils

We examined all the core catcher samples from Holes U1388A–U1388C for calcareous nannofossil biostratigraphy. Calcareous nannofossil assemblages are abundant to rare, with the exception of Sample 339-U1388B-9X-CC, which is barren. Preservation is moderate, with the presence of dissolution and overgrowth in some samples. Small placolith species (<3 µm) dominate most of the assemblages (Table T5).

Two Pleistocene nannofossil datums defined and/or calibrated by Raffi et al. (2006 and references therein) were identified in all holes (Table T4).

The FO of *Emiliania huxleyi* (0.26 Ma), which marks the base of Zone NN21, was placed between Samples 339-U1388B-6X-CC and 7X-CC (47.47–56.14 mbsf). However, this event should be taken with caution because of dissolution effects and the low proportion of this species. The LO of *P. lacunosa* (0.46 Ma), considered a globally synchronous event that defines the top of Zone NN19, occurs between Samples 339-U1388B-18X-CC and 19X-CC (162.82–178.02 mbsf).

Planktonic foraminifers

The core catcher samples from Site U1388 contain high amounts of lithic grains (commonly in the fine sand range; Table T6). Therefore, planktonic foraminifer abundance is relatively low (abundant to present). Foraminifer abundance exceeds 30% only in Sample 339-U1388B-2X-CC. Three samples from Hole U1388B are barren, and four additional samples are almost barren. Preservation is often very good, revealing pristine foraminifer shells. Three samples (339-U1388B-4X-CC, 17X-CC, and 19X-CC) show only moderate preservation. The planktonic foraminifer assemblage is typical for this region, with species linked to temperate to subtropical waters. Similar to the previous sites, the assemblages are dominated by *Globigerina bulloides*, *Neogloboquadrina pachyderma* (dextral), and *Globorotalia inflata*. *Orbulina universa*, *Globorotalia truncatulinoides*, and *Globigerinella siphonifera* contribute regularly to the fauna. Sample 339-U1388A-1H-CC contains *Globigerinoides trilobus* and *Globigerinoides sacculifer* and therefore most likely dates from the Holocene.

Benthic foraminifers

Samples 339-U1388A-1H-CC, 339-U1388B-1H-CC through 24X-CC, and 339-U1388C-2R-CC through 4R-CC were analyzed for benthic foraminiferal assemblages (Table T7). As with Sites U1386 and U1387, the abundance and preservation of benthic foraminifers is related to lithology, and higher abun-

dance and well-preserved benthic foraminifers are observed in finer sediments. The abundance of benthic foraminifers fluctuates from rare to highly abundant. Samples 339-U1388B-5X-CC and 9X-CC and 339-U1388B-18X-CC are barren. In most of the samples that revealed foraminifers, benthic assemblages are moderately to well preserved, except for Samples 339-U1388B-4X-CC and 7X-CC.

The benthic foraminiferal fauna is mainly composed of species of *Brizalina*, *Bulimina*, *Cassidulina*, *Cibicides*, *Globobulimina*, *Sphaeroidina*, and *Uvigerina* in varying proportions. In general, an upper bathyal environment is indicated. Transport from the shelf, indicated by *Ammonia beccarii*, *Asterigerinata planorbis*, and *Elphidium* spp., occurs sporadically and is mainly restricted to the upper part of the succession. Two major assemblages can be distinguished that suggest variations in ventilation and/or MOW current strength and that alternate throughout the succession:

Assemblages composed of *Brizalina dilatata*, *Bulimina aculeata*, *Cassidulina laevigata/teretis*, and *Sphaeroidina bulloides* characterize environments with increased organic matter flux and reduced ventilation (van Morkhoven et al., 1986; Leckie and Olson, 2003; Murray, 2006). Peak abundances of *Brizalina* spp. (Sample 339-U1388B-12X-CC, 14X-CC, and 20X-CC) indicate maxima in oxygen depletion of bottom water related to enhanced input of organic matter and/or a well-stratified water column.

Assemblages with high abundances of *Cibicides/Cibicides* spp. and *Uvigerina* spp. (Samples 339-U1388B-3X-CC, 7X-CC, 15X-CC, 21X-CC through 24X-CC, and 339-U1388C-2R-CC through 4R-CC) indicate increased ventilation, potentially related to an increase in MOW current strength. Within some of these assemblages, the “epibenthos group,” suggested as an indicator for MOW intensity in the area (Schönfeld, 1997, 2002; Schönfeld and Zahn, 2000), shows abundances of >5%. The exceptionally high abundance of *Cibicides lobatulus* in Sample 339-U1388B-3X-CC might be related to a peak in MOW strength close to the exit of the Strait of Gibraltar.

The *Stilostomella* extinction event was not recognized at Site U1388, thus suggesting that the deposits are younger than 0.58–0.7 Ma (Hayward, 2002; Kawagata et al., 2005). However, in Sample 339-U1388B-2X-CC, several moderately well preserved tests of *Pleurostomella alternans*, *Siphonodosaria ketienziensis*, and *Siphonodosaria subtertenuata* were found, which are absent in all other samples. As the same sample yields very high abundances of reworked

early Pleistocene nannofossils, we consider the foraminiferal tests reworked too.

Palynology

Samples 339-U1388B-2X-CC and 14X-CC were analyzed for palynology. The main pollen types found at this site, deciduous and evergreen *Quercus*, *Olea*, Ericaceae, Chenopodiaceae, *Artemisia*, *Taraxacum*-type, and Poaceae (Table T8), are those already observed at the previous Sites U1386 and U1387 (see “Palynology” in the “Site U1386” chapter [Expedition 339 Scientists, 2013b] and “Palynology” in the “Site U1387” chapter [Expedition 339 Scientists, 2013c]). The first sample is characterized by poorly preserved pollen morphotypes and, as is normal for such samples, an abundance of *Taraxacum*-type pollen grains. The sample below, Sample 339-U1388B-14X-CC, is composed of an important fraction of well-preserved pollen grains dominated by semidesert elements, mainly *Artemisia* and Chenopodiaceae, indicating a period of arid and cold conditions in the close continents between 0.26 and 0.46 Ma (Table T4).

Paleomagnetism

Paleomagnetic investigation of the APC, XCB, and RCB cores collected at Site U1388 included measurement of magnetic susceptibility of whole-core and archive-half split-core sections and the natural remanent magnetization (NRM) of archive-half split-core sections. NRM was measured before and after alternating field (AF) demagnetization with 20 mT peak field for all studied cores of the site. Stepwise AF demagnetization of 10 selected discrete samples was performed at successive peak fields of 0, 5, 10, 15, 20, 25, 30, 35, 40, 45, 50, 55, 60, 70, and 80 mT to verify the reliability of the split core measurements and to determine the demagnetization behavior of the recovered sediment. The depth levels where the measured discrete samples were taken are indicated by blue triangles in the first panel of Figure F22. We processed data extracted from the Laboratory Information Management System (LIMS) database by removing all measurements collected from disturbed and void intervals, which are listed in Table T9, and all measurements that were made within 10 cm of the section ends, which are slightly biased by measurement edge effects. The processed NRM inclination, declination, and intensity data after 20 mT peak field AF demagnetization are listed in Tables T10, T11, and T12.

Natural remanent magnetization and magnetic susceptibility

The intensity of NRM after 20 mT peak field AF demagnetization is in the range of $\sim 10^{-4}$ to $\sim 10^{-2}$ A/m (Fig. F22, third panel). The sands from lithologic Unit I (Core 339-U1388A-1H; see “Lithostratigraphy”) exhibit very low intensities ($\sim 10^{-4}$ A/m) and are underlain by sediment with moderately high intensity values ($\sim 10^{-3}$ – 10^{-2} A/m).

Despite the XCB-induced coring disturbance and the drill string overprint, a very stable magnetic component was preserved in the sediment. A magnetic overprint with steep, positive inclination, which was probably acquired during drilling, was usually removed by up to 20 mT peak field AF demagnetization (Fig. F23). Although the XCB cores are heavily biscuited and frequently contain as much of the disturbed matrix as the intact material, the quality of the resulting paleomagnetic data is excellent and sufficient to determine the magnetic polarity.

Except for two discrete samples from Hole U1388A that consist of mainly sands from lithologic Unit I (see “Lithostratigraphy”) and failed to yield stable NRM, progressive AF demagnetization of eight discrete samples from Hole U1388B revealed stable NRM with positive inclinations (Fig. F23). Several samples exhibit a steep, normal overprint that was generally removed after AF demagnetization at peak field of ~ 15 – 20 mT, demonstrating that the 20 mT magnetic cleaning level is, in general, sufficient to eliminate the overprint. A few samples also appear to have acquired a significant amount of anhysteretic remanent magnetization at high peak field (>55 mT) AF demagnetization steps, especially for one sample from 160.86 mbsf in Hole U1388B (Fig. F23). The acquired anhysteretic remanent magnetization is possibly because of bias caused by ambient magnetic field during AF demagnetization at high peak fields. We calculated component NRM directions of the eight discrete samples from data from 25–50 mT demagnetization steps using principal component analysis (Kirschvink, 1980) and the UPmag software (Xuan and Channell, 2009). Maximum angular deviations associated with the principal component analysis are mostly $<10^\circ$, suggesting the component NRM directions are reasonably well defined. Component NRM inclinations of these discrete samples vary between $\sim 50^\circ$ and 65° (Fig. F22, yellow circles on inclination panel) and are generally consistent with the archive-half section measurements.

Magnetic susceptibility measurements were made on whole cores from all three holes as part of the Whole-Round Multi Sensor Logger (WRMSL) analysis and on archive-half split core sections using the Section Half Multi Sensor Logger (SHMSL) (see “[Physical properties](#)”). Magnetic susceptibility is consistent between the two instruments and, in general, parallels the intensity of magnetic remanence. The WRMSL acquired susceptibility was stored in the database in raw meter units. These were multiplied by a factor of 0.68×10^{-5} to convert to the dimensionless volume SI unit (Blum, 1997). A factor of $(67/80) \times 10^{-5}$ was multiplied by the SHMSL acquired susceptibility stored in the database. Magnetic susceptibility varies between 5×10^{-5} and 40×10^{-5} SI (Fig. [F22](#), fourth panel). Note that in Figure [F22](#), a constant of 25×10^{-5} SI was added to the SHMSL measurements (gray lines) to facilitate the comparison with the WRMSL measurements (black lines).

Magnetostratigraphy

The geomagnetic field at the latitude of Site U1388 (36.27°N) has an expected inclination of 55.73°, assuming a geocentric axial dipole model, which is sufficiently steep to determine magnetic polarity in cores that lack a horizontal orientation. NRM inclination data (after 20 mT peak field AF demagnetization) from all three holes indicate that only the Brunhes (C1n) normal polarity chron is recorded in these sediments (Fig. [F22](#)). This interpretation is supported by the discrete sample measurements. A discrete sample from the base of Hole U1388B (Sample 339-U1388B-24X-7, 44–46 cm) clearly carries a positive inclination and is <0.781 Ma. Whether the Brunhes Chron is complete or incomplete cannot be determined from the magnetostratigraphy. However, preliminary biostratigraphic datums (see “[Biostratigraphy](#)”) indicate an age between 600 and 900 ka at the base of Hole U1388B.

Physical properties

The shipboard physical properties program at Site U1388 included high-resolution nondestructive measurements of gamma ray attenuation (GRA) density, magnetic susceptibility (loop sensor), *P*-wave velocity (mostly in 2.5 cm steps), and NGR on whole-round core sections measured each 20 cm. Thermal conductivity was not obtained at this site because of poor recovery and sediment disturbance. Discrete measurements of *P*-wave velocity were determined on every other working-half section in Hole U1388B between Cores 12X and 20X. Moisture and density (MAD) were measured once in every section as 10 cm³ discrete samples. Color reflectance spectrometry

and split-core point-logger magnetic susceptibility were obtained for every section in each hole in 5 cm steps. Based on physical properties, three intervals were distinguished. The first interval (physical properties Unit I), between 0 and 100 mbsf, is characterized by low core recovery and high-frequency variations of all parameters. A second interval (physical properties Unit II), between 100 and ~150 mbsf, is characterized by high core recovery and a marked positive relationship between GRA density and magnetic susceptibility values. A third interval (physical properties Unit III), from ~150 mbsf to the bottom of the hole, displays low magnetic susceptibility values and indistinct relations between the different parameters.

Whole-Round Multisensor Logger measurements

After allowing the cores to equilibrate for 3 h, GRA bulk density and magnetic susceptibility were measured in all core sections at 2.5 cm intervals at Site U1388 using the WRMSL (Fig. [F24](#)).

Gamma ray attenuation density

Variations in GRA density may reflect changes in lithology, consolidation, cementation, and porosity. Measured GRA density ranges between 1.26 and 2.01 g/cm³ in Hole U1388A, showing a steady increase in the upper intervals that probably reflects the presence of a coarse sand layer. A marked decrease observed in the lower part of the hole can be linked with an increase in fine sand content (Fig. [F24](#)).

In Hole U1388B from 0 to 100 mbsf, core recovery was very poor and GRA density ranges between 1.7 and 2.2 g/cm³. Despite the poor recovery, distinct high-frequency variations can be recognized (e.g., Cores 339-U1388B-9X and 10X). These high-frequency variations are also present in the upper part of Core 339-U1388B-12X, in which recovery is higher. The boundary between this high-frequency to lower frequency variation further downhole is in Core 339-U1388B-12X at ~110 mbsf. This boundary also can be distinguished by a change in lithology, concomitant with a decrease in the number of sandy turbidite layers (see “[Lithostratigraphy](#)”).

GRA density below 110 mbsf has almost the same values as those obtained from discrete samples. Density values range between 1.9 and 2.1 g/cm³ in the interval between 110 and ~150 mbsf for MAD and between 1.6 and 2.1 g/cm³ for GRA. There was high core recovery in this interval, which allows us to identify a strong link between GRA density, magnetic susceptibility, and the presence of silt and sands. Despite the positive correlation between GRA

density and magnetic susceptibility, the relationship between NGR and the color reflectance parameters L^* and a^* is complex. Comparing GRA density to L^* shows that high GRA density is not clearly associated with distinct changes in sediment lightness. In general, GRA density and NGR show a negative correlation in this interval, a relationship contrasting with that at other sites. This complex pattern can be linked with the abundance of detrital material including mica, zircon, glauconite, opaques, heavy minerals, and feldspars (see “[Lithostratigraphy](#)”) in both muddy and sandy layers.

In the lower part of Site U1388, GRA density values range between 1.6 and 2.1 g/cm³. The GRA density variations are difficult to correlate with changes in grain size (e.g., Cores 339-U1388B-19X and 20X). This could be linked with changes in the nature or fabric of the grains, as indicated by grain density variations (Fig. [F25](#)). The highest GRA density values in this interval correspond to layers with coarse grain size and low NGR values. Typically, sandy beds are associated with low GRA density, so this unexpected result could be explained by an unusual mineralogical composition.

Magnetic susceptibility

The most notable aspects of the magnetic susceptibility records at Site U1388 are the cyclical and smooth variations observed between 100 and ~150 mbsf and the low values below ~150 mbsf (Fig. [F24](#)). In the upper 100 m (physical properties Unit I), where core recovery was poor, susceptibility values range from 10×10^{-5} to 30×10^{-5} SI. In physical properties Unit II, where core recovery was high, magnetic susceptibility long-term trends show three major cycles that become progressively more intense, with average values between 10×10^{-5} and 40×10^{-5} SI. Other minor cycles and spikes are superimposed on the major cycles and reach 80×10^{-5} SI, the highest magnetic susceptibility value. These cyclic variations are mirrored by GRA density values and are associated with the presence of silty/sandy layers with high magnetic susceptibility.

Magnetic susceptibility values are low ($<20 \times 10^{-5}$ SI) from ~150 mbsf to the bottom of the hole (physical properties Unit III). This observation is also supported by low NRM values (see “[Paleomagnetism](#)”). Despite these low values, the composition of the sediment appears to be almost the same as in the overlying intervals, suggesting that diagenetic processes are controlling magnetic susceptibility in this interval. A likely factor for the main decrease of magnetic susceptibility is the reduction of fine-grained magnetite to iron sulfides below the sulfate reduction zone. However, the present sulfate–methane transition

(SMT) zone, occurring around 40 mbsf and recognized in Hole U1388B (see “[Geochemistry](#)”), shows no correlation between low magnetic susceptibility and this boundary.

P-wave velocity

No reasonable *P*-wave velocity measurements were retrieved using the WRMSL. An attempt was made to determine *P*-wave velocities on split cores in each section of Hole U1388B (Fig. [F24](#)). Because of low core recovery and poor sediment to liner coupling, reasonable results from split cores were recovered only between ~100 and ~180 mbsf and values range between 1550 and 1730 m/s. *P*-wave velocities determined by the split-core logger do not show a clear correlation with any other physical property or lithology. Caution must be taken in interpreting the manually picked data, in which greater subjectivity and poorer signal quality lead to higher scatter in the data. The method of manually picking data tends to overestimate velocities.

Natural gamma radiation

NGR was measured on all core sections at 20 cm spacing and run on an integration time of 7 min per section. Measured values range from 20 to 45 cps, with a single peak reaching 88 cps in Core 339-U1388B-12X, which was not plotted because it appears to be an artifact. No distinctive explanatory feature can be found in the sediment (Fig. [F26](#)).

In Hole U1388A there is an interval of coarse sediment, in which NGR has low values around 19 cps. In the high-recovery interval from ~100 to ~150 mbsf in Hole U1388B, we can observe three cycles with progressively increasing amplitudes in NGR and a marked increase at the base of Core 339-U1388A-16X. Along this interval, NGR shows mainly negative correlations with magnetic susceptibility and GRA density. However, NGR values do not always reflect observed changes in grain size. This can be related to the described homogeneous mineral composition (see “[Lithostratigraphy](#)”).

Below ~150 mbsf core recovery is poorer, but major variations in NGR values can be distinguished in Cores 339-U1388B-18X, 20X, and 22X. In these cases, NGR values increase and decrease by 10 cps over ~2 m. Lows in NGR counts appear to be related to the presence of coarse sand deposits, probably with a lower content of K-feldspars or any other mineral enriched in potassium and thorium contents. This marked decrease in NGR is coincident with an increase in GRA density and relatively high values in grain density. No obvious correlation can be found in this interval between NGR and color reflectance parameters.

Moisture and density

Measurements of bulk density, porosity, and grain density were undertaken on 2 samples from Hole U1388A, 41 samples from Hole U1388B, and 4 samples from Hole U1388C. One MAD sample was taken every other section. The samples were taken at the same depths, approximately 60 cm from the top of the section, when available. Care was also taken to avoid locations with obvious drilling disturbance. These samples were measured for wet mass and dry density to calculate bulk density and grain density.

The MAD bulk densities from discrete samples are plotted in Figure F24 and show a range of 1.9–3.2 g/cm³. In the upper 110 mbsf, GRA and MAD bulk densities show certain offsets, where discrete sample densities are occasionally higher than those measured with the WRMSL. In the interval of high recovery between 110 and 150 mbsf, densities obtained by both techniques are in agreement. For the lowermost interval, below 150 mbsf, WRMSL values are lower because of poor core recovery and incompletely filled core liners, which affect the accuracy of the WRMSL measurements.

The patterns of porosity and moisture content in the interval between 110 and 150 mbsf stand out with respect to those of the other physical parameters, as they have only two amplitude cycles instead of three (Fig. F25). These two cycles appear to be related to long-term compositional changes interrupted by a coarser layer in Core 339-U1388B-15X. In general, samples taken from predominantly silt/sandy sections show lower values in porosity and moisture content. In addition, wet bulk densities appear to be higher in coarse-grained levels. This observation is not sufficiently resolved. Notably, only the dry volume of the sample was determined, not the wet bulk volume. Hence, the difference between the two density estimates might be related to the precipitation of salt crystals in the pore space during sample drying at 105°C, which would affect the determination of dry volumes by pycnometer and all further calculations.

Porosity ranges from 38% to 50%, decreasing with depth in the upper ~100 mbsf (Fig. F25). Bulk densities do not exhibit clear increasing values with depth for Hole U1388B (Fig. F24). The lack of compaction-related depth trends could be a result of poor core recovery and the relatively shallow depths reached in this site. NGR values indicate compositional variations for certain intervals, although grain density values are relatively constant in the range from ~2.6 to ~2.8 g/cm³ without clear trends (Figs. F25, F26). A density peak of 3.2 g/cm³ is found in Core 339-U1388B-24X. Grain densities are on average slightly

higher than quartz density (2.65 g/cm³) and probably reflect the varying degree of heavy minerals, opaques, and zircon in the sediment.

Summary of main results

The most remarkable observation at Site U1388 with respect to the previous sites is the negative correlation between GRA density and NGR and the inconsistent correlation between GRA density, magnetic susceptibility, and NGR with color reflectance parameters. When we compare physical properties with lithology, we observe that high GRA densities and magnetic susceptibility are associated with layers of coarse sediment. Nevertheless, NGR is not consistently sensitive to grain size variations (e.g., coarse grain layers), which are in some cases coincident with low NGR values but in other cases not. This relationship between physical properties was not observed at the previous sites and could be related to a homogeneous mineral composition in both fine and coarse layers. In any case, the described changes require more detailed analyses in order to be sufficiently explained.

Geochemistry

Volatile hydrocarbons

Headspace gas analysis was performed as a part of the standard protocol required for shipboard safety and pollution prevention monitoring. In total, 20 headspace samples were analyzed, including 1 from Hole U1388A, 18 from Hole U1388B, and 1 from Hole U1388C (Fig. F27; Table T13), spanning the entire depth range of the site. Methane (C₁), ethane (C₂), and ethene (C₂₌) were the only hydrocarbons detected. Methane ranged from 10.38 ppmv near the surface to a maximum of 65,682 ppmv at 160.1 mbsf (Section 339-U1388B-18X-2). Ethane was detected at and below 83.6 mbsf and remained less than 2.75 ppmv. Ethene was detected at and below 147 mbsf and did not exceed 0.82 ppmv.

Sedimentary geochemistry

Sediment samples were collected for analysis of solid-phase geochemistry (inorganic and organic carbon) at a resolution of approximately one sample per core in Holes U1388A–U1388C (Table T14), spanning the maximum penetration at this site. CaCO₃ varies from 18.0 to 29.9 wt% (Fig. F8). Organic carbon is generally low and varies between 0.08 and 0.92 wt% (Fig. F28A).

Nitrogen was measured downhole to 224.74 mbsf, with values ranging from 0.02 to 0.11 wt% (Fig.

F28B). The C/N ratio, used to distinguish the origin of organic matter (marine versus terrestrial) in sediment (Emerson and Hedges, 1988; Meyers, 1997), indicates that the organic carbon is mainly of marine origin with little terrestrial input (Fig. **F28C**). The highest C/N value of 16 is at 36.34 mbsf, corresponding to a portion of the core with fine-sand composition. The surrounding sediment is mainly clay and silt. A slight positive relationship appears to exist between organic matter content and C/N ratios, but it is weaker than at Sites U1385–U1387.

Interstitial water chemistry

Major cations and anions

Elemental analyses were made on 14 samples from whole-round samples taken at Site U1388 to a total depth of 211 mbsf, including 1 sample from Hole U1388A and 13 from Hole U1388B.

Sulfate concentrations are near seawater values at the top of the section and decrease to zero by ~50 mbsf (Fig. **F29A**; Table **T15**). Alkalinity generally increases downhole with the exception of a low interval between 125 and 150 mbsf (Fig. **F29B**). Ammonium gradually increases from near zero at the top of the hole to a maximum of 8000 μM at 200 mbsf (Fig. **F29C**). Methane begins to increase at 50 mbsf, marking the SMT (Fig. **F29D**).

Calcium, magnesium, and potassium profiles show similar patterns, with a sharp decrease between the top of the hole and 50 mbsf (Fig. **F30**). Potassium continues to gradually decrease downhole, whereas calcium and magnesium increase. Chloride and sodium increase downhole from seawater values at the top of the section to a maximum of 800 and 690 mM at 211 mbsf, respectively (Fig. **F31**). The Na/Cl ratio remains near the seawater value (0.86) throughout the section.

Minor elements

Strontium remains near seawater value in the upper 75 mbsf and increases thereafter, reaching its greatest values at the base of the hole (Fig. **F32**). Barium was below detection in the uppermost sample and increases downhole to a maximum of 57 μM between 107 and 128 mbsf. Thereafter, barium decreases downhole to 150 mbsf and averages ~25 μM below. Lithium decreases between the surface and 50 mbsf and then increases downhole, exhibiting a pattern similar to that of strontium. Boron is high in the upper 50 mbsf and undergoes a series of stepped decreases downhole at 70, 100, and 150 mbsf. Silicon concentration is 110 μM at the surface and generally increases downhole, with a distinct maximum of 647 μM between 160 and 177 mbsf.

Figure **F33** shows the relationship of various elemental concentrations versus chloride. Sodium, calcium, magnesium, and strontium show strong positive relationships with chloride, whereas potassium, boron, and barium display a negative correlation with chloride.

Stable isotopes

Oxygen and hydrogen isotopes were measured on 14 samples from whole-round samples at Site U1388. At the top of the hole, $\delta^{18}\text{O}$ and δD are at bottom water values of 0.8‰ and 6.5‰, respectively, and increase to 1.3‰ and 9.2‰ by 50 mbsf, respectively (Fig. **F34**; Table **T16**). δD gradually decreases below 50 mbsf toward the base of the hole, whereas average $\delta^{18}\text{O}$ values remain between 1.3‰ and 1.4‰. $\delta^{18}\text{O}$ and δD are generally positively correlated (Fig. **F35**).

Discussion

The interstitial water profiles at Site U1388 reflect a combination of processes, including microbial degradation of organic matter, dissolution, precipitation of authigenic minerals, and the likely influence of a brine. Sulfate reduction is complete in the uppermost 50 mbsf. The increase in alkalinity and decreases in calcium and magnesium reflect authigenic precipitation of calcite and dolomite. This interpretation is supported by a peak in dolomite observed in XRD data at 36.34 mbsf (see “**Lithostratigraphy**”). The linear downhole increase and high values of sodium and chloride at depth suggest a source for these elements in the deeper sediment. Some mud volcanoes in the Gulf of Cádiz have high salinities derived from dissolution of halite and late-stage evaporites (Hensen et al., 2007; Scholz et al., 2009). Nevertheless, no strong deviation from the seawater value for Na/Cl (0.86) at Site U1388 is apparent, as would be expected from the dissolution of halite (Na/Cl = 1). Vengosh et al. (1994) suggests that the high salinity values of interstitial waters in Mediterranean Deep Sea Drilling Project sites with Na/Cl ratios typical of seawater are the remnants of Miocene hypersaline lakes, and perhaps these brines also are present in the eastern Gulf of Cádiz.

Stratigraphic correlation

Three holes were drilled at Site U1388. The construction of a composite section was not warranted because of incomplete or lack of recovery. The upper 4 mbsf was cored in both Holes U1388A and U1388B, but there was no recovery in Core 339-U1388B-1H. The interval from 205 to 226 mbsf was cored in both Holes U1388B and U1388C. Recovery was again incomplete over this interval, and the core is partly

disturbed. Correlation may be possible between Cores 339-U1388B-24X and 339-U1388C-3R, but correlation would be based on one susceptibility peak that is ~0.50 m higher in Core 339-U1388B-24X than in 339-U1388C-3R.

References

- Akhmetzhanov, A., 2003. Modern analogues of deep-water hydrocarbon reservoirs [Ph.D. thesis]. Moscow State Univ., Russia.
- Akhmetzhanov, A., Kenyon, N.H., Habgood, E., Van Der Mollen, A.S., Neilsen, T., Ivanov M., and Shashkin, P., 2007. North Atlantic contourite sand channels. *In* Viana, A.R., and Rebesco, M. (Eds.), *Economic and Palaeoceanographic Significance of Contourite Deposits*. Geol. Soc. Spec. Publ., 276(1):25–47. doi:10.1144/GSL.SP.2007.276.01.02
- Akhmetzhanov, A.M., Kenyon, N.H., Habgood, E.L., Gardner, J., Ivanov, M.K., and Shashkin, P., 2002. Sand lobes in the Gulf of Cádiz: towards better understanding of clastic reservoir high-resolution architecture. *In* Cunha, M., Pinheiro, L., and Suzyumov, A. (Eds.), *Geosphere/Biosphere/Hydrosphere Coupling Processes, Fluid Escape Structures and Tectonics at Continental Margins and Ocean Ridges*. IOC Workshop Rep., 183:23. (Abstract) http://www.jodc.go.jp/info/ioc_doc/Workshop/127690e.pdf
- Blum, P., 1997. Physical properties handbook: a guide to the shipboard measurement of physical properties of deep-sea cores. *ODP Tech. Note*, 26. doi:10.2973/odp.tn.26.1997
- Brackenridge, R., Stow, D.A.V., and Hernández-Molina, F.J., 2011. Contourite sands: nature, distribution and controls [28th International Association of Sedimentologists (IAS) Meeting of Sedimentology, Zaragoza, Spain, 5–8 July 2011].
- Buitrago, J., García, C., Cajebread-Brow, J., Jiménez, A., and Martínez del Olmo, W., 2001. Contouritas: Un Excelente Almacén Casi Desconocido (Golfo de Cádiz, SO de España) [Congreso Técnico Exploración y Producción REPSOL-YPF, Madrid, Spain, 24–27 September 2001].
- Emerson, S., and Hedges, J.I., 1988. Processes controlling the organic carbon content of open ocean sediments. *Paleoceanography*, 3(5):621–634. doi:10.1029/PA003i005p00621
- Expedition 339 Scientists, 2013a. Expedition 339 summary. *In* Stow, D.A.V., Hernández-Molina, F.J., Alvarez Zarikian, C.A., and the Expedition 339 Scientists, *Proc. IODP*, 339: Tokyo (Integrated Ocean Drilling Program Management International, Inc.). doi:10.2204/iodp.proc.339.101.2013
- Expedition 339 Scientists, 2013b. Methods. *In* Stow, D.A.V., Hernández-Molina, F.J., Alvarez Zarikian, C.A., and the Expedition 339 Scientists, *Proc. IODP*, 339: Tokyo (Integrated Ocean Drilling Program Management International, Inc.). doi:10.2204/iodp.proc.339.102.2013
- Expedition 339 Scientists, 2013c. Site U1386. *In* Stow, D.A.V., Hernández-Molina, F.J., Alvarez Zarikian, C.A., and the Expedition 339 Scientists, *Proc. IODP*, 339: Tokyo (Integrated Ocean Drilling Program Management International, Inc.). doi:10.2204/iodp.proc.339.104.2013
- Expedition 339 Scientists, 2013d. Site U1387. *In* Stow, D.A.V., Hernández-Molina, F.J., Alvarez Zarikian, C.A., and the Expedition 339 Scientists, *Proc. IODP*, 339: Tokyo (Integrated Ocean Drilling Program Management International, Inc.). doi:10.2204/iodp.proc.339.105.2013
- Expedition 339 Scientists, 2013e. Site U1389. *In* Stow, D.A.V., Hernández-Molina, F.J., Alvarez Zarikian, C.A., and the Expedition 339 Scientists, *Proc. IODP*, 339: Tokyo (Integrated Ocean Drilling Program Management International, Inc.). doi:10.2204/iodp.proc.339.107.2013
- García, M., Hernández-Molina, F.J., Llave, E., Stow, D.A.V., León, R., Fernández-Puga, M.C., Díaz del Río, V., and Somoza, L., 2009. Contourite erosive features caused by the Mediterranean Outflow Water in the Gulf of Cádiz: Quaternary tectonic and oceanographic implications. *Mar. Geol.*, 257(1–4):24–40 doi:10.1016/j.mar-geo.2008.10.009
- Habgood, E.L., 2002. Alongslope and downslope sediment transport processes in the Gulf of Cádiz [Ph.D. thesis]. Univ. Southampton, United Kingdom.
- Habgood, E.L., Kenyon, N.H., Masson, D.G., Akhmetzhanov, A., Weaver, P.P.E., Gardner, J., and Mulder, T., 2003. Deep-water sediment wave fields, bottom current sand channels, and gravity flow channel-lobe systems: Gulf of Cádiz, NE Atlantic. *Sedimentology*, 50(3):483–510. doi:10.1046/j.1365-3091.2003.00561.x
- Hanquiez, V., Mulder, T., Lecroart, P., Gonthier, E., Marchès, E., and Voisset, M., 2007. High resolution sea-floor images in the Gulf of Cádiz, Iberian margin. *Mar. Geol.*, 246(1):42–59. doi:10.1016/j.mar-geo.2007.08.002
- Hayward, B.W., 2002. Late Pliocene to middle Pleistocene extinctions of deep-sea benthic foraminifera (“*Stilostomella* extinction”) in the southwest Pacific. *J. Foraminiferal Res.*, 32(3):274–307. doi:10.2113/32.3.274
- Hensen, C., Nuzzo, M., Hornibrook, E., Pinheiro, L.M., Bock, B., Magalhães, V.H., and Brückmann, W., 2007. Sources of mud volcano fluids in the Gulf of Cádiz—indications for hydrothermal imprint. *Geochim. Cosmochim. Acta*, 71(5):1232–1248. doi:10.1016/j.gca.2006.11.022
- Hernández-Molina, F.J., Llave, E., Somoza, L., Fernández-Puga, M.C., Maestro, A., León, R., Medialdea, T., Barnolas, A., García, M., Díaz del Río, V., Fernández-Salas, L.M., Vázquez, J.T., Lobo, F., Alveirinho Dias, J.M., Rodero, J., and Gardner, J., 2003. Looking for clues to paleoceanographic imprints: a diagnosis of the Gulf of Cádiz contourite depositional systems. *Geology*, 31(1):19–22. doi:10.1130/0091-7613(2003)031<0019:LFCTPI>2.0.CO;2
- Hernández-Molina, F.J., Llave, E., Stow, D.A.V., García, M., Somoza, L., Vázquez, J.T., Lobo, F.J., Maestro, A., Díaz

- del Río, V., León, R., Medialdea, T., and Gardner, J., 2006. The contourite depositional system of the Gulf of Cádiz: a sedimentary model related to the bottom current activity of the Mediterranean Outflow Water and its interaction with the continental margin. *Deep-Sea Res., Part II*, 53(11–13):1420–1463. doi:10.1016/j.dsr2.2006.04.016
- Hernández-Molina, F.J., Serra, N., Stow, D.A.V., Llave, E., Ercilla, G., and Van Rooij, D., 2011. Along-slope oceanographic processes and sedimentary products around the Iberian margin. *Geo-Mar. Lett.*, 31(5–6):315–341. doi:10.1007/s00367-011-0242-2
- Kawagata, S., Hayward, B.W., Grenfell, H.R., and Sabaa, A., 2005. Mid-Pleistocene extinction of deep-sea foraminifera in the North Atlantic Gateway (ODP Sites 980 and 982). *Palaeogeogr., Palaeoclimatol., Palaeoecol.*, 221(3–4):267–291. doi:10.1016/j.palaeo.2005.03.001
- Kenyon, N.H., and Belderson, R.H., 1973. Bed forms of the Mediterranean undercurrent observed with side-scan sonar. *Sediment. Geol.*, 9(2):77–99. doi:10.1016/0037-0738(73)90027-4
- Kirschvink, J.L., 1980. The least-squares line and plane and the analysis of palaeomagnetic data. *Geophys. J. R. Astron. Soc.*, 62(3):699–718. doi:10.1111/j.1365-246X.1980.tb02601.x
- Leckie, R.M., and Olson, H.C., 2003. Foraminifera as proxies of sea-level change on siliciclastic margins. In Olson, H.C., and Leckie, R.M. (Eds.), *Micropaleontologic Proxies of Sea-Level Change and Stratigraphic Discontinuities*. Spec. Publ.—SEPM (Soc. Sediment. Geol.), 75:5–19.
- Legg, S., Briegleb, B., Chang, Y., Chassignet, E.P., Danabasoglu, G., Ezer, T., Gordon, A.L., Griffies, S., Hallberg, R., Jackson, L., Large, W., Özgökmen, T.M., Peters, H., Price, J., Riemenschneider, U., Wu, W., Xu, X., and Yang, J., 2009. Improving oceanic overflow representation in climate models: the gravity current entrainment climate process team. *Bull. Am. Meteorol. Soc.*, 90(5):657–670. doi:10.1175/2008BAMS2667.1
- Llave, E., Hernández-Molina, F.J., Somoza, L., Stow, D.A.V., and Díaz del Río, V., 2007. Quaternary evolution of the contourite depositional system in the Gulf of Cádiz. *Geol. Soc. Spec. Publ.*, 276:49–79. doi:10.1144/GSL.SP.2007.276.01.03
- Llave, E., Hernández-Molina, F.J., Stow, D., Somoza, L., and Díaz del Río, V., 2005. The contourite depositional system in the Gulf of Cádiz: an example of drifts with reservoir potential characteristics. In Martínez del Olmo, W. (Ed.), *Asociación de Geólogos y Geofísicos Españoles del Petróleo (XXV aniversario)*: Madrid (AGGEP and REP-SOL-YPF), 53–73. <http://www.aggep.org/AGGEP/Documentos/Intro%20XXV%20Aniversario.pdf>
- Llave, E., Matias, H., Hernández-Molina, F.J., Ercilla, G., Stow, D.A.V., and Medialdea, T., 2011. Pliocene–Quaternary contourites along the northern Gulf of Cadiz margin: sedimentary stacking pattern and regional distribution. *Geo-Mar. Lett.*, 31(5–6):377–390. doi:10.1007/s00367-011-0241-3
- Madelain, F., 1970. Influence de la topographie du fond sur l'écoulement méditerranéen entre le Détroit de Gibraltar et le Cap Saint-Vincent. *Cah. Océanogr.*, 22:43–61.
- Meyers, P.A., 1997. Organic geochemical proxies of paleoceanographic, paleolimnologic, and paleoclimatic processes. *Org. Geochem.*, 27(5–6):213–250. doi:10.1016/S0146-6380(97)00049-1
- Murray, J.W., 2006. *Ecology and Applications of Benthic Foraminifera*: Cambridge (Cambridge Univ. Press).
- Nelson, C.H., Baraza, J., and Maldonado, A., 1993. Mediterranean undercurrent sandy contourites, Gulf of Cádiz, Spain. *Sediment. Geol.*, 82(1–4):103–131. doi:10.1016/0037-0738(93)90116-M
- Raffi, I., Backman, J., Fornaciari, E., Pälike, H., Rio, D., Lourens, L., and Hilgen, F., 2006. A review of calcareous nannofossil astrobiochronology encompassing the past 25 million years. *Quat. Sci. Rev.*, 25(23–24):3113–3137. doi:10.1016/j.quascirev.2006.07.007
- Scholz, F., Hensen, C., Reitz, A., Romer, R.L., Liebetrau, V., Meixner, A., Weise, S.M., and Haeckel, M., 2009. Isotopic evidence ($^{87}\text{Sr}/^{86}\text{Sr}$, $\delta^7\text{Li}$) for alteration of the oceanic crust at deep-rooted mud volcanoes in the Gulf of Cádiz, NE Atlantic Ocean. *Geochim. Cosmochim. Acta*, 73(18):5444–5459. doi:10.1016/j.gca.2009.06.004
- Schönfeld, J., 1997. The impact of the Mediterranean Outflow Water (MOW) on benthic foraminiferal assemblages and surface sediments at the southern Portuguese continental margin. *Mar. Micropaleontol.*, 29(3–4):211–236. doi:10.1016/S0377-8398(96)00050-3
- Schönfeld, J., 2002. Recent benthic foraminiferal assemblages in deep high-energy environments from the Gulf of Cádiz (Spain). *Mar. Micropaleontol.*, 44(3–4):141–162. doi:10.1016/S0377-8398(01)00039-1
- Schönfeld, J., and Zahn, R., 2000. Late glacial to Holocene history of the Mediterranean Outflow. Evidence from benthic foraminiferal assemblages and stable isotopes at the Portuguese margin. *Palaeogeogr., Palaeoclimatol., Palaeoecol.*, 159(1–2):85–111. doi:10.1016/S0031-0182(00)00035-3
- Serra, N., 2004. Observations and numerical modelling of the Mediterranean Outflow [Ph.D. thesis]. Univ. Lisbon, Spain.
- Serra, N., Ambar, I., and Boutov, D., 2010. Surface expression of Mediterranean water dipoles and their contribution to the shelf/slope–open ocean exchange. *Ocean Sci.*, 6(1):191–209. doi:10.5194/os-6-191-2010
- Stow, D., Brackenridge, R., and Hernandez-Molina, F.J., 2011a. Contourite sheet sands: new deepwater exploration target [presented at the AAPG 2011 Annual Convention and Exhibition, Houston, Texas, 10–13 April, 2011].
- Stow, D., Hernández-Molina, F.J., Hodell, D., and Alvarez Zarikian, C.A., 2011b. Mediterranean outflow: environmental significance of the Mediterranean Outflow Water and its global implications. *IODP Sci. Prosp.*, 339. doi:10.2204/iodp.sp.339.2011
- Stow, D.A.V., and Faugères, J.-C., 2008. Contourite facies and the facies model. *Dev. Sedimentol.*, 60:223–256. doi:10.1016/S0070-4571(08)10013-9
- van Morkhoven, F.P.C.M., Berggren, W.A., and Edwards, A.S., 1986. *Cenozoic Cosmopolitan Deep-Water Benthic Foraminifera*. Bull. Cent. Rech. Explor.—Prod. Elf-Aquitaine, 11.

- Vengosh, A., Starinsky, A., and Anati, D.A., 1994. The origin of Mediterranean interstitial waters—relics of ancient Miocene brines: a re-evaluation. *Earth Planet Sci. Lett.*, 121(3–4):613–627. doi:10.1016/0012-821X(94)90095-7
- Viana, A.R., 2008. Economic relevance of contourites. *Dev. Sedimentol.*, 60:491–510. doi:10.1016/S0070-4571(08)10023-1
- Viana, A.R., Almeida, W., Jr., Nunes, M.C.V., and Bulhões, E.M., 2007. The economic importance of contourites. *Geol. Soc. Spec. Publ.*, 276(1):1–23. doi:10.1144/GSL.SP.2007.276.01.01
- Xuan, C., and Channell, J.E.T., 2009. UPmag: MATLAB software for viewing and processing U channel or other pass-through paleomagnetic data. *Geochem., Geophys., Geosyst.*, 10(10):Q10Y07. doi:10.1029/2009GC002584

Publication: 17 June 2013
MS 339-106



Figure F1. 3-D sketch showing the location of Site U1388 ($36^{\circ}16.142'N$, $6^{\circ}47.648'W$) over the contourite terrace in the proximal sector of the contourite depositional system close to the Strait of Gibraltar (made by H. Pereira, Escola Secundária de Loulé, Portugal, using Mironé and iView4D software).

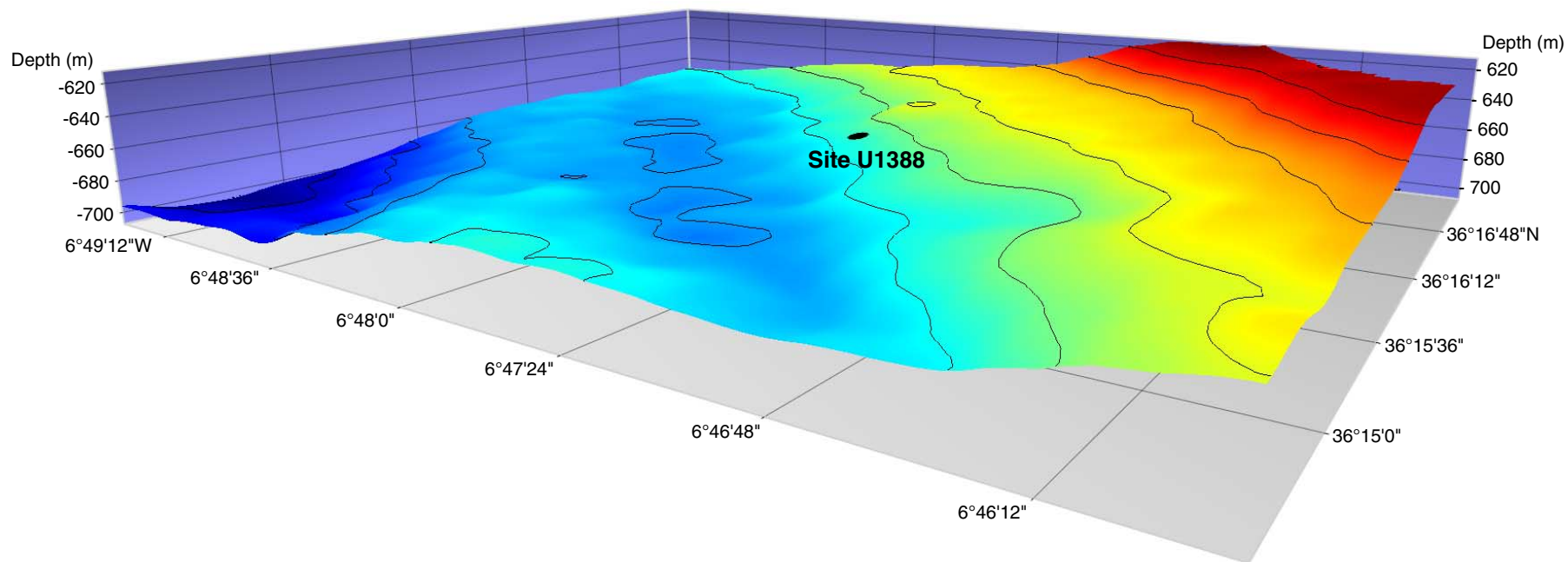


Figure F2. Original Seamap side-scan data including proximal scour and sand ribbons (Sector 1) over the contourite terrace and overflow sedimentary lobe (Sector 2). Red circle indicates location of Site U1388. Furrows legend from Kenyon and Belderson (1973) and Habgood et al. (2003). From Hernández-Molina et al. (2006). Data courtesy of Joan Gardner from Naval Research Laboratory, USA.

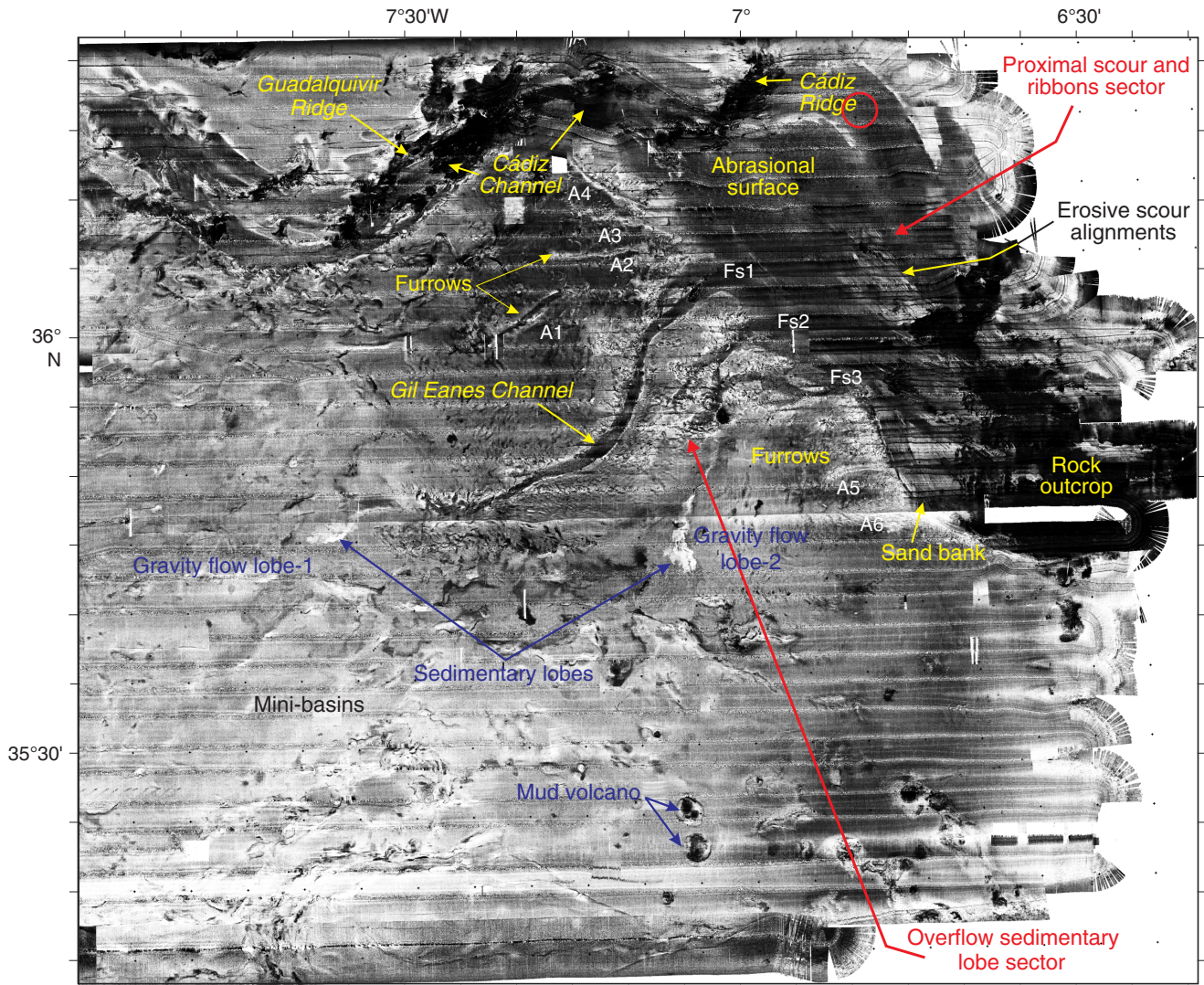


Figure F3. Bathymetric sketch with the location of Site U1388 on an extensive sandy sheeted drift of the proximal Sector 1 of the contourite depositional system close to the Gibraltar Gateway (base map made by Dr. R. León, Geological Survey, IGME, Spain).

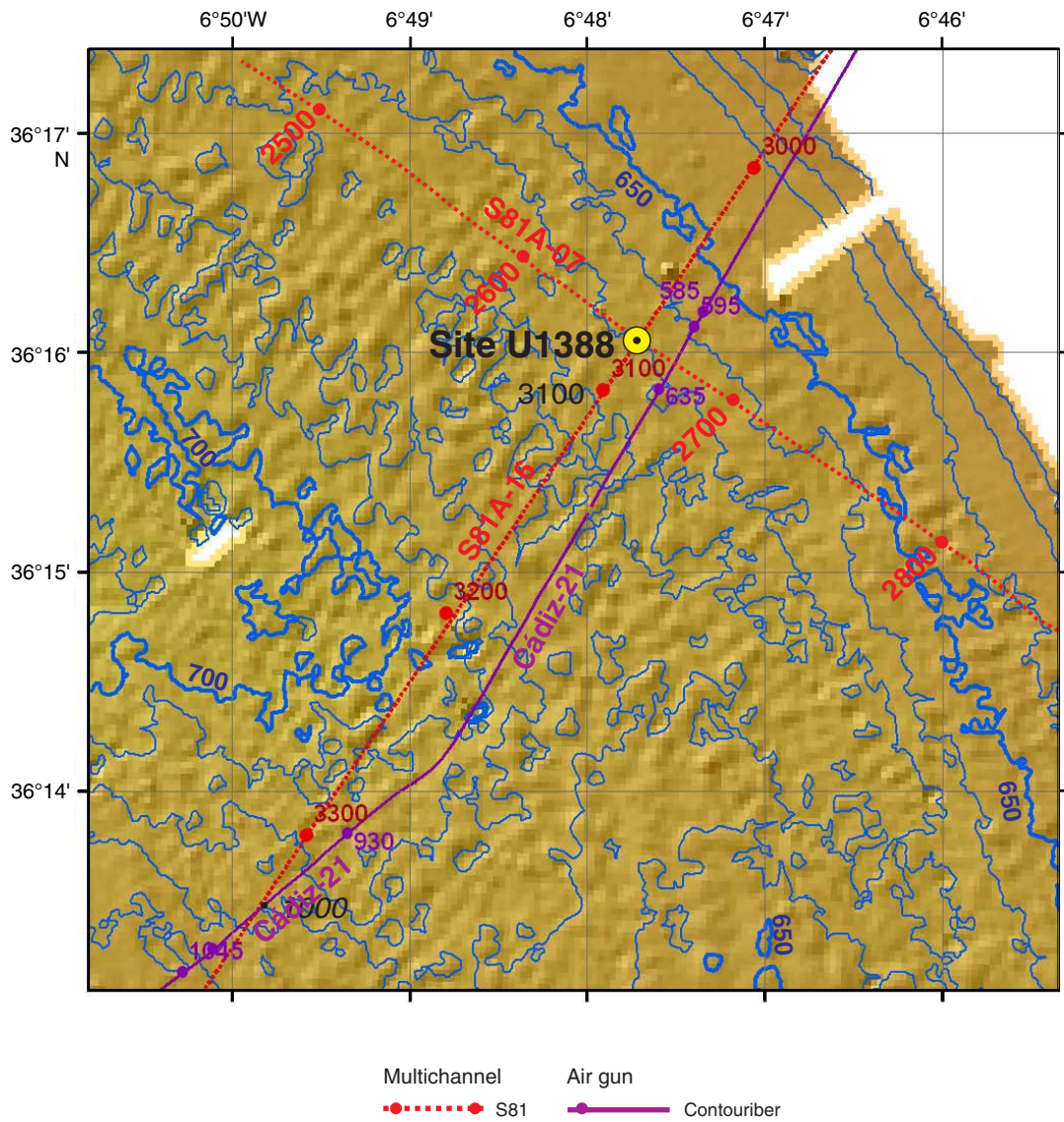




Figure F4. Seismic profiles from the proximal scour and sand ribbons Sector 1. From Hernández-Molina et al. (2006) and Llave et al. (2007). **A.** Sketch sector and seismic lines. **B.** Abrasional surface with high backscatter intensity. **C.** Several erosive scour alignments with a northeast–southwest orientation, smooth V- shaped expression, and truncated reflectors. **D.** Longitudinal bedforms (southeast to northwest) caused by MOW. Red circle indicates location of Site U1388.

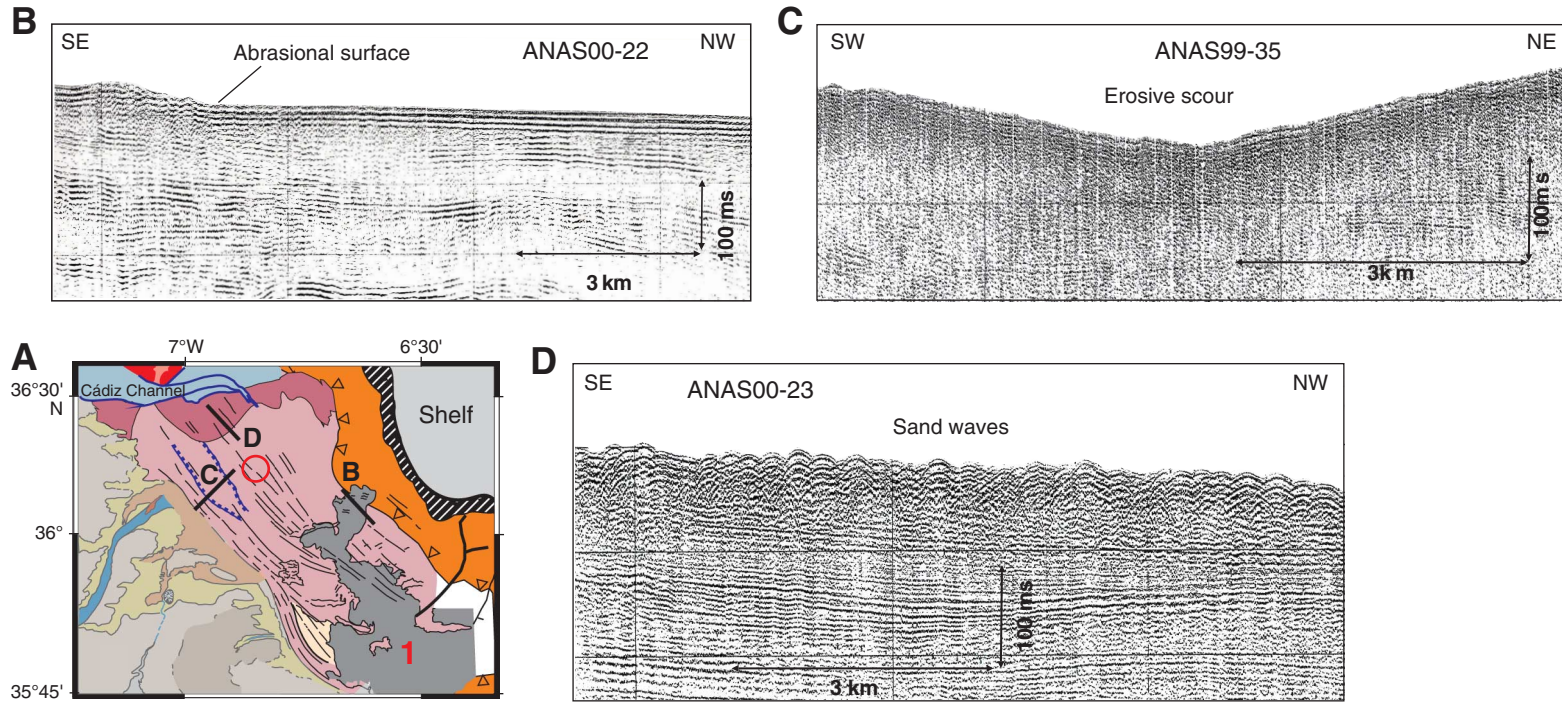




Figure F5. Graphic overview of the oceanographic patterns in the Gulf of Cádiz (from García et al., 2009) showing the circulation pattern of Mediterranean Outflow Water (MOW) cores and branches. Red circle indicates location of Site U1388.

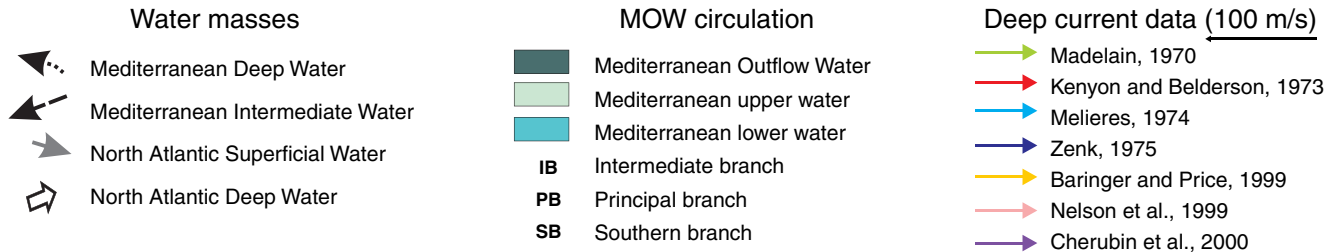
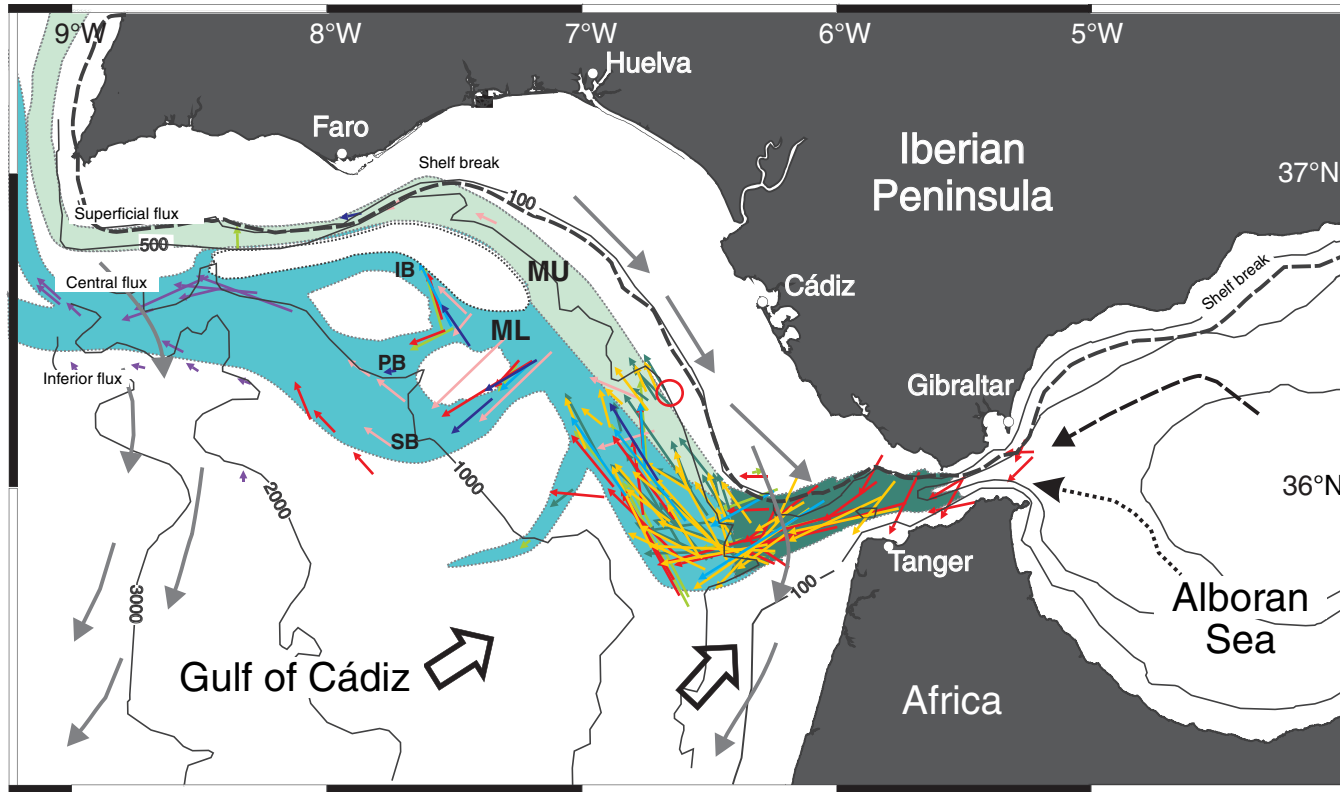


Figure F6. Graphic lithology summary log, Site U1388.

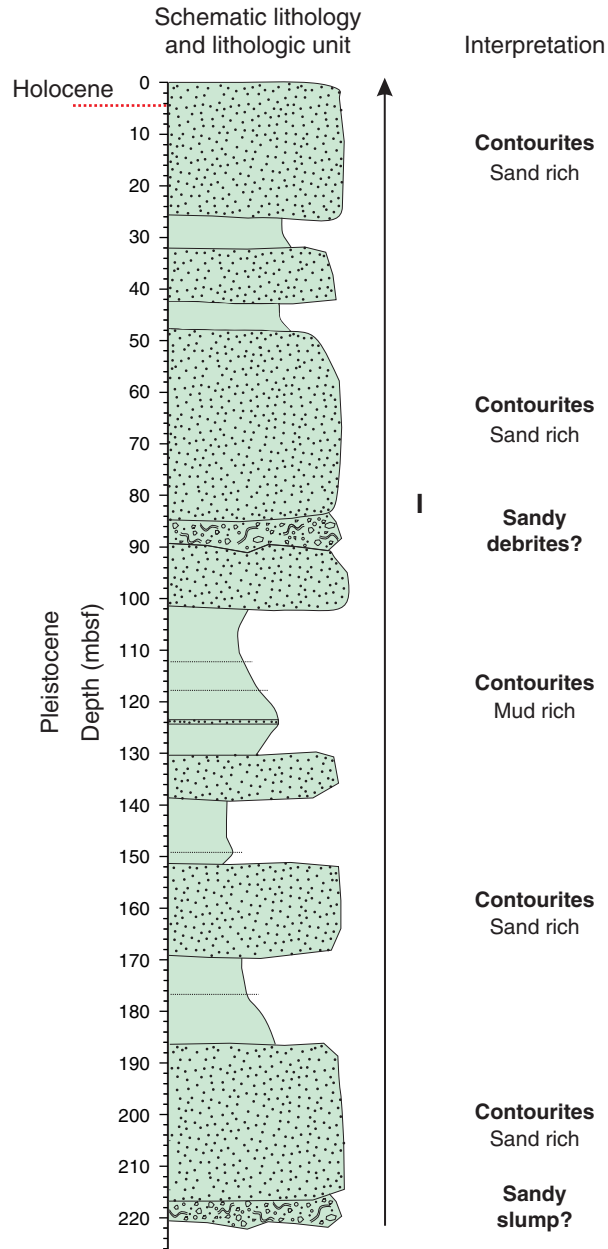


Figure F7. Plot of downhole variations in lithologies, Site U1388.

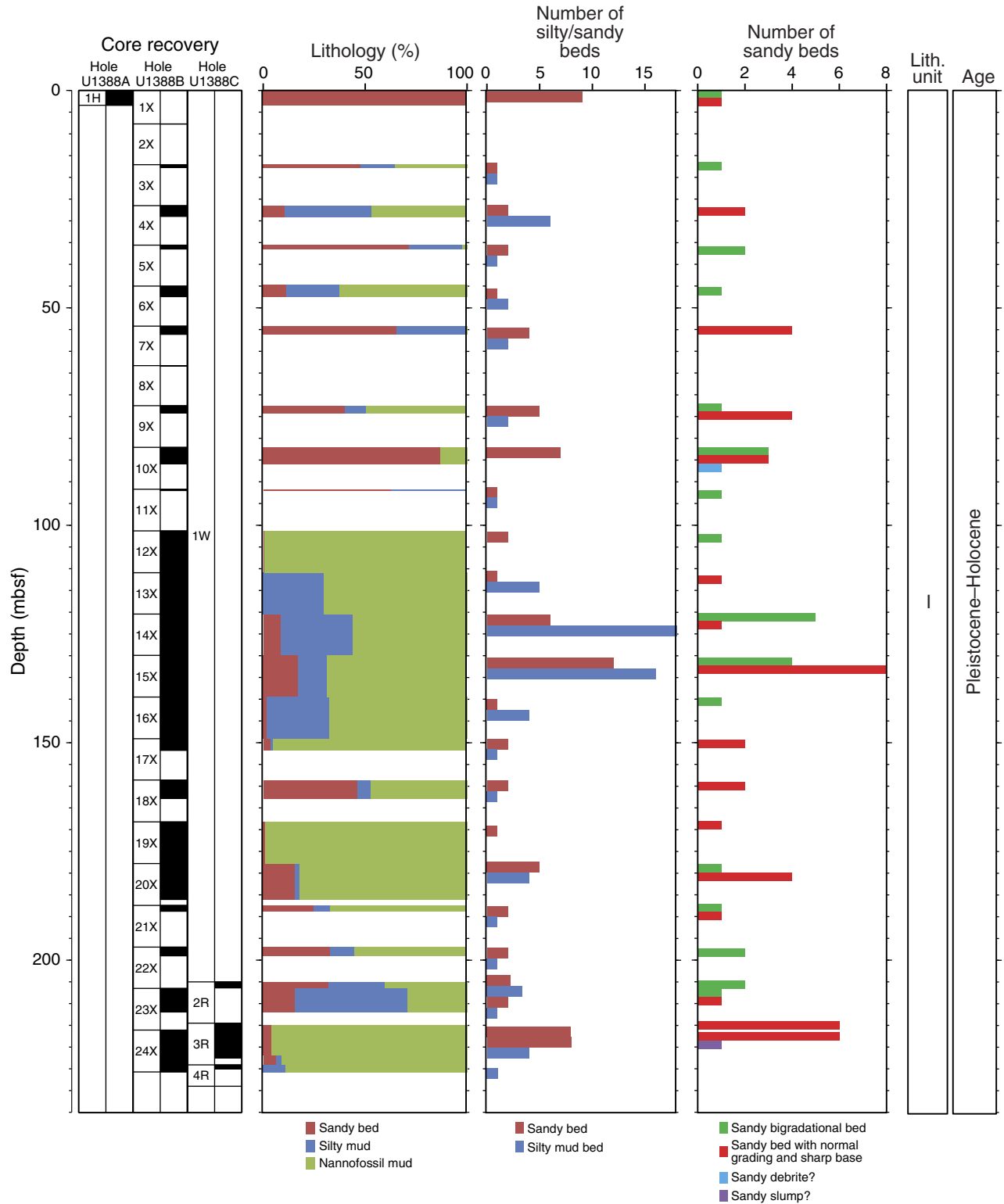


Figure F8. Plot of calcium carbonate, Holes U1388A (solid circle) and U1388B (open circles).

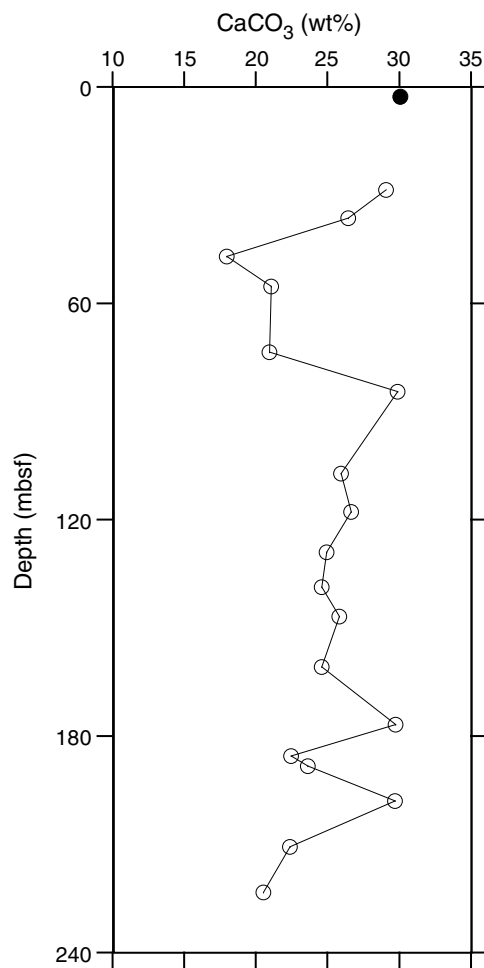


Figure F9. Graphic lithology summaries, Site U1388. A. Hole U1388A. (Continued on next two pages.)



Figure F9 (continued). B. Hole U1388B. (Continued on next page.)

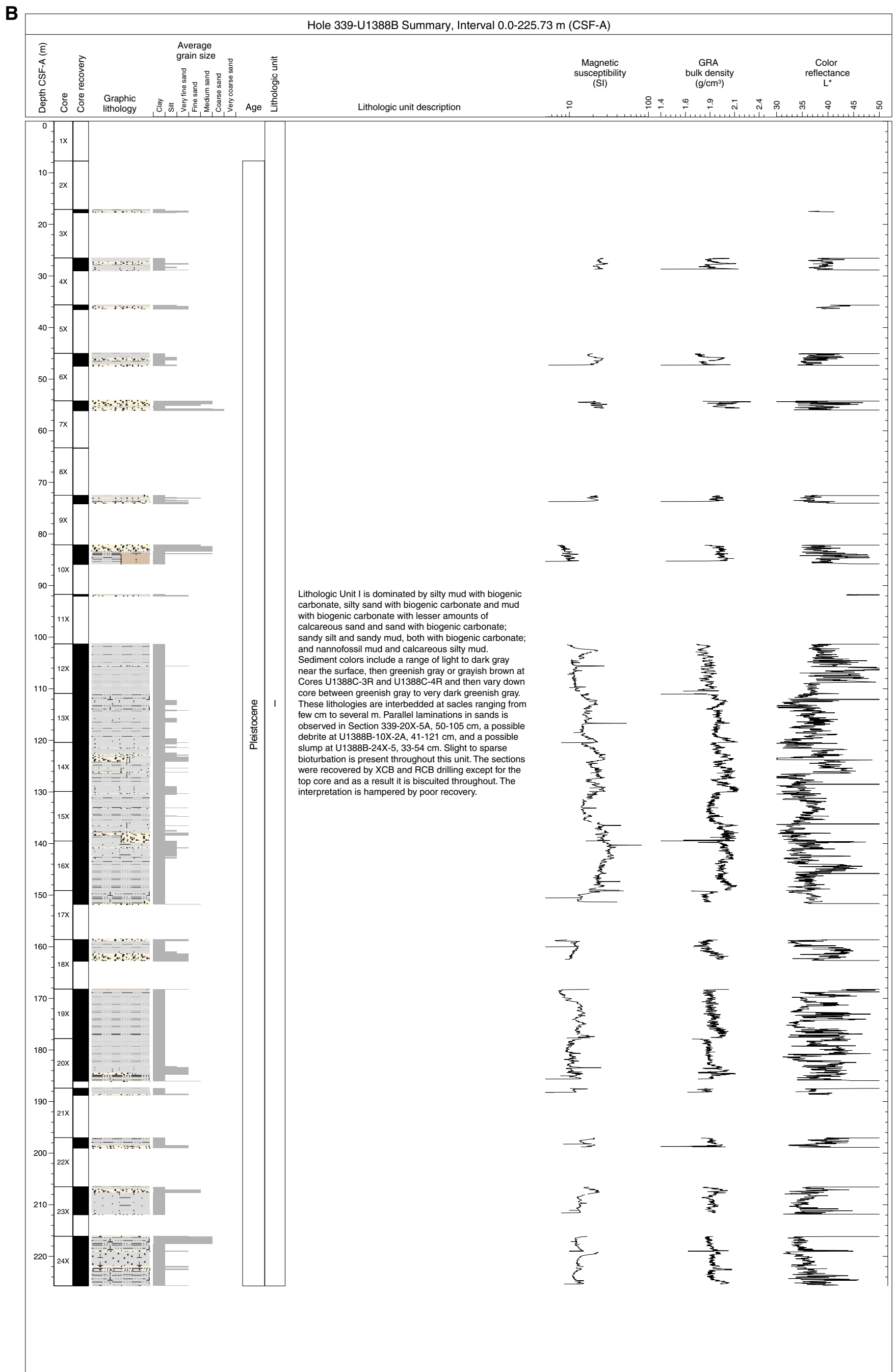


Figure F9 (continued). C. Hole U1388C

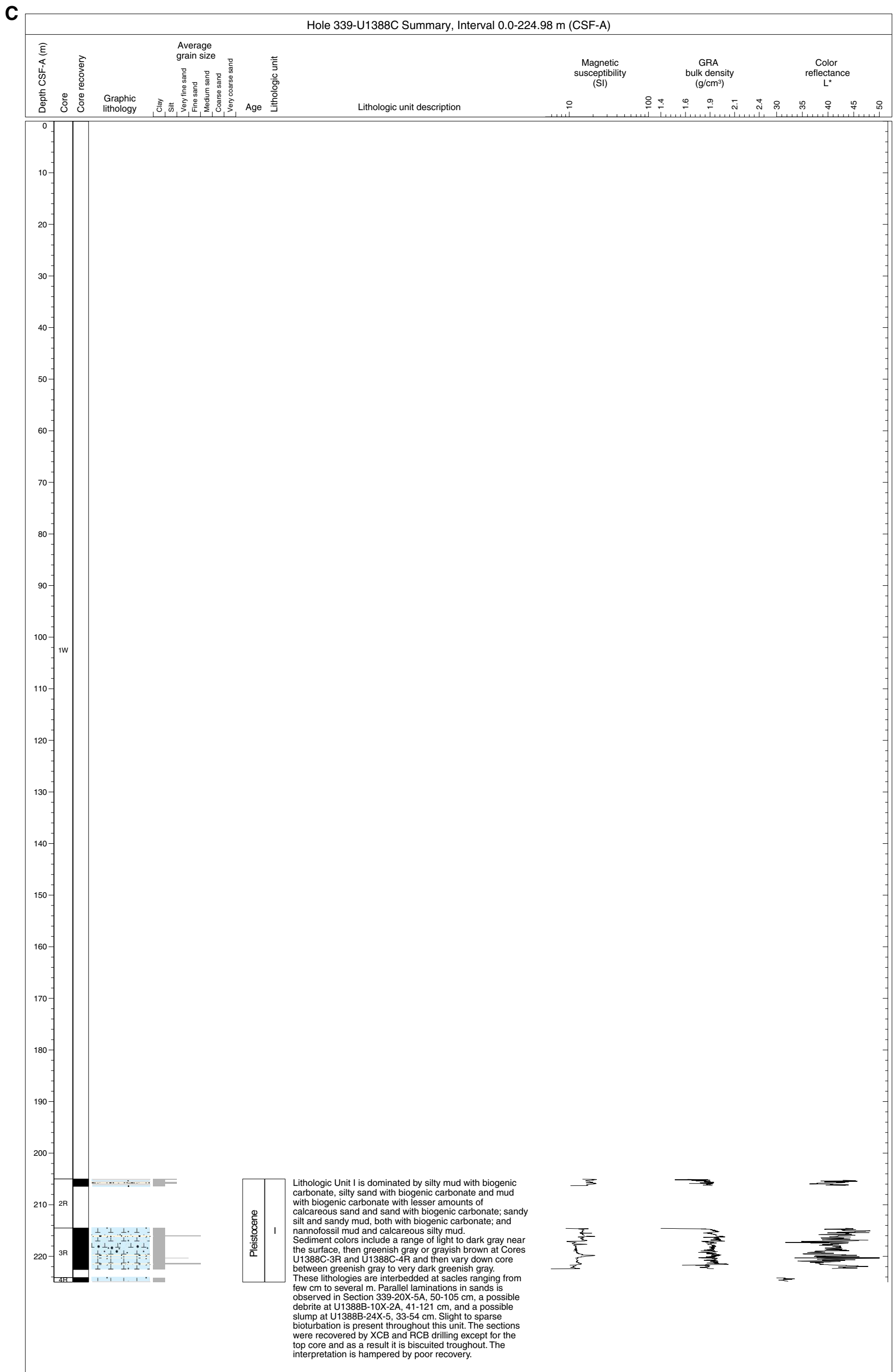




Figure F10. Plot of percentage of coarser beds (sandy and silty beds) relative to the total thickness cored and relative to the total thickness recovered. If the sediment not recovered by XCB drilling in the upper 100 m of Hole U1388B is primarily muds and silty muds, then the abundances of coarser and finer lithologies are relatively uniform through the entire section at Site U1388. If the unrecovered sediments above ~100 mbsf are primarily sands and silts, then coarser lithologies are significantly more abundant in the upper 100 m of the section.

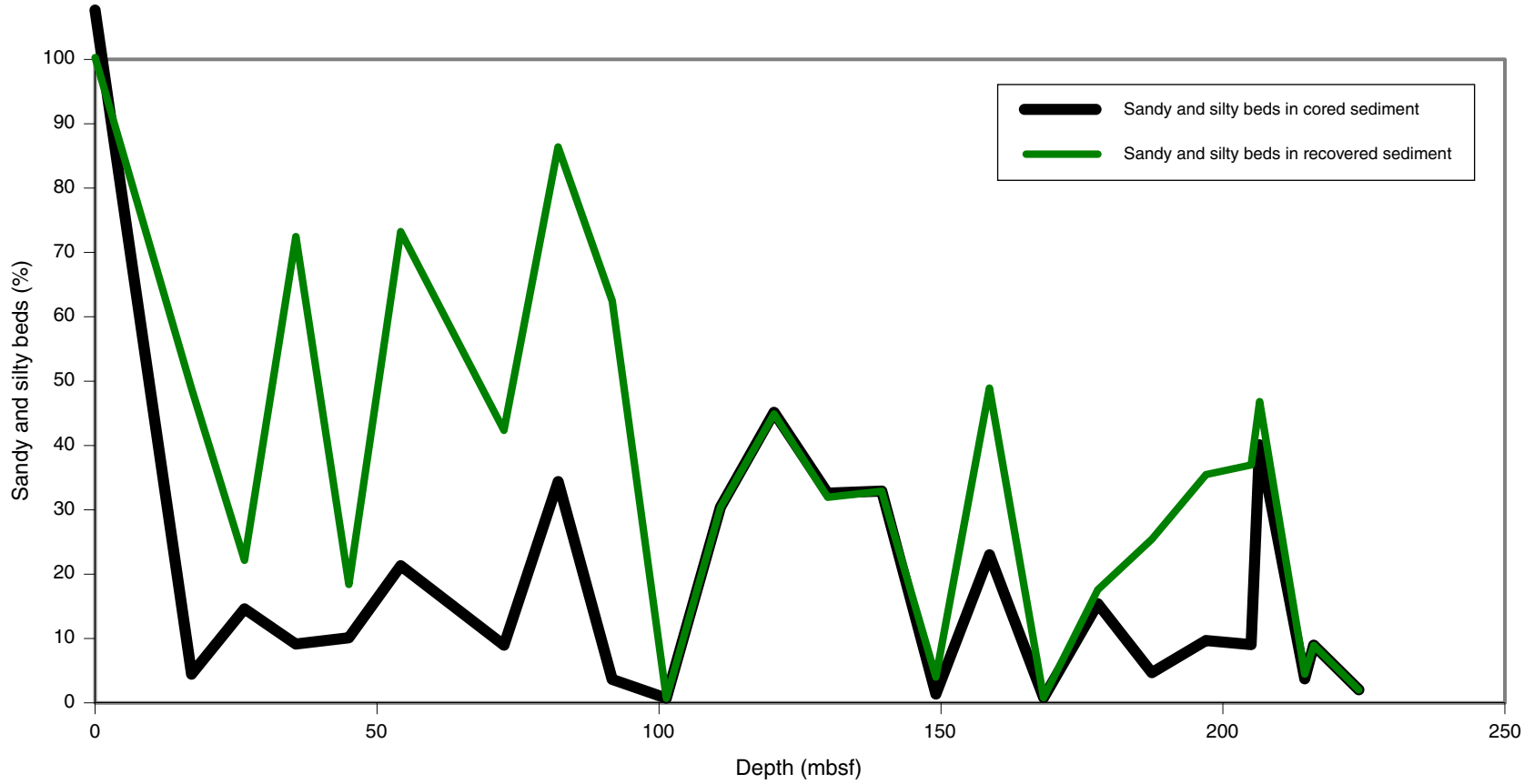


Figure F11. Core image of a contourite bed (Section 339-U1388B-16X-13A). Pink material visible in places on the core surface is drilling mud.



Figure F12. Core image of a sharp basal contact (Section 339-U1388B-19X-1A).

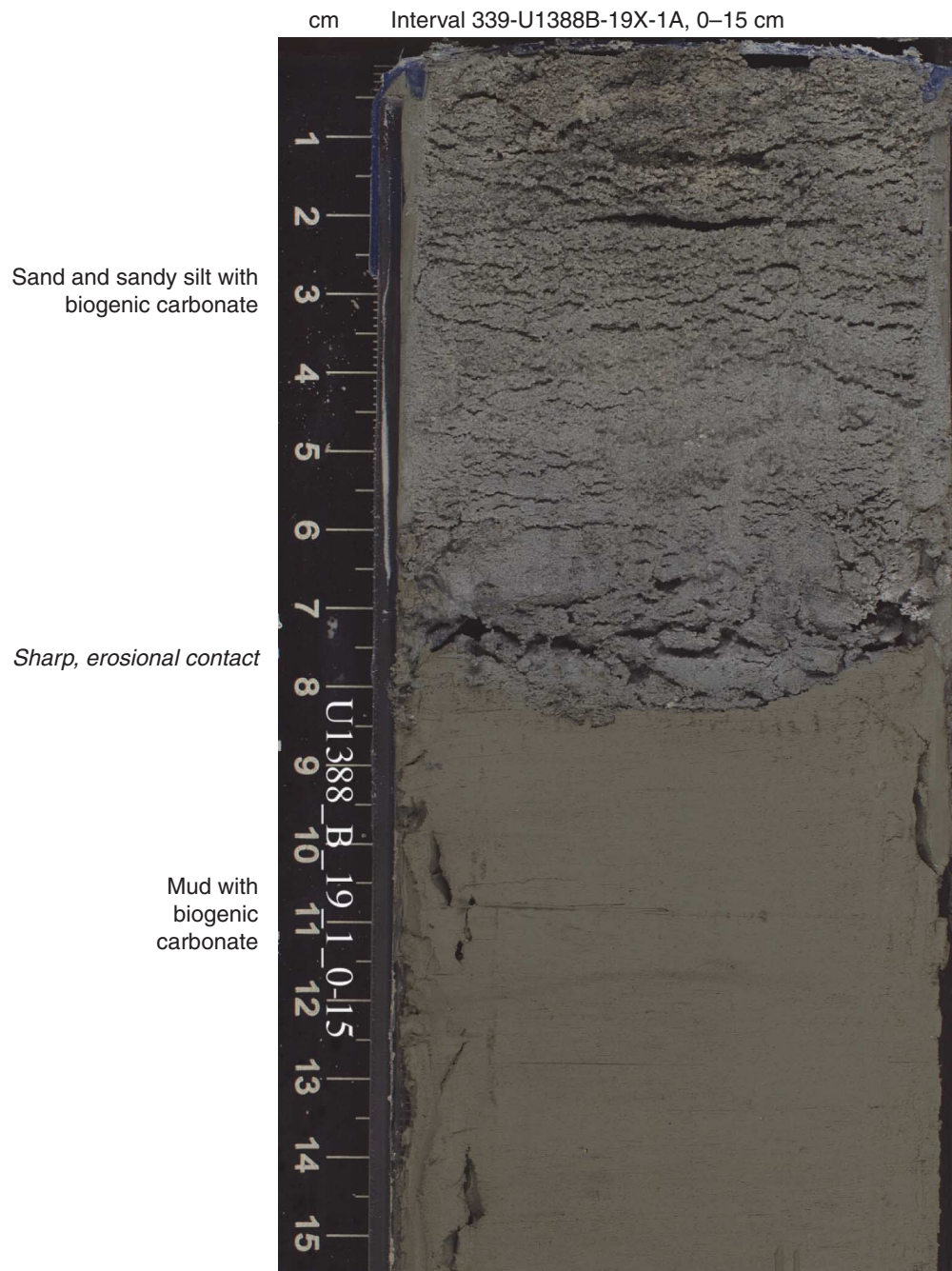


Figure F13. Core image of an inversely graded bed (Section 339-U1388C-3R-2A).

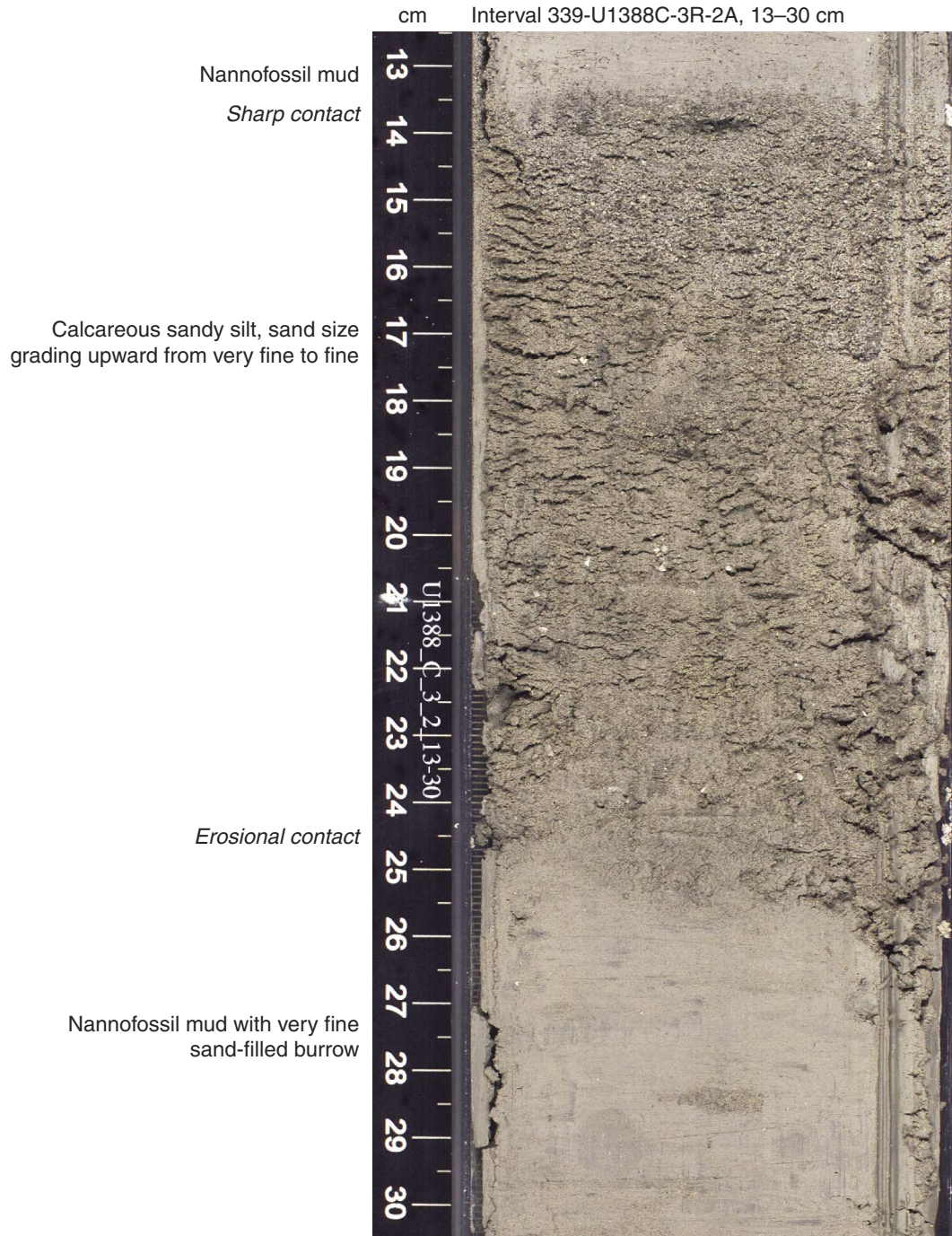


Figure F14. Core image of an inversely graded bed (Section 339-U1388C-3R-4A).

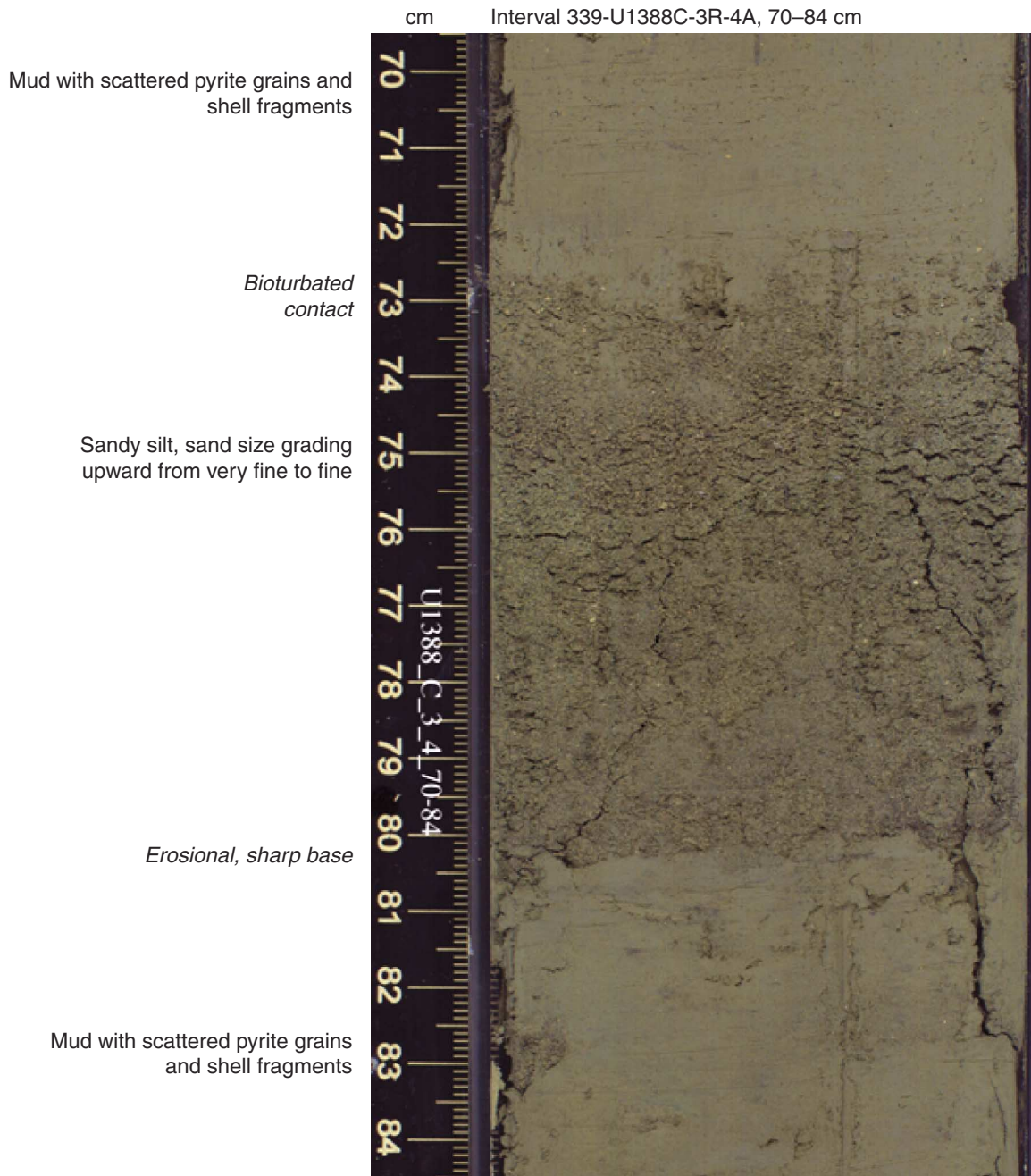


Figure F15. Core image of an inversely graded bed (Section 339-U1388C-3R-5A).

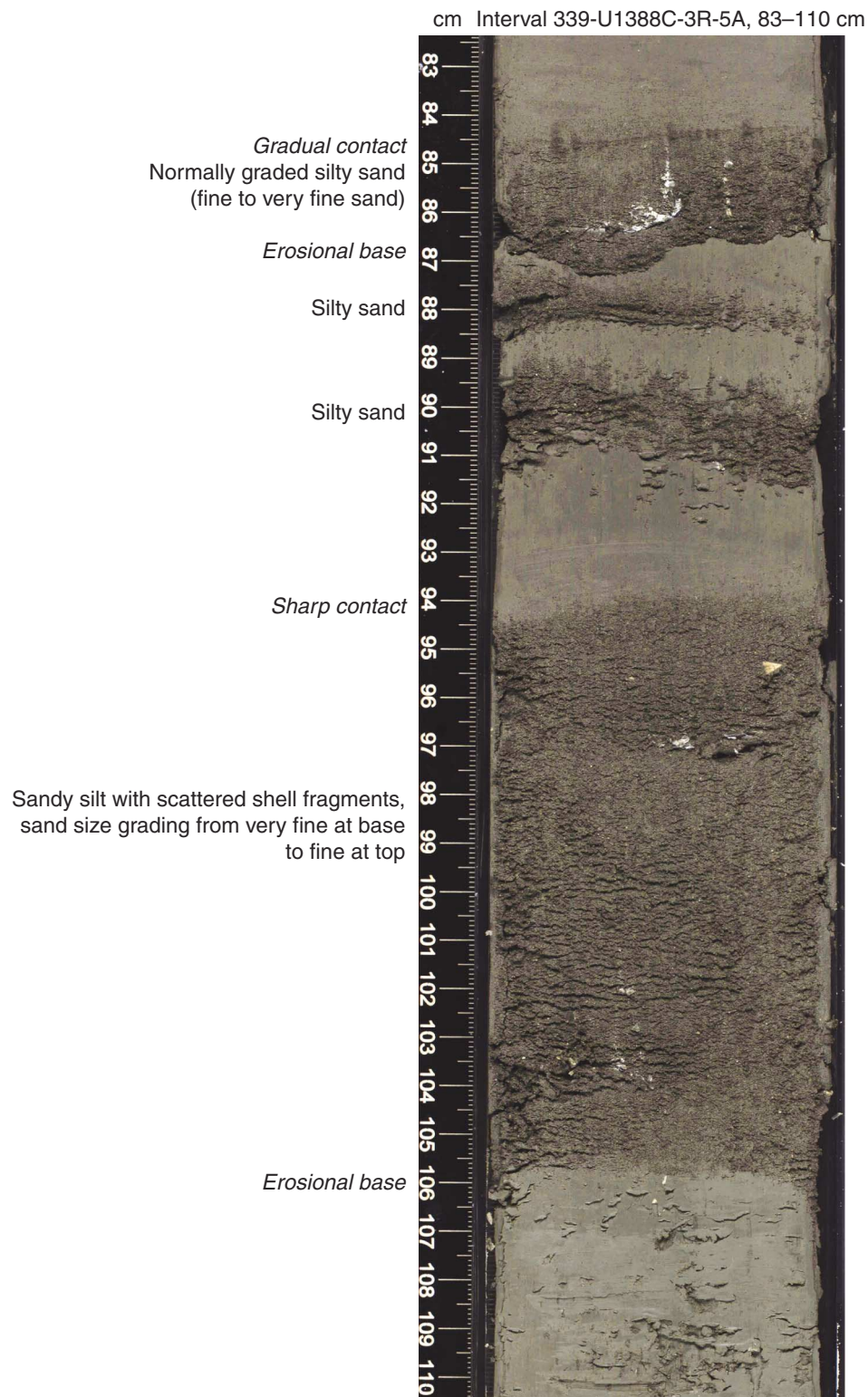


Figure F16. Core image of laminated sand and mud, including light sand laminations interbedded with other sand and mud (Section 339-U1388B-20X-5A).

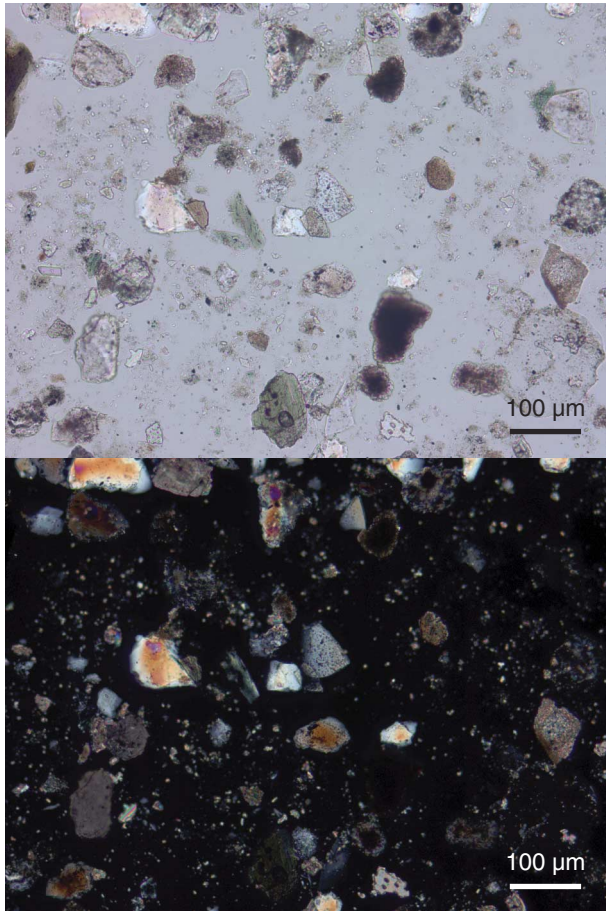


Figure F17. Core images of two likely mass transport deposits. **A.** Slump deposit (Section 339-U1388B-10X-2A). **B.** Debris-flow deposit (Section 339-U1388B-24X-5A).



Figure F18. Photomicrographs of mineral grains in smear slides. The smear slides show relatively similar compositions; identified minerals include quartz and detrital carbonate, which are common. Biogenic carbonate (foraminiferal fragments and nannofossils) and feldspar, mica, dolomite, hypersthene, hornblende, glauconite, and zircon are present to rare. Pyrite is also observed. **A.** Turbidite (Sample 339-U1388B-7X-1, 9 cm). **B.** Contourite (Sample 339-U1388B-10X-1, 100 cm). Upper panels taken under transmitted light; lower panels taken under cross-polarized light.

A Sample 339-U1388B-7X-1A, 9 cm



B Sample 339-U1388B-10X-1A, 100 cm

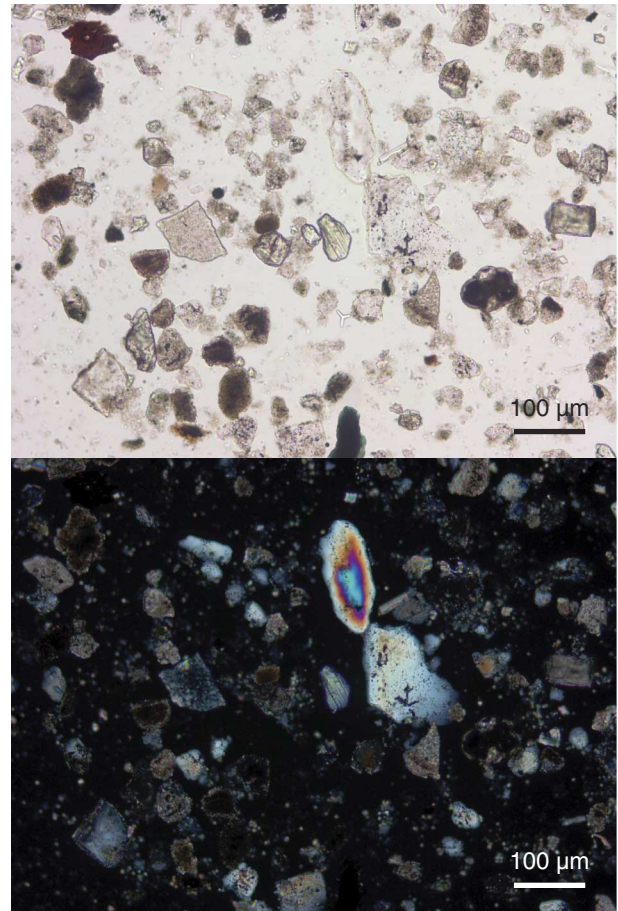


Figure F19. Photographs of three complete, well-preserved gastropods (Samples 339-U1388B-10X-CC and 19X-2-PAL, and 339-U1388A-1H-3A, 48–49 cm).



Scale graduation is 1 mm



Figure F20. XRD peak intensity profiles, Site U1388.

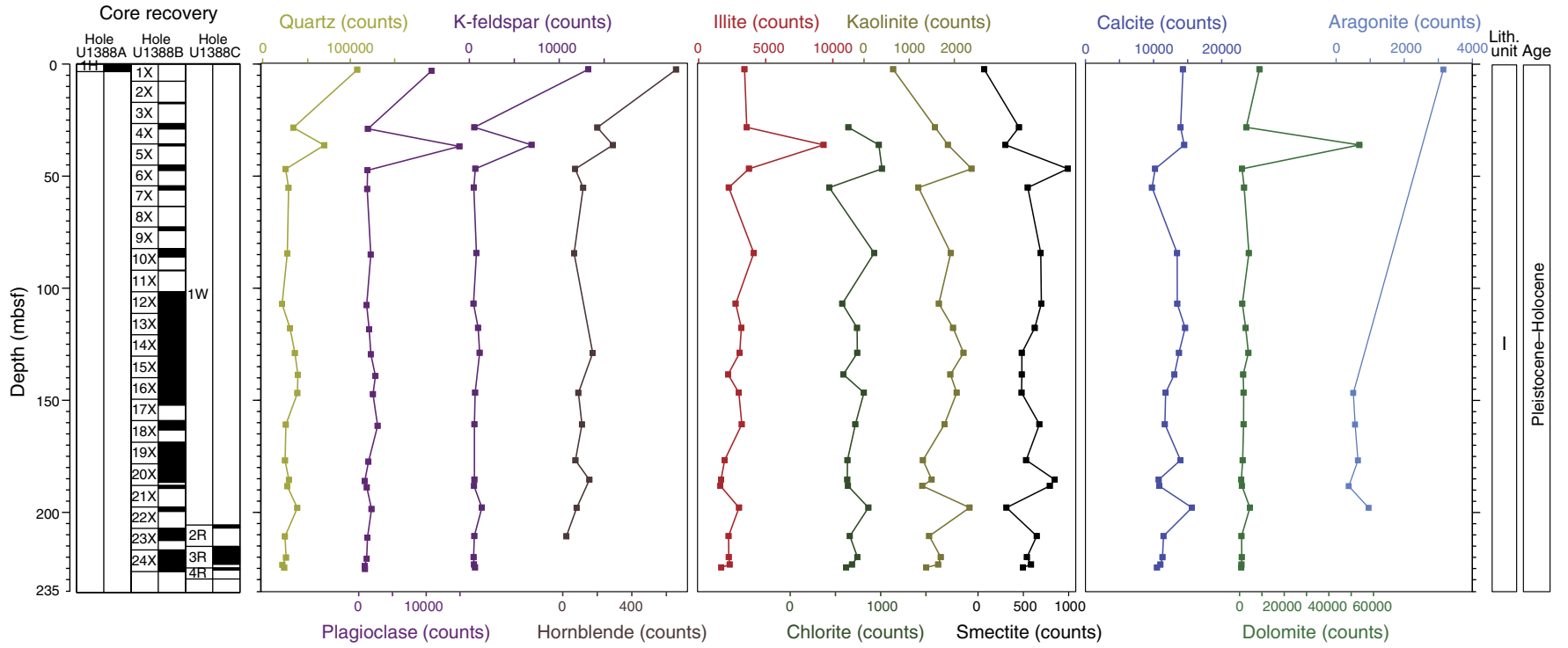


Figure F21. XRD patterns of bulk nonglycolated (black) and ethylene glycolated (red) sediment samples, Site U1388. Downhole changes in clay-mineral abundance have not been quantified, but note that low-angle peak generally shifts to lower angles and becomes more intense as a result of glycolation. This suggests the presence of poorly crystalline smectite.

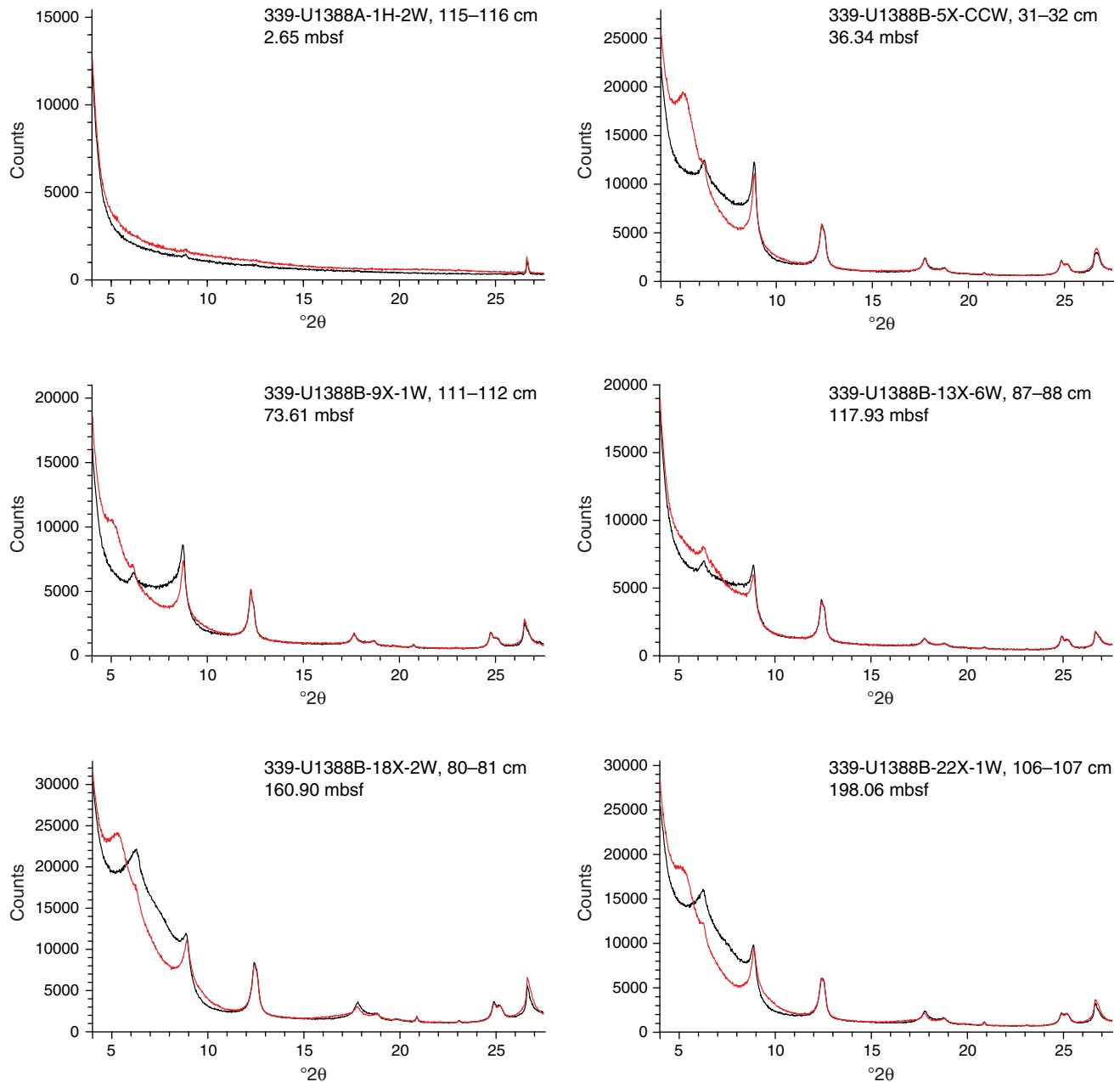




Figure F22. Paleomagnetism after 20 mT AF demagnetization, Site U1388. Blue triangles = discrete sample locations. Yellow circles = component inclinations of discrete samples with maximum angular deviation mostly less than 10°. In Chron columns, black = normal polarity, white = reversed polarity, and gray = zones without a clear magnetostratigraphic interpretation. In Inclination columns, blue dashed lines = expected geocentric axial dipole inclinations at the site latitude during reversed (left) and normal (right) polarities. In Susceptibility columns, gray lines indicate SHMSL susceptibility plus 25×10^{-5} volume SI to better show the comparison with WRMSL susceptibility (black lines). **A.** Hole U1365A. (Continued on next two pages.)

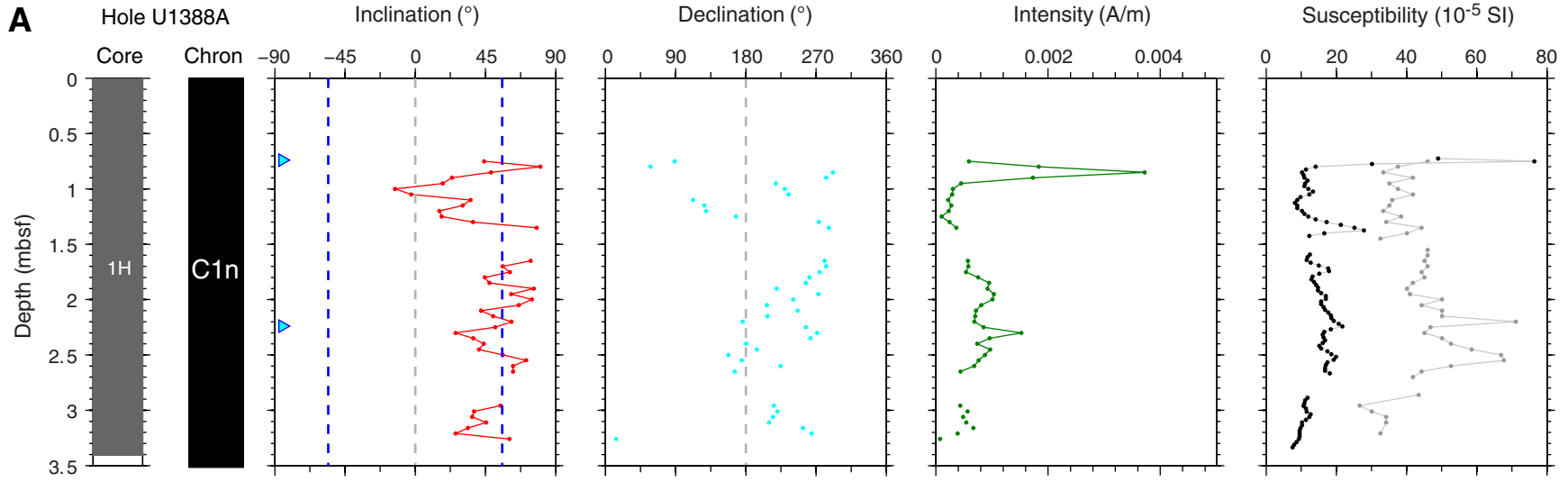




Figure F22 (continued). B. Hole U1388B. (Continued on next page.)

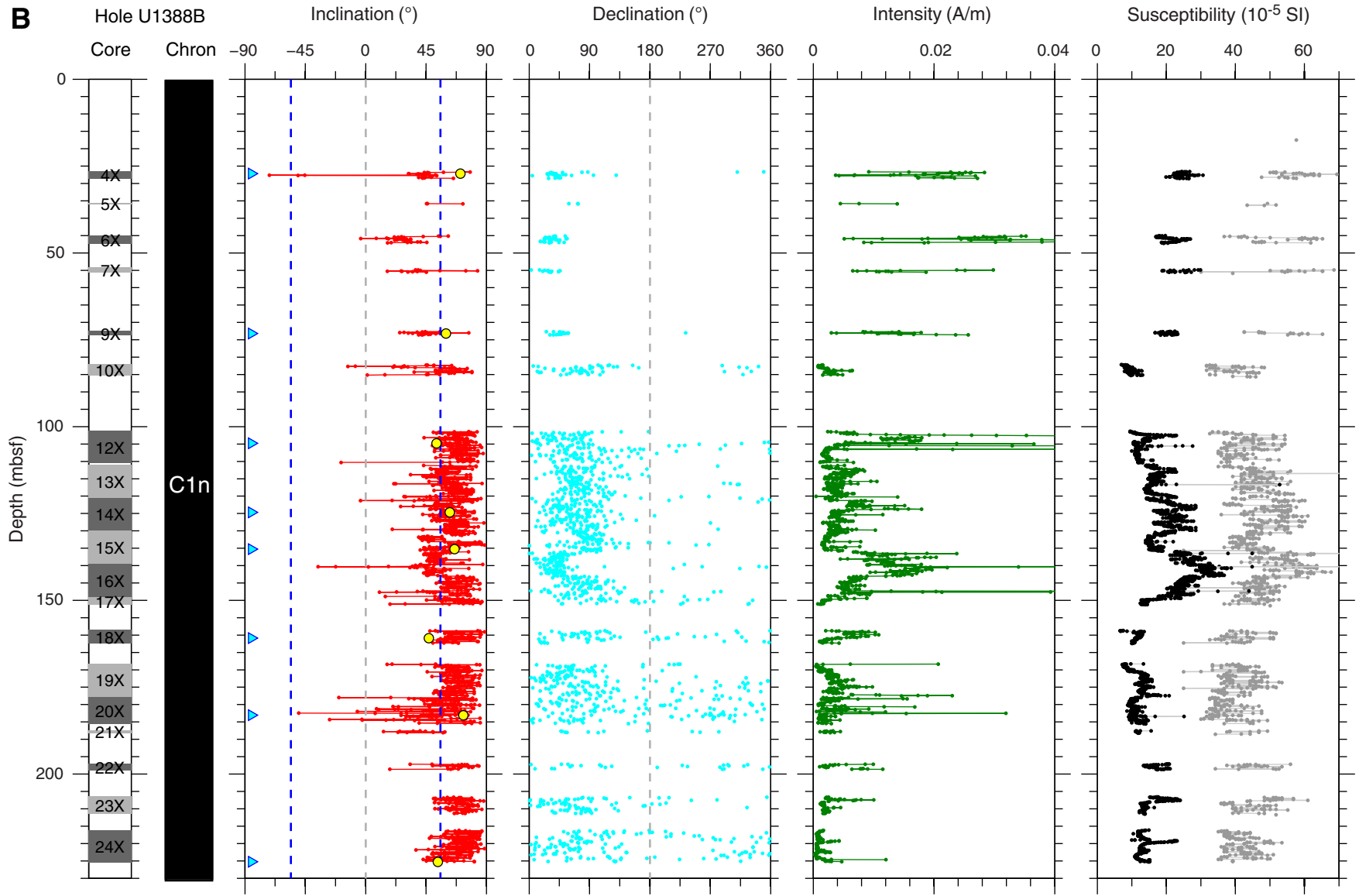




Figure F22 (continued). C. Hole U1388C.

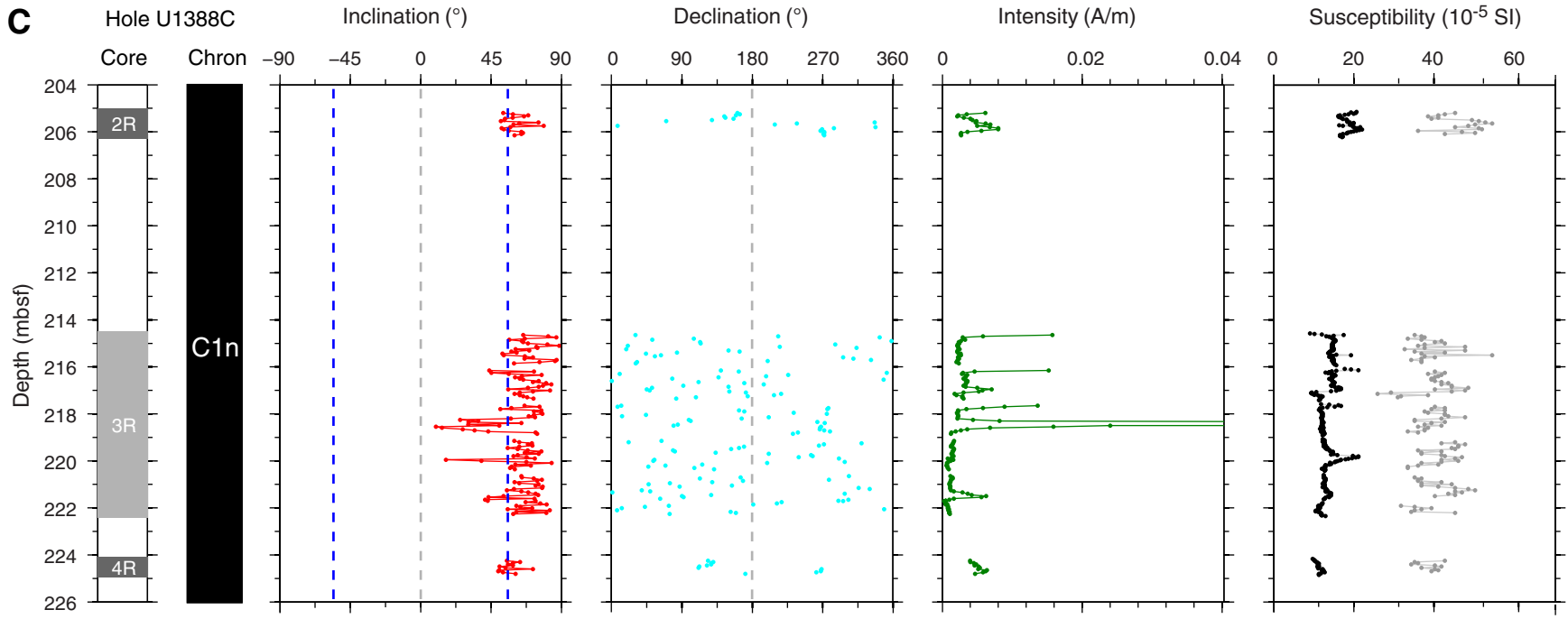


Figure F23. AF demagnetization results for eight discrete samples, Hole U1388B. For each sample, the right plot shows the vector endpoints of paleomagnetic directions measured after each demagnetization treatment on an orthogonal projection (Zijderveld) plot. Squares = horizontal projections, circles = vertical projections. The left plot shows the intensity variation with progressive demagnetization. Orthogonal projection plots illustrate the removal of a step drilling overprint by ~15–20 mT peak field AF demagnetization and a significant amount of ARM acquisition during high-peak field (>55 mT) AF demagnetization, with the remaining magnetization providing a well-resolved characteristic remanent magnetization.

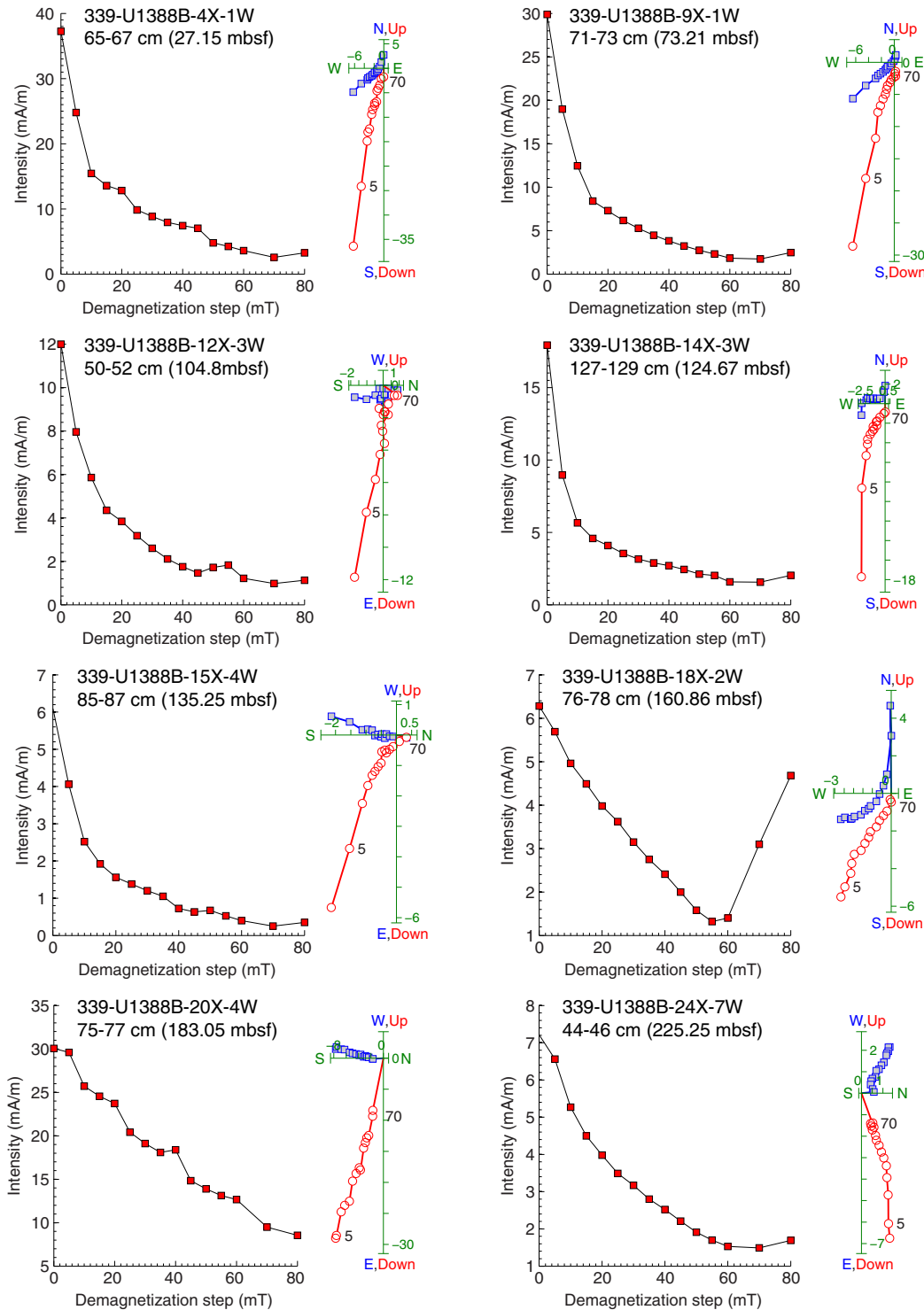


Figure F24. Plots of *P*-wave velocity (PWV) measured in Holes U1388B on the Section-Half Measurement Gantry (discrete samples) set on automatic (solid circles) and manual (open circles) mode, wet bulk density in Holes U1388B (red solid diamonds) and U1388C (open red diamonds) on discrete samples, gamma ray attenuation measured on the Whole Round Multisensor Logger (WRMSL) in Holes U1388A (black line), U1388B (gray line) and U1388C (magenta line), magnetic susceptibility (MS) measured on the WRMSL in Holes U1388A (black line), U1388B (gray line) and U1388C (magenta line), and MS obtained on split cores of Holes U1388B (green dots) and U1388C (light green dots). PP = physical properties.

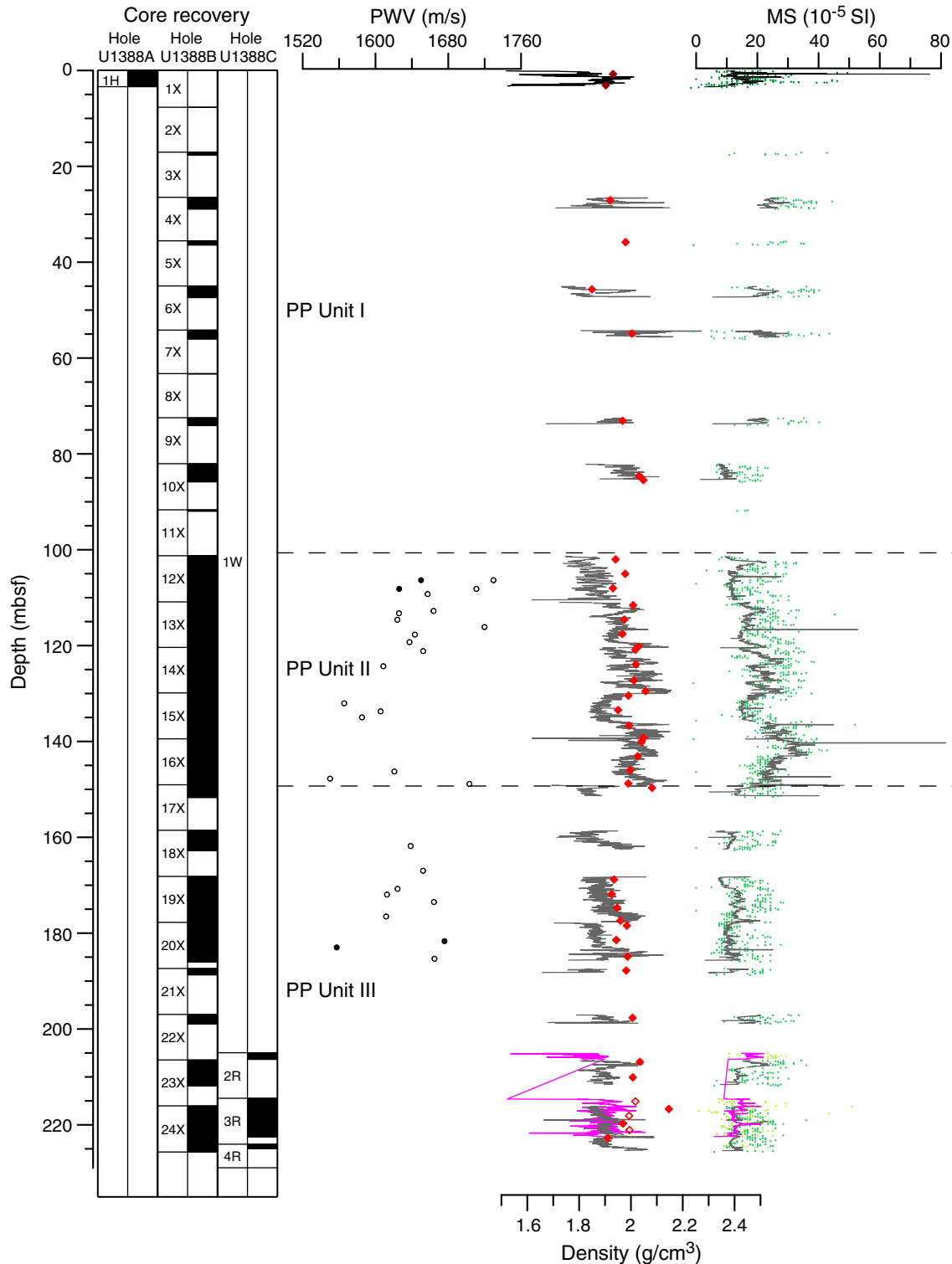


Figure F25. Plots of grain density, moisture content and porosity from discrete measurements. Solid symbols = Hole U1388A and U1388B, open symbols = U1388C. PP = physical properties.

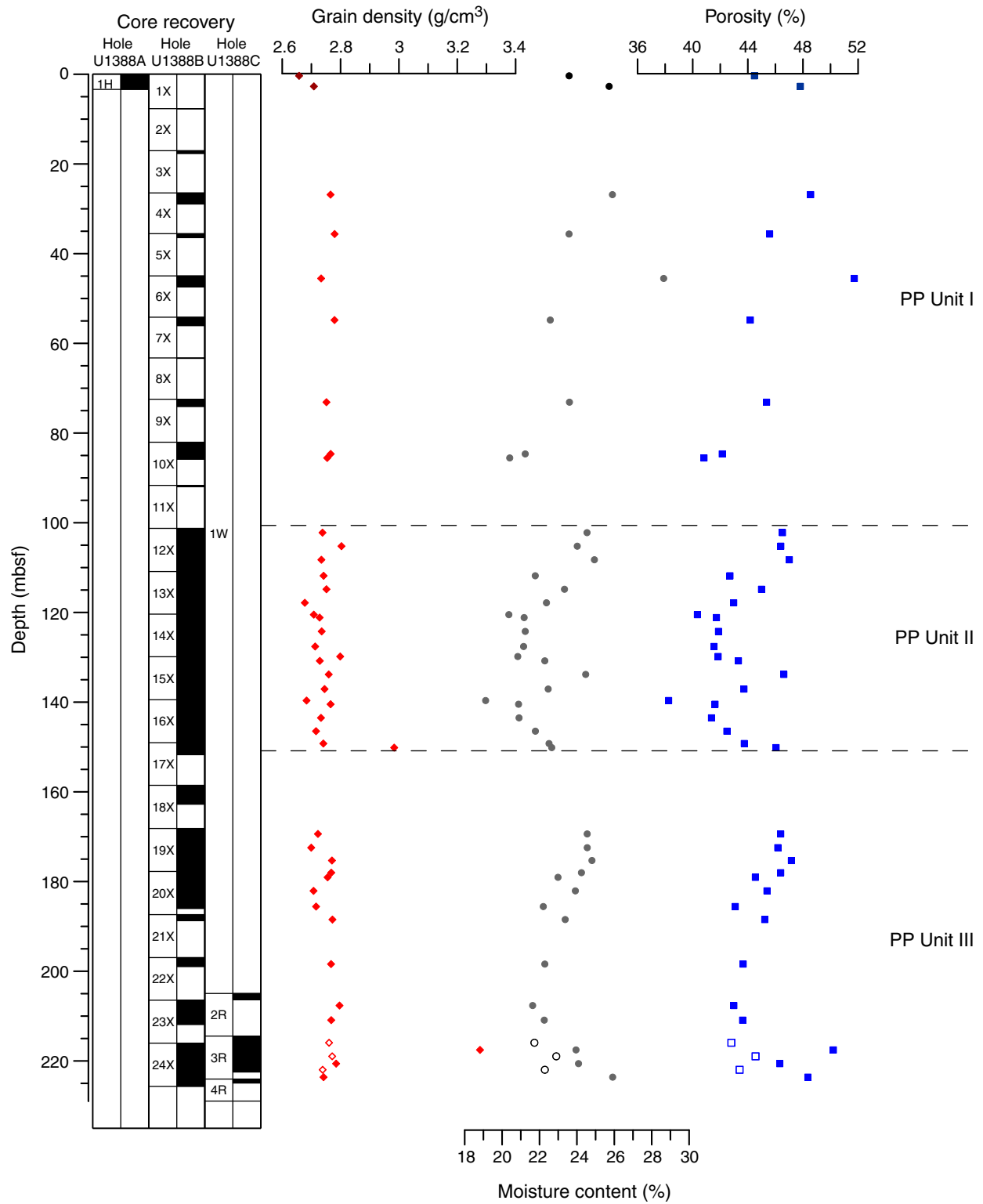


Figure F26. Plots of downhole distribution of color reflectance (L^* , a^*) and natural gamma ray (NGR) measurements in Holes U1388A–U1388C. Heavy lines = Hole U1388A, dark lines = Hole U1388B, light lines = Hole U1388C. PP = physical properties.

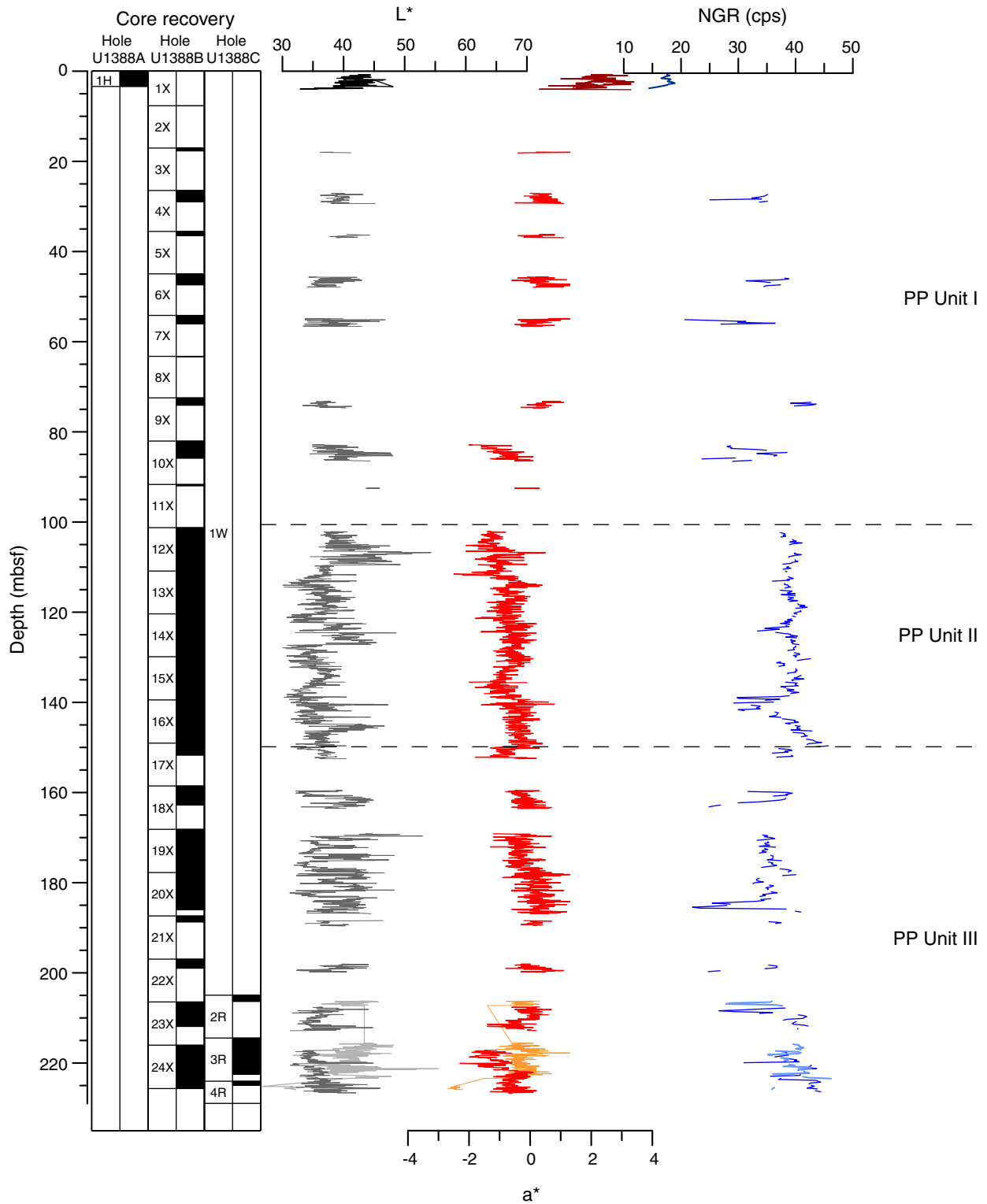


Figure F27. Plot of headspace gas analyses for volatile hydrocarbons, Site U1388.

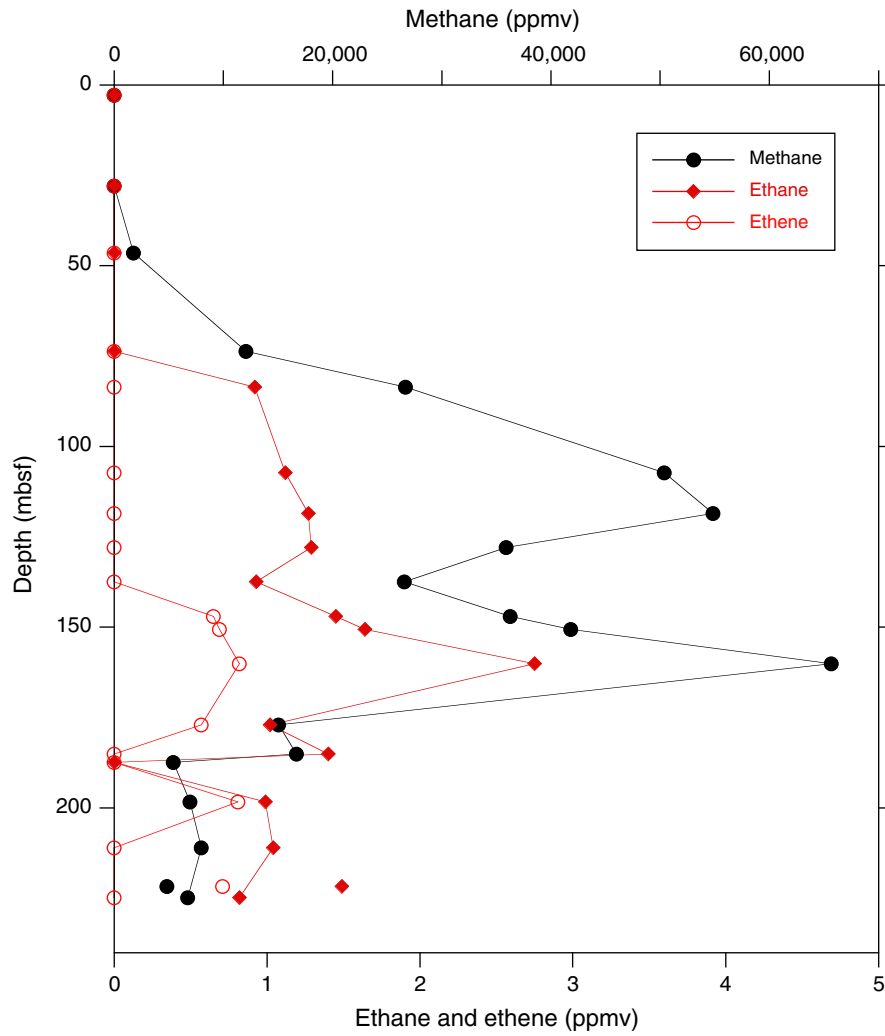


Figure F28. A–C. Plots of calculated total organic carbon (TOC), total nitrogen (TN), and C/N ratio, Holes U1388A (solid circle) and U1388B (open circles).

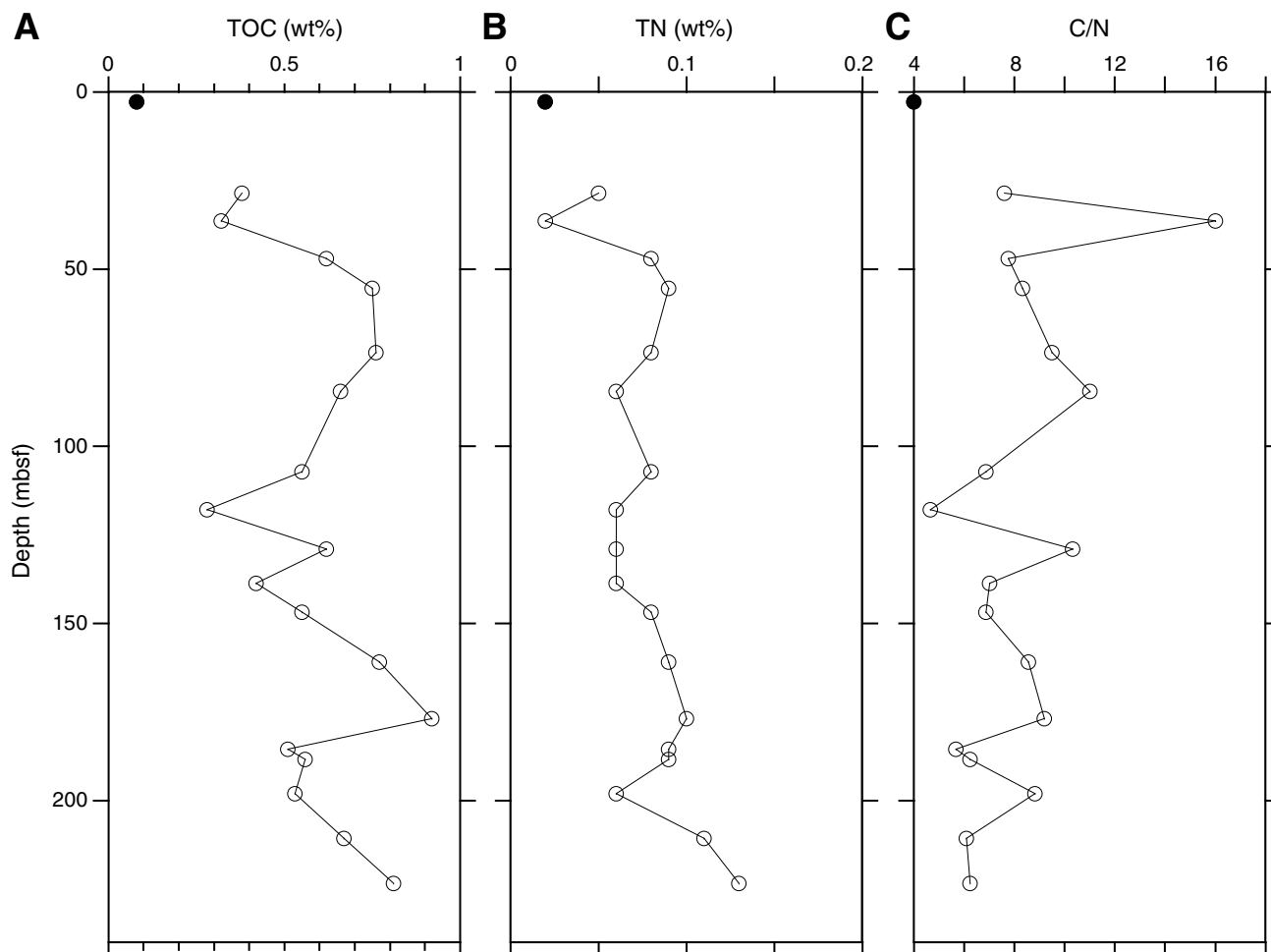




Figure F29. Plots of (A–C) interstitial water sulfate, alkalinity, ammonium, and (D) hydrocarbons (open circles = methane, solid circles = ethene, diamonds = ethane), Hole U1385B.

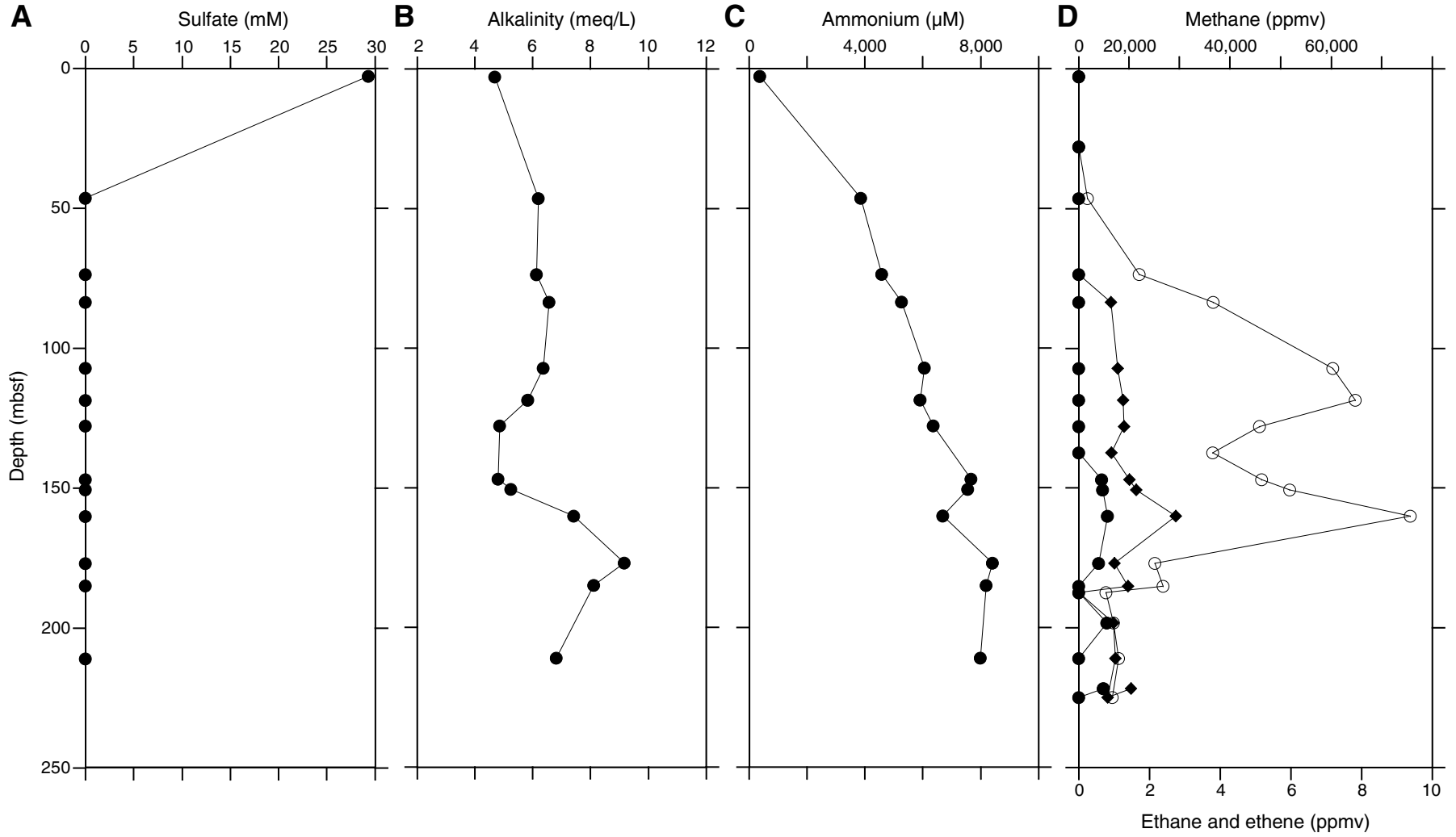


Figure F30. Plots of interstitial water calcium, magnesium, and potassium, Site U1388.

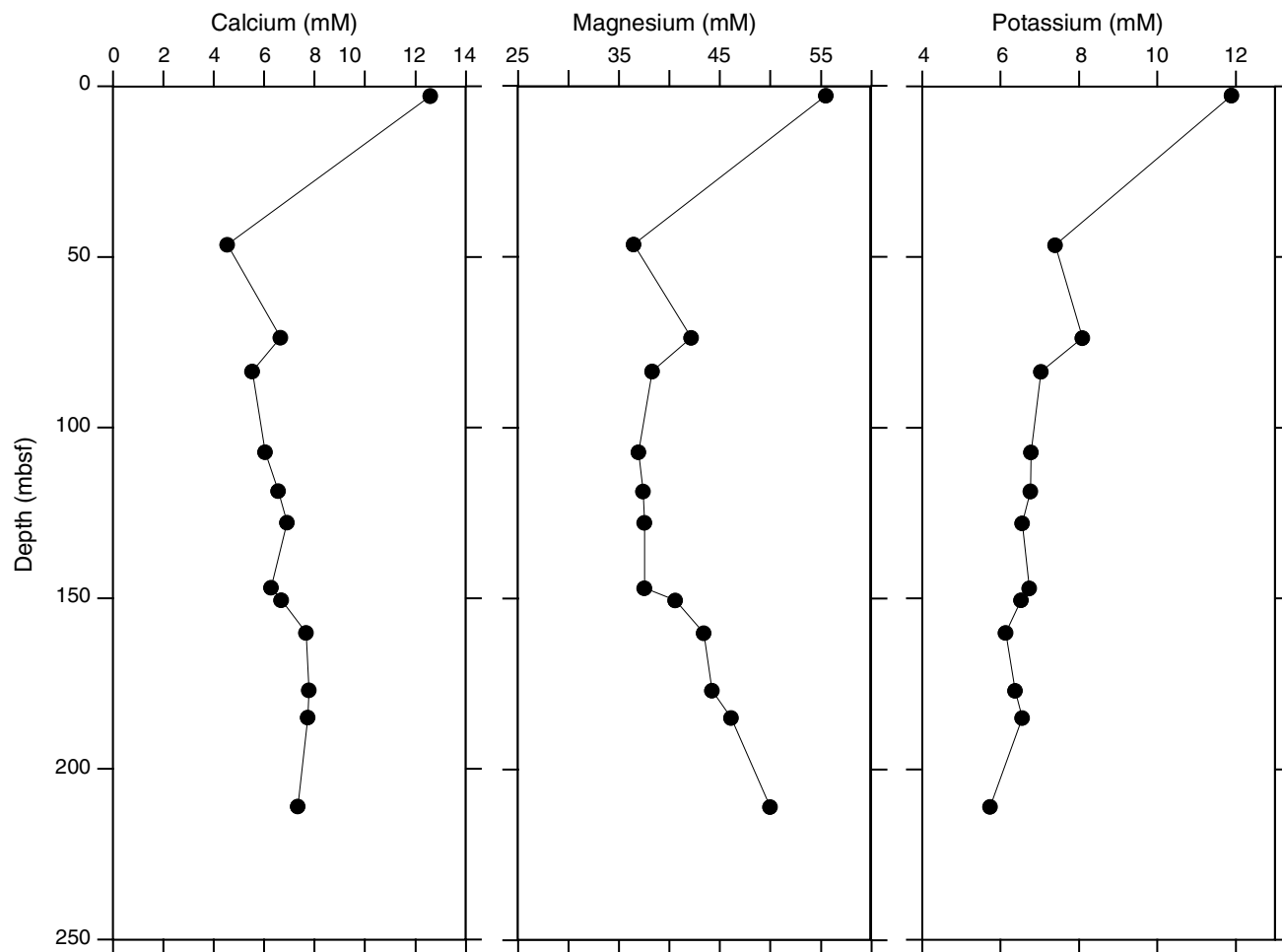


Figure F31. A–C. Plots of interstitial water sodium, chloride, and Na^+/Cl^- ratio, Site U1388. Dotted line indicates seawater Na^+/Cl^- ratio.

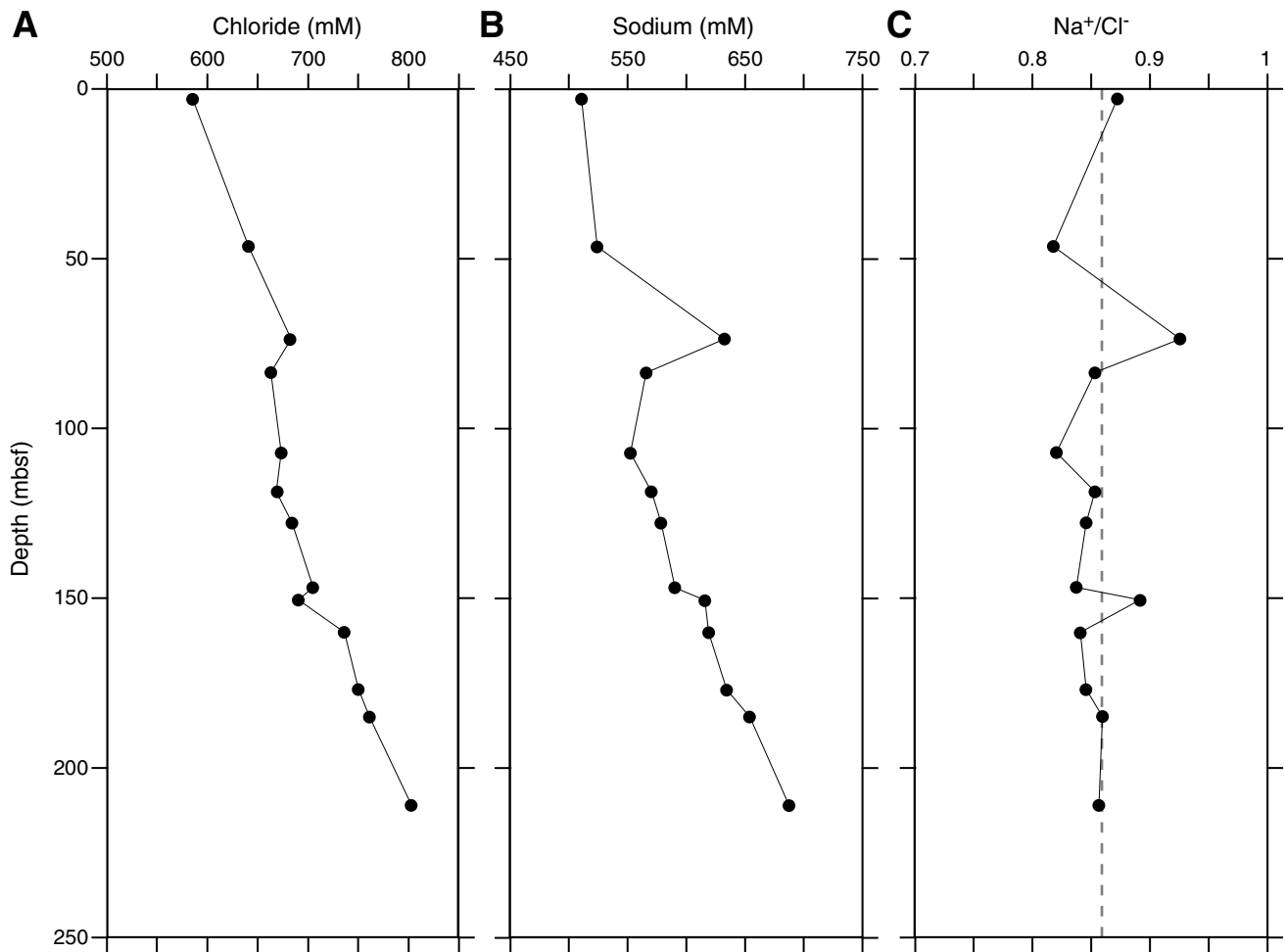




Figure F32. Plots of interstitial water strontium, barium, lithium, boron, and silicon, Site U1388.

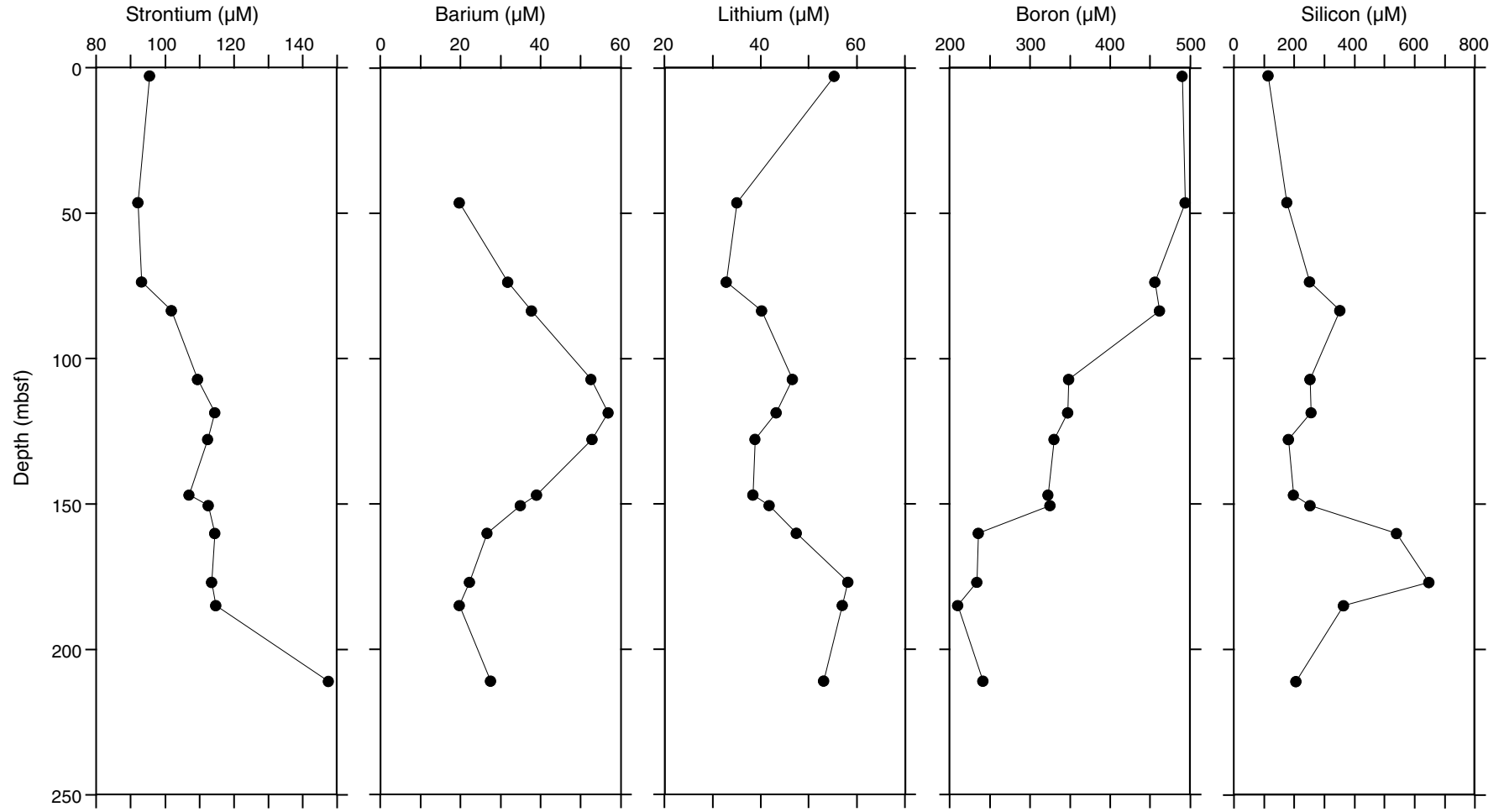


Figure F33. Plots of various elemental concentrations vs. chloride, Site U1388.

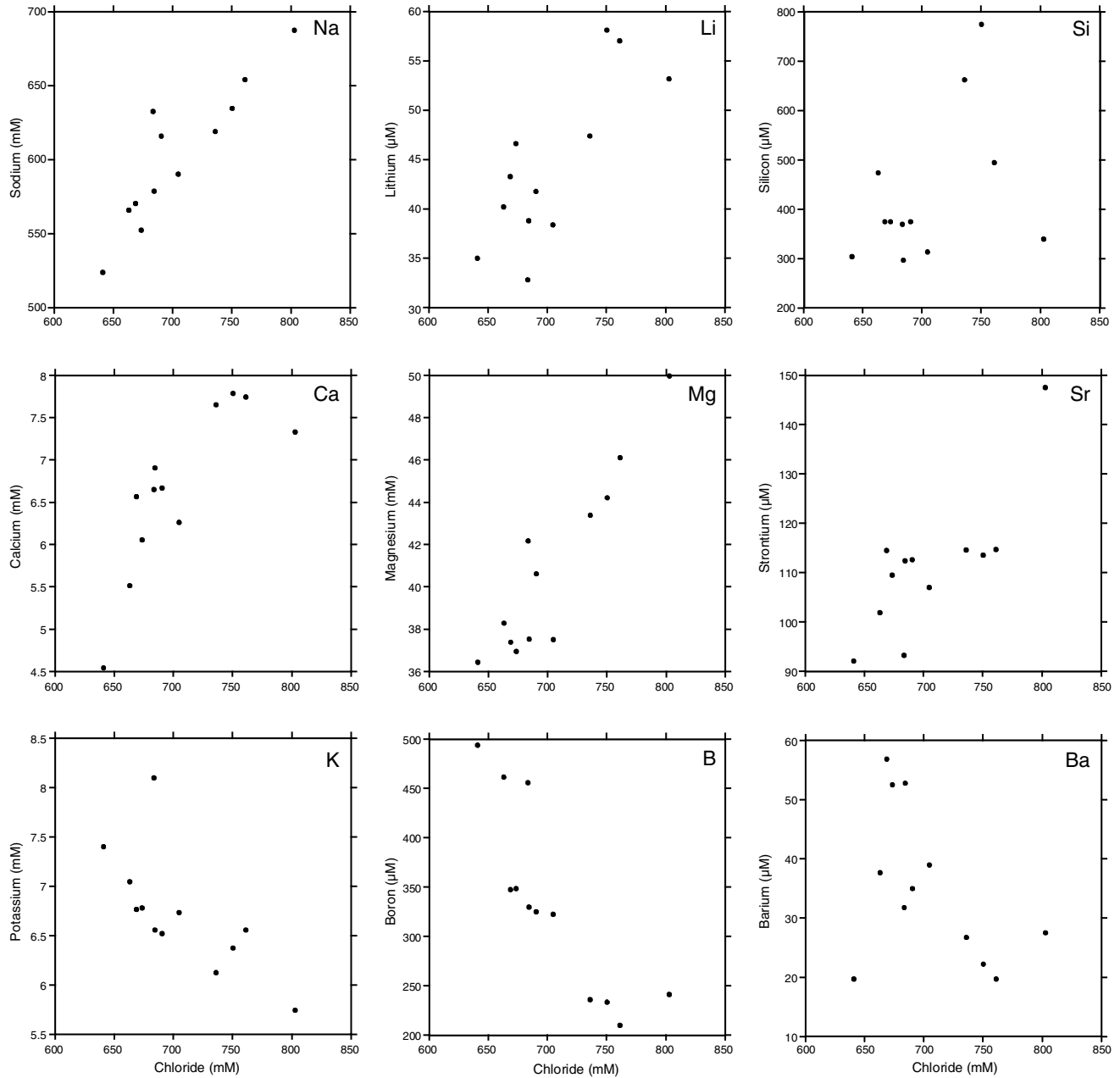


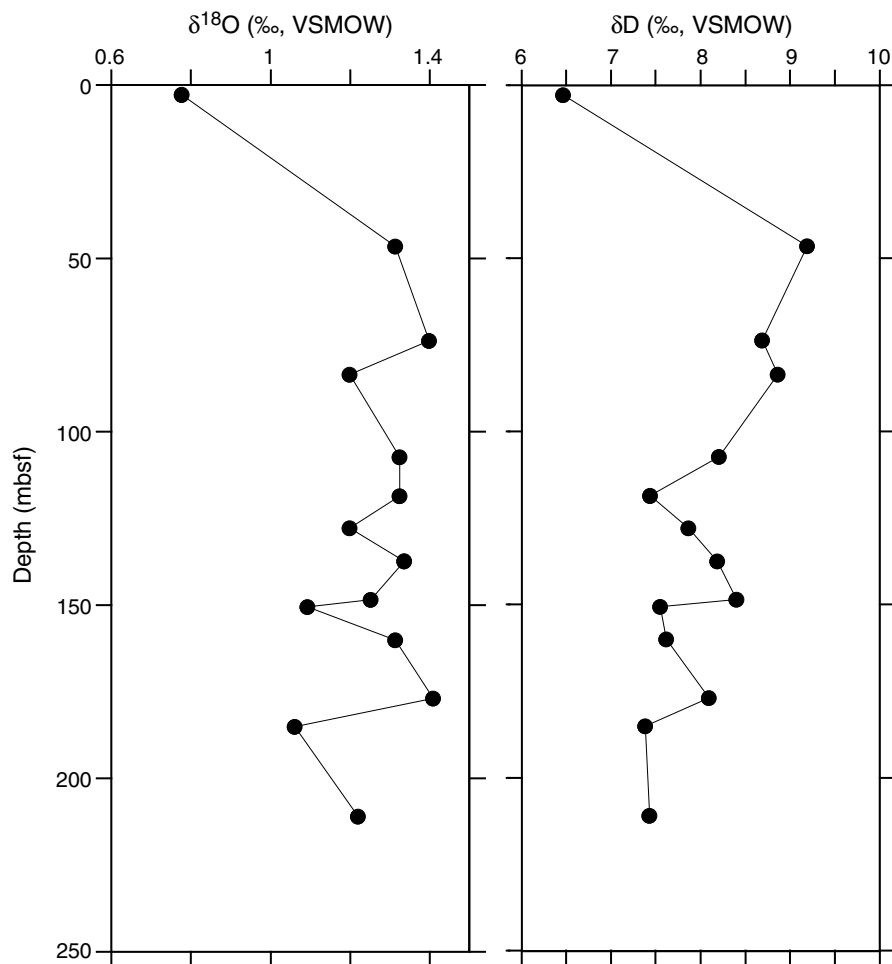
Figure F34. Plots of interstitial water stable isotopes, Site U1388. VSMOW = Vienna standard mean ocean water.

Figure F35. Plot of $\delta^{18}\text{O}$ vs. δD , Site U1388. VSMOW = Vienna standard mean ocean water.

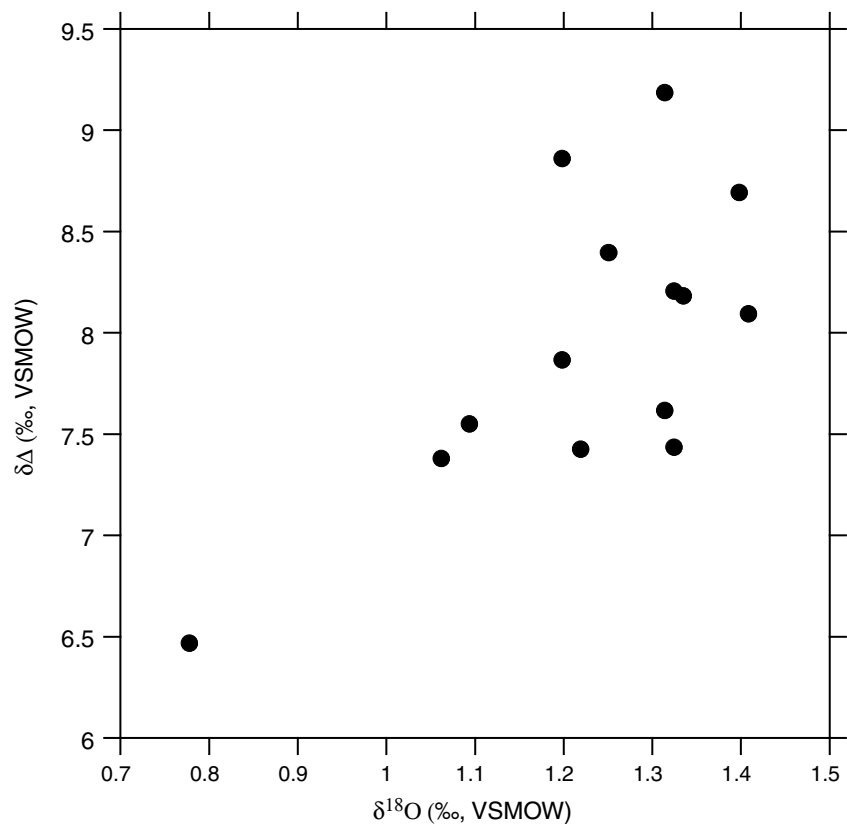


Table T1. Coring summary, Site U1388. (Continued on next page.)

Hole U1388A

Latitude: 36°16.1378'N
 Longitude: 6°47.6602'W
 Time on hole (d): 0.8
 Seafloor (drill pipe measurement below rig floor, m DRF): 669 (APC mudline)
 Distance between rig floor and sea level (m): 11.3
 Water depth (drill pipe measurement from sea level, mbsl): 657.7
 Total penetration (drilling depth below seafloor, m DSF): 3.4
 Total length of cored section (m): 3.4
 Total core recovered (m): 3.64
 Core recovery (%): 107.06
 Total number of cores: 1

Hole U1388B

Latitude: 36°16.1383'N
 Longitude: 6°47.6413'W
 Time on hole (d): 1.4
 Seafloor (drill pipe measurement below rig floor, m DRF): 674.4
 Distance between rig floor and sea level (m): 11.3
 Water depth (drill pipe measurement from sea level, mbsl): 663.1
 Total penetration (drilling depth below seafloor, m DSF): 225.7
 Total length of cored section (m): 225.7
 Total core recovered (m): 106.54
 Core recovery (%): 47.2
 Total number of cores: 24

Hole U1388C

Latitude: 36°16.1495'N
 Longitude: 6°47.6411'W
 Time on hole (d): 1.2
 Seafloor (drill pipe measurement below rig floor, m DRF): 674.0
 Distance between rig floor and sea level (m): 11.3
 Water depth (drill pipe measurement from sea level, mbsl): 662.7
 Total penetration (drilling depth below seafloor, m DSF): 229
 Total length of cored section (m): 24
 Total core recovered (m): 10.36
 Core recovery (%): 43.17
 Total number of cores: 3

Site U1388 totals

Number of cores: 28
 Penetration (m): 458.1
 Cored (m): 253.1
 Recovered (m): 120.54 (47.6%)

Core	Date (2011)	Time (h)	Depth DSF (m)			Depth CSF (m)			Curated length (m)	Recovery (%)
			Top of cored interval	Bottom of cored interval	Interval advanced (m)	Top of recovered core	Bottom of recovered core	Length of core recovered (m)		
339-U1388A- 1H	18 Dec	1510	0.0	3.4	3.4	0.0	3.64	3.64	3.64	107
				Advanced total:	3.4					
				Total interval cored:	3.4					
339-U1388B- 1X	19 Dec	0930	0.0	7.7	7.7	0.0	0.00	0.00	0.00	0
2X	19 Dec	1030	7.7	17.1	9.4	7.7	7.73	0.03	0.03	0
3X	19 Dec	1135	17.1	26.5	9.4	17.1	17.75	0.65	0.65	7
4X	19 Dec	1230	26.5	35.6	9.1	26.5	29.00	2.50	2.50	27
5X	19 Dec	1310	35.6	45.0	9.4	35.6	36.50	0.90	0.90	10
6X	19 Dec	1345	45.0	54.2	9.2	45.0	47.47	2.47	2.47	27
7X	19 Dec	1425	54.2	63.3	9.1	54.2	56.14	1.94	1.94	21
8X	19 Dec	1515	63.3	72.5	9.2	63.3	63.40	0.10	0.10	1
9X	19 Dec	1605	72.5	82.1	9.6	72.5	74.18	1.68	1.68	18
10X	19 Dec	1650	82.1	91.7	9.6	82.1	85.92	3.82	3.82	40
11X	19 Dec	1730	91.7	101.3	9.6	91.7	92.06	0.36	0.36	4
12X	19 Dec	1815	101.3	110.9	9.6	101.3	110.93	9.63	9.63	100
13X	19 Dec	1915	110.9	120.4	9.5	110.9	120.71	9.81	9.81	103
14X	19 Dec	1955	120.4	129.9	9.5	120.4	130.19	9.79	9.79	103
15X	19 Dec	2025	129.9	139.5	9.6	129.9	139.86	9.96	9.96	104
16X	19 Dec	2100	139.5	149.1	9.6	139.5	149.32	9.82	9.82	102
17X	19 Dec	2140	149.1	158.6	9.5	149.1	151.79	2.69	2.69	28
18X	19 Dec	2240	158.6	168.2	9.6	158.6	162.82	4.22	4.22	44

Table T1 (continued).

Core	Date (2011)	Time (h)	Depth DSF (m)			Depth CSF (m)			Length of core recovered (m)	Curated length (m)	Recovery (%)
			Top of cored interval	Bottom of cored interval	Interval advanced (m)	Top of recovered core	Bottom of recovered core	Length of core recovered (m)			
19X	20 Dec	0005	168.2	177.8	9.6	168.2	178.02	9.82	9.82	102	
20X	20 Dec	0110	177.8	187.4	9.6	177.8	186.08	8.28	8.28	86	
21X	20 Dec	0225	187.4	197.0	9.6	187.4	188.80	1.40	1.40	15	
22X	20 Dec	0335	197.0	206.5	9.5	197.0	199.04	2.04	2.04	21	
23X	20 Dec	0530	206.5	216.1	9.6	206.5	211.96	5.46	5.46	57	
24X	20 Dec	0645	216.1	225.7	9.6	216.1	225.73	9.63	9.63	100	
				Advanced total:	225.7						
				Total interval cored:	225.7						
339-U1388C-											
1W	21 Dec	0600				****Drilled from 0 to 205.0 m DSF without coring****					
2R	21 Dec	0715	205.0	214.5	9.5	205.0	206.43	1.43	1.43	15	
3R	21 Dec	0835	214.5	224.1	9.6	214.5	222.55	8.05	8.05	84	
4R	21 Dec	1355	224.1	229.0	4.9	224.1	224.98	0.88	0.88	18	
				Advanced total:	229.0						
				Total interval cored:	24.0						

DRF = drilling depth below rig floor, DSF = drilling depth below seafloor, CSF = core depth below seafloor. H = advanced piston coring system, X = extended core barrel system, R = rotary core barrel system, W = washed interval. Time is Universal Time Coordinated.

Table T2. Sediment textures, compositions, and lithology names determined by smear slide, Site U1388.

	Texture (%)			Composition (%)				Comments	Also reported
	Sand	Silt	Clay	Siliciclastic	Detrital carbonate	Biogenic carbonate	Biogenic silica		
Sand (with biogenic carbonate)	75–95	1–15	0–10	60–95	2–30	0–30	0–2	Subangular to well rounded quartz, feldspars, mica, rock fragments, zircon, opaques, heavy minerals, glauconite, foraminifers, and sometimes many pyrite nodules	
Silty sand with biogenic carbonate (calcareous silty sand)	40–70	20–40	10–20	30–60	30–50	5–20	0–2	Quartz, opaques, feldspars, mica, zircon, detrital dolomite, hornblende, glauconite, nannofossils, foraminifers, and calcareous and sponge spicules	
Sandy silt with biogenic carbonate (calcareous sandy silt)	20–40	45–60	15–20	45–60	20–35	20	0–4	Quartz, mica, opaques, feldspars, glauconite, pyrite, detrital and authigenic dolomite, nannofossils, foraminifers, and sponge and calcareous spicules	
Silty mud with biogenic carbonate (calcareous silty mud)	5–20	35–70	30–40	25–50	25–55	20–35	0–4	Opagues, mica, feldspars, heavy minerals, zircon, glauconite, detrital and authigenic dolomite, pyrite, nannofossils, foraminifers, and calcareous and sponge spicules	U1388C-3R-2, 25 cm; diatoms and radiolarians
Mud with biogenic carbonate	0–10	20–40	55–80	20–60	25–55	15–25	0–2	Mica, zircon, glauconite, opaques, heavy minerals, detrital and authigenic dolomite, nannofossils, and sponge spicule fragments	U1388B-19X-1, 9 cm; diatom and radiolarian fragments
Nannofossil mud (mud with nannofossils)	0–5	20–30	70–80	35–55	30–40	15–25		Pyrite, nannofossils, and calcareous and sponge spicules	U1388B-24X-5, 138 cm; wood fragments

Table T3. XRD peak intensities of minerals from bulk sediment, Site U1388.

Core, section, interval (cm)	Depth (mbsf)	Total intensity (counts)	Quartz (counts)	Calcite (counts)	K-feldspar (counts)	Plagioclase (counts)	Dolomite (counts)	Chlorite (counts)	Kaolinite (counts)	Illite (counts)	Smectite (counts)	Hornblende (counts)	Augite (counts)	Pyrite (counts)	Aragonite (counts)
339-															
U1388A-1H-2, 115–116	2.65	162,621	107,577	14,225	13,229	10,773	8,893	NA	659	3,421	67	656	NA	NA	3,121
U1388B-4X-2, 50–51	28.50	60,738	34,942	13,870	481	1,295	3,003	648	1,581	3,588	450	201	NA	679	NA
U1388B-5X-CC, 31–32	36.34	172,681	70,098	14,409	6,889	14,939	53,594	983	1,866	9,311	301	291	NA	NA	NA
U1388B-6X-2, 48–49	46.98	47,298	26,081	10,078	595	1,235	1,093	1,018	2,386	3,751	988	73	NA	NA	NA
U1388B-7X-1, 114–115	55.34	47,548	29,517	9,609	420	1,185	2,037	438	1,216	2,246	547	119	NA	214	NA
U1388B-10X-2, 97–99	84.57	55,753	28,088	13,358	713	1,713	4,153	932	1,927	4,113	689	67	NA	NA	NA
U1388B-12X-4, 131–132	107.11	44,351	22,159	13,375	395	1,102	1,242	581	1,666	2,759	696	NA	376	NA	NA
U1388B-13X-6, 87–88	117.93	57,381	31,184	14,545	906	1,479	2,737	744	1,978	3,184	624	NA	NA	NA	NA
U1388B-14X-6, 116–117	129.06	63,775	36,715	13,630	1,080	1,733	3,946	746	2,209	3,060	482	174	NA	NA	NA
U1388B-15X-6, 130–131	138.70	66,468	40,042	12,945	NA	2,413	1,626	593	1,919	2,194	482	NA	4,254	NA	NA
U1388B-16X-5, 133–134	146.83	62,547	39,546	11,639	572	2,045	1,824	819	2,058	2,997	479	92	NA	NA	476
U1388B-18X-2, 80–81	160.90	50,070	26,442	11,531	497	2,745	1,805	725	1,790	3,218	675	112	NA	NA	530
U1388B-19X-6, 119–120	176.89	47,769	25,491	13,855	NA	1,370	1,393	638	1,315	1,941	529	74	NA	548	614
U1388B-20X-6, 50–51	185.57	47,595	29,914	10,612	494	820	796	636	1,507	1,670	844	155	NA	147	NA
U1388B-21X-CC, 12–13	188.37	46,139	28,106	10,697	447	1,128	1,061	644	1,301	1,622	790	NA	NA	NA	343
U1388B-22X-1, 106–107	198.06	71,266	39,446	15,555	1,322	1,826	4,624	869	2,342	3,011	312	82	949	NA	928
U1388B-23X-3, 125–126	210.75	44,635	25,426	11,327	481	1,220	877	664	1,452	2,234	646	22	NA	286	NA
U1388C-3R-4, 114–115	220.14	46,061	26,678	11,176	407	1,111	998	747	1,708	2,248	538	NA	450	NA	NA
U1388B-24X-5, 131–132	223.41	41,169	22,490	10,871	447	824	848	688	1,650	2,318	583	NA	406	NA	NA
U1388C-4R-1, 64–65	224.74	41,585	24,522	10,357	565	863	796	623	1,388	1,691	494	NA	NA	286	NA

NA = no peak detected.



Table T4. Biostratigraphic datums, Hole U1388B.

Event	Reference	Age (Ma)	Depth (mbsf)		
			Top	Bottom	Mean
FO <i>Emiliana huxleyi</i>	Raffi et al., 2006	0.26	47.47	56.14	51.81
LO <i>Pseudoemiliana lacunosa</i>	Raffi et al., 2006	0.46	162.82	178.02	170.42

FO = first occurrence, LO = last occurrence.

Table T5. Abundance of nannofossils, Site U1388.

Core, section, interval (cm)	Depth (mbsf)	Preservation		Abundance																										
				<i>Braarudosphaera bigelowii</i>	<i>Calcidiscus leptoporus</i> (<5 µm)	<i>Calcidiscus leptoporus</i> (>8 µm)	<i>Calcidiscus leptoporus</i> (5–8 µm)	<i>Coccolithus pelagicus</i> spp. <i>azorinus</i>	<i>Coccolithus pelagicus</i> spp. <i>braarudii</i>	<i>Coccolithus pelagicus</i> ssp. <i>pelagicus</i>	<i>Emiliana huxleyi</i> (<4 µm)	<i>Emiliana huxleyi</i> (>4 µm)	<i>Gephyrocapsa caribbeanica</i>	Medium <i>Gephyrocapsa</i> group	<i>Gephyrocapsa oceanica</i> (>5 µm)	<i>Gephyrocapsa oceanica</i> (<5 µm)	<i>Gephyrocapsa omega</i>	<i>Gephyrocapsa</i> spp. (<3 µm)	<i>Helicosphaera carteri</i>	<i>Helicosphaera sellii</i>	<i>Pontosphaera</i> spp.	<i>Pseudoemiliana lacunosa</i>	<i>Reticulofenestra asanoi</i> (>6 µm)	<i>Reticulofenestra asanoi</i> (<6 µm)	<i>Reticulofenestra minuta</i> (<3 µm)	<i>Rhabdosphaera</i> spp.	<i>Syracosphaera</i> spp.	<i>Umbilicosphaera sibogae</i>		
339-U1388A-1H-CC	3.64	M	R			R		R	P	F				P	R			R												R
339-U1388B-2X-CC	7.73	M	A	P	F	F		F	F		R		C			D	F	F		C			D							
3X-CC	17.73	M	C			R		R	R	C				R	R			C	R										R	
4X-CC	29.00	M	C			R				R								R	R											
5X-CC	36.50	M	R			R					P							R												
6X-CC	47.47	P	P															P												
7X-CC	56.14	M	F			P									P			P												
8X-CC	63.40	M	A			R				R				R				D	R					A			R			
9X-CC	74.18		B																											
10X-CC	85.92	M	A												C		A	F					A							
11X-1, 5	91.75	M	A				F	F	F		F	C	C	F	F	C	F	F		F			C							
12X-CC	110.93	G	A									F	C			D	F		F				D			F				
13X-CC	120.71	M	VA					F	F					C	C	F		C	F				C							
14X-CC	130.19	G	A					R						C	C	A		A					A			F	F			
15X-CC	139.86	G	A			R		R	R		F			C	C	A	R						A	R		F				
16X-CC	149.32	G	VA					R				F		F	F	A							A			R				
17X-CC	151.79	M	VA			R		R	R		C			C	C	A							A			F				
18X-CC	162.82	M	C			R		R			R			R	R	F							F							
19X-CC	178.02	M	VA			P		R	R		A		R	F	D	R	R	F					F			F				
20X-CC	185.91	M	A			R		F	F		C	F	C	A	R	R	R		R	R			F			R	R			
21X-CC	188.66	M	F								R	R	R	R	R					P			P							
22X-CC	199.04	M	C			R					R	F	R	C	R								R							
23X-CC	211.87	G	A			F		F		F		C		A	R	C							P	R		F				
24X-CC	225.73	G	A	R		R		R	R					F	F	A	F						R	A		R	R			
339-U1388C-3R-CC	222.55	M	VA			R				F	P	R	F	F	R	D	R			C			D							

Preservation: G = good, M = medium. Abundance: D = dominant, VA = very abundant, A = abundant, C = common, F = few, R = rare, P = present, B = barren. See "Biostratigraphy" in the "Methods" chapter (Expedition 339 Scientists, 2013b) for abundance and preservation definitions.





Table T6. Abundance of planktonic foraminifers, Site U1388.

Core section,	Depth (mbsf)		Pteropod abundance			Planktonic foraminifer abundance										Comment																
	Top	Bottom	B	R	VG	<i>Globigerina bulloides</i>	<i>Globigerinoides ruber</i> (white)	<i>Globigerinoides sacculifer</i>	<i>Globigerinoides trilobus</i>	<i>Globorotalia inflata</i>	<i>Globorotalia hirsuta</i> (dex)	<i>Globorotalia hirsuta</i> (sin)	<i>Globorotalia crassaformis</i> s.l. (dex)	<i>Globorotalia crassaformis</i> s.l. (sin)	<i>Globorotalia truncatulinoides</i> (dex)		<i>Globorotalia truncatulinoides</i> (sin)	<i>Beella digitata</i>	<i>Globigerina calida</i>	<i>Globigerina falconensis</i>	<i>Globigerinella siphonifera</i>	<i>Globigerinita glutinata</i>	<i>Globigerinoides conglobatus</i>	<i>Globorotalia menardii</i> (dex)	<i>Globorotalia scitula</i> (dex)	<i>Globorotalia scitula</i> (sin)	<i>Globoturborotalita tenella</i>	<i>Neogloboquadrina atlantica</i> (dex)	<i>Neogloboquadrina pachyderma</i> (dex)	<i>Neogloboquadrina pachyderma</i> (sin)	<i>Orbulina universa</i>	<i>Pulleniatina obliquiloculata</i>
339-U1388A-1H-CC	3.59	3.64	B	R	VG	F	R	R	F	D	P		P	A		P						R							P	F		
339-U1388B-2X-CC	7.70	7.73	B	D	VG	F	R			A			R	R		P					P	P					P	F	F	P		
3X-CC	17.70	17.73	B	P	VG	F	A		R	A		P															A	F				
4X-CC	28.95	29.00	B	P	M	A				F																	A	P				
5X-CC	36.45	36.50	B	P																												
6X-CC	47.42	47.47	B	B																												
7X-CC	56.09	56.14	B	P	VG																											
8X-CC	63.30	63.40	B	P	VG	D	P			P											P						A					
9X-CC	74.13	74.18	B	B																												
10X-CC	85.87	85.92	B	D	VG	A			F		P	R				P	P	P								A	P	R				
11X-1	92.01	92.06	B	P	VG	F	R		D			P	A													R	R	F				
12X-CC	101.71	101.76	B	A	VG	A	P		F				R					P	P							A	P	F	R			
13X-CC	120.66	120.71	B	A	VG	A												P	P	P	R					D	P		F			
14X-CC	130.14	130.19	B	R	G	A	P		F																	D	P					
15X-CC	139.81	139.86	B	A	G	A	P		F				R					P	P	P						D	P		P			
16X-CC	149.27	149.32	B	A	G	A	P		F									P	P	P	R					A	P	R	P			
17X-CC	151.74	151.79	B	P	M	A	R		F				R													A		R	P	P		
18X-CC	162.77	162.82	B	P																												
19X-CC	177.97	178.02	B	R	M	F	R		F												P						D	P	R			
20X-CC	185.85	185.91	B	A	G	A	R		F				P						P	P							A	R				
21X-CC	188.61	188.66	B	P	G	F	P		A														P				A					
22X-CC	198.99	199.04	R	F	VG	A	R		A			P		P					P	R	P						A	P	P			
23X-CC	211.80	211.87	B	A	VG	D	F		F										P	R							F	R	P	P		
24X-CC	225.68	225.73	B	A	VG	A	F		P	A	P																A	P	R	P	P	
339-U1388C-2R-CC	206.38	206.43	B	D	G	A	R		F					R							P	P					D	R	P			
339-U1388C-3R-CC	222.50	222.55	B	D	G	A	R		F				P	P							P	P					A	R	P			

Abundance: D = dominant, A = abundant, F = few, P = present, R = rare, B = barren. Preservation: VG = very good, G = good, M = moderate. sin = sinistral, dex = dextral. See “Biostratigraphy” in the “Methods” chapter (Expedition 339 Scientists, 2013b) for abundance and preservation definitions.



Table T7. Abundance of benthic foraminifers, Site U1388. (Continued on next two pages.)

Core, section	Depth (mbsf)		Preservation	Abundance	<i>Ammonia beccarii</i>	<i>Amphicoryna scalaris</i>	<i>Anomalinoidea</i> spp.	<i>Asterigerinata planorbis</i>	<i>Astrononion</i> spp.	<i>Bigenerina nodosaria</i>	<i>Biloculinella</i> spp.	<i>Bolivina cf. robusta</i>	<i>Bolivina/Brizalina</i> spp.	<i>Brizalina alata</i>	<i>Brizalina dilatata</i>	<i>Brizalina spathulata</i>	<i>Bulimina aculeata</i>	<i>Bulimina elongata</i>	<i>Bulimina gibba</i>	<i>Bulimina marginata</i>	<i>Bulimina striata</i> gr.	<i>Bulimina</i> spp.	<i>Buliminella elegantissima</i>	<i>Cassidulina laevigata/teretis</i>	<i>Cassidulina</i> spp.	<i>Cibicides lobatulus</i>	<i>Cibicides cf. lobatulus</i>	<i>Cibicides refugens</i>	<i>Cibicides kullenbergi</i>	<i>Cibicides pachyderma</i>	<i>Cibicides wuellerstorfi</i>	<i>Cibicides/Cibicides</i> spp.	<i>Dentalina</i> spp.	<i>Ehrenbergina</i> spp.	Elphidid taxa	<i>Elphidium crispum</i>	<i>Elphidium cf. jensei</i>	<i>Elphidium</i> spp.	<i>Epistominella</i> spp.	<i>Fissurina</i> spp.	<i>Fursenkoina</i> spp.	<i>Gavelinopsis?</i> sp.	<i>Globobulimina affinis</i>	<i>Globobulimina spinescens</i>						
	Top	Bottom																																																
339-U1388A-1H-CC	3.59	3.64	G	R	F	P							P		P			R		P		F			A	P		R	F				R	F																
339-U1388B-2X-CC	7.70	7.73	G	A						P					P	P	P			P		F				R		F	R														P	R						
3X-CC	17.70	17.73	M	F	P										R	P						F				D		F	R		P			F	R							R	P							
4X-CC	28.95	29.00	P	R	R												P											R																						
5X-CC	36.45	36.50	P	B																																														
6X-CC	47.42	47.47	M-P	R																R					P										R															
7X-CC	56.09	56.14	P	R	A																							R		A				R																
8X-CC	63.30	63.40	M-P	R	R			P					R													R	R																			P				
9X-CC	74.13	74.18	P	B																								R																						
10X-CC	85.87	85.92	G	A					P	R	P	R	P	R	R	R				R		F				R		F	R																P	R				
11X-1	92.01	92.06	M	R	R																	P				R																								
12X-CC	110.88	110.93	G	D	P								R	R	D	P	P											F	R																	P	P			P
13X-CC	120.66	120.71	G	A	P									R	R	R						R								P	P																	P	R	
14X-CC	130.14	130.19	G	F	P								A	R	A	P	P									R																								
15X-CC	139.81	139.86	G	F	R		P						R		F	P	P					P						R																						
16X-CC	149.27	149.32	G	A	R			P					R	R	P	R	R					P	P				F	P																						
17X-CC	151.74	151.79	G	F				P					R	R	R	P	R																																	
18X-CC	162.77	162.82	P	B																																														
19X-CC	177.97	178.02	G	A					P	P	P	F	R		R													F	R																					
20X-CC	185.85	185.91	G	D									P	R	A		R	P																																
21X-CC	188.61	188.66	G	R																																														
22X-CC	198.99	199.04	G	A	P		P						R		R																																			
23X-CC	211.80	211.87	G	A	P								F	P	R		P	R	R																															
24X-CC	225.68	225.73	M	A									R	P	R		F	R																																
339-U1388C-2R-CC	206.38	206.43	G	A									R		R																																			
3R-CC	222.50	222.55	M	A			P						R		R		A																																	
4R-1	224.93	224.98	M	R	R												P																																	

Preservation: G = good, M = moderate, P = poor. Abundance: D = dominant, A = abundant, F = few, P = present, R = rare, B = barren. See "Biostratigraphy" in the "Methods" chapter (Expedition 339 Scientists, 2013b) for abundance and preservation definitions.



Table T7 (continued).

Core, section	Depth (mbsf)		Preservation	Abundance	<i>Textularia</i> spp.	<i>Trifarina angulosa</i>	<i>Trifarina bradyi</i>	<i>Trifarina</i> spp.	<i>Triloculina</i> spp.	<i>Uvigerina mediterranea</i>	<i>Uvigerina peregrina</i>	<i>Uvigerina</i> spp.	<i>Valulina</i> spp.	<i>Valvulinera</i> spp.
	Top	Bottom												
339-U1 388A-1H-CC	3.59	3.64	G	R	P	R					R	R		
339-U1 388B-2X-CC	7.70	7.73	G	A	R	R					R	R		
3X-CC	17.70	17.73	M	F	P	F					R	P		
4X-CC	28.95	29.00	P	R								P		
5X-CC	36.45	36.50	P	B										
6X-CC	47.42	47.47	M-P	R							R	R		
7X-CC	56.09	56.14	P	R	R	R					F			
8X-CC	63.30	63.40	M-P	R		P							P	
9X-CC	74.13	74.18	P	B										
10X-CC	85.87	85.92	G	A						F	P	F		
11X-1	92.01	92.06	M	R		P				P				
12X-CC	110.88	110.93	G	D		P				R	R	F		
13X-CC	120.66	120.71	G	A		F	P							
14X-CC	130.14	130.19	G	F						R			P	
15X-CC	139.81	139.86	G	F		R					P			
16X-CC	149.27	149.32	G	A										R
17X-CC	151.74	151.79	G	F			P							P
18X-CC	162.77	162.82	P	B										
19X-CC	177.97	178.02	G	A							R			
20X-CC	185.85	185.91	G	D										
21X-CC	188.61	188.66	G	R										
22X-CC	198.99	199.04	G	A		F					R		P	
23X-CC	211.80	211.87	G	A	P									R
24X-CC	225.68	225.73	M	A	P	R		R		A	R	R		
339-U1 388C-2R-CC	206.38	206.43	G	A		P				F		F		
3R-CC	222.50	222.55	M	A		P						F		
4R-1	224.93	224.98	M	R	R	R				R				P

Table T8. Abundance of pollen and spores, Hole U1388B.

Core, section	Depth (mbsf)		Preservation	Abundance	Broken	Corroded	Crumpled	Unknown taxa	Alnus	Anthemis type	Apiaceae	Artemisia	Aster type	Brassicaceae	Centauria nigra type	Chenopodiaceae	Cyperaceae	Exotic counted	Ephedra distachya type	Ephedra fragilis type	Ericaceae	Isoetes	Olea	Pinus	Plantago	Plumbaginaceae	Poaceae	Quercus deciduous type	Quercus evergreen type	Taraxacum	Unidentifiables	
	Top	Bottom																														
339-U1388B-2X-CC	7.70	7.73	P	A		9			F	F	F	F																				
14X-CC	130.14	130.19	M	A	2	14	2	1		C	F	A	C	F	F	A	C	69	F	F	C	C	C	C	F	C	C	F	F	A	C	

Preservation: M = moderate, P = poor. Abundance: A = abundant, C = common, F = few. See "Biostratigraphy" in the "Methods" chapter (Expedition 339 Scientists, 2013b) for abundance and preservation definitions.

Table T9. Core disturbance intervals, Site U1388.

Core, section	Offset of disturbed interval (cm)		Type of disturbance
	Top	Bottom	
339-U1388A-1A-1	0	70	Core top/Soupy
1A-2	125	135	IW
339-U1388B-6X-1	145	150	IW
7X-1	0	65	Disturbed
10X-1	145	150	IW
12X-4	145	150	IW
13X-6	145	150	IW
14X-5	145	150	IW
15X-5	145	150	IW
16X-5	145	150	IW
17X-1	0	20	Core top
17X-1	145	150	IW
18X-1	0	10	Core top
18X-1	145	150	IW
19X-6	125	135	IW
20X-1	0	10	Core top
20X-5	125	130	IW
21X-1	0	17	Core top
22X-1	0	5	Core top
23X-3	140	145	IW
339-U1388C-2R-1	0	15	Core top

IW = interstitial water sample.



Table T10. NRM inclination, declination, and intensity data after 20 mT peak field AF demagnetization, Hole U1388A. (Continued on next page.)

Core, section, interval (cm)	Depth (mbsf)	Inclination (°)	Declination (°)	Flexit- corrected declination (°)	Intensity (A/m)
339-U1388A-					
1H-1	0.00				
1H-1, 5	0.05				
1H-1, 10	0.10				
1H-1, 15	0.15	-65.1	218.7		0.00106
1H-1, 20	0.20	-67.1	229.3		0.001155
1H-1, 25	0.25	-68.7	237.2		0.001306
1H-1, 30	0.30	-72.7	277.8		0.001199
1H-1, 35	0.35	-69.2	339.7		0.0007429
1H-1, 40	0.40	-72.6	40.1		0.0003739
1H-1, 45	0.45	-57.4	19.5		0.000595
1H-1, 50	0.50	-49.1	321.3		0.0007535
1H-1, 55	0.55	-13.4	335.7		0.0006154
1H-1, 60	0.60	13.3	321.6		0.0004347
1H-1, 65	0.65	76.1	226.2		0.0001293
1H-1, 70	0.70	42.2	67		0.0002901
1H-1, 75	0.75	44.3	88.9		0.0005917
1H-1, 80	0.80	80.2	57.9		0.001829
1H-1, 85	0.85	48.5	291.8		0.003722
1H-1, 90	0.90	23.5	283		0.001729
1H-1, 95	0.95	17.7	218.6		0.000453
1H-1, 100	1.00	-12.9	229.8		0.0003069
1H-1, 105	1.05	-2.5	234.5		0.0002894
1H-1, 110	1.10	35.4	112.2		0.000222
1H-1, 115	1.15	30.4	126.9		0.0002784
1H-1, 120	1.20	15.5	129.3		0.0002311
1H-1, 125	1.25	17.1	167.4		0.0001011
1H-1, 130	1.30	37	273.8		0.0002429
1H-1, 135	1.35	77.9	286.5		0.0003679
1H-1, 140	1.40				
1H-1, 145	1.45				
1H-1, 150	1.50				
1H-2	1.50				
1H-2, 5	1.55				
1H-2, 10	1.60				
1H-2, 15	1.65	73.9	281.1		0.0005715
1H-2, 20	1.70	56	283		0.0005796
1H-2, 25	1.75	60.6	274.6		0.0005386
1H-2, 30	1.80	44.5	261.5		0.0007555
1H-2, 35	1.85	47.6	257		0.0009471
1H-2, 40	1.90	76	219.5		0.0009221
1H-2, 45	1.95	61.6	272.9		0.001032
1H-2, 50	2.00	74.8	240.6		0.00101
1H-2, 55	2.05	66.5	206.9		0.0008087
1H-2, 60	2.10	42.3	246.4		0.0007146
1H-2, 65	2.15	50	207.9		0.0007026
1H-2, 70	2.20	61.8	176.1		0.0006899
1H-2, 75	2.25	51.3	256.6		0.0008523
1H-2, 80	2.30	25.9	271.3		0.001523
1H-2, 85	2.35	37.2	263.1		0.0009578
1H-2, 90	2.40	44	180.7		0.0007373
1H-2, 95	2.45	40.8	194.3		0.0009692
1H-2, 100	2.50	56.2	157.7		0.0008753
1H-2, 105	2.55	71.1	174.9		0.000762
1H-2, 110	2.60	62.7	224.8		0.000684
1H-2, 115	2.65	62.8	165.8		0.0004401
1H-2, 120	2.70				
1H-2, 125	2.75				
1H-2, 130	2.80				
1H-3	2.81				
1H-3, 5	2.86				
1H-3, 10	2.91				
1H-3, 15	2.96	54.6	215.8		0.0004363
1H-3, 20	3.01	37.6	220.4		0.0005674
1H-3, 25	3.06	36.6	214.9		0.0004845
1H-3, 30	3.11	45.3	209.7		0.0005455

Table T10 (continued).

Core, section, interval (cm)	Depth (mbsf)	Inclination (°)	Declination (°)	FlexIt-corrected declination (°)	Intensity (A/m)
1H-3, 35	3.16	33.9	253.1		0.0006703
1H-3, 40	3.21	25.8	264.2		0.0003908
1H-3, 45	3.26	60.4	13.9		7.78E-05
1H-3, 50	3.31				
1H-3, 55	3.36				
1H-3, 60	3.41				

Blank cells indicate depth levels where data were either not available (i.e., FlexIt-corrected declination data for nonoriented cores) or removed because of disturbance, voids, or measurement edge effects.

Table T11. NRM inclination, declination, and intensity data after 20 mT peak field AF demagnetization, Hole U1388B. (Continued on next page.)

Core, section, interval (cm)	Depth (mbsf)	Inclination (°)	Declination (°)	FlexIt-corrected declination (°)	Intensity (A/m)
339-U1388B-					
4X-1	26.50				
4X-1, 5	26.55				
4X-1, 10	26.60				
4X-1, 15	26.65	72.3	349.6		0.009223
4X-1, 20	26.70	77.8	310.4		0.015849
4X-1, 25	26.75	71.7	87.4		0.022768
4X-1, 30	26.80	58.1	78.8		0.025235
4X-1, 35	26.85	43.7	49.9		0.028365
4X-1, 40	26.90	46.1	33		0.02617
4X-1, 45	26.95	47.2	30.9		0.025975
4X-1, 50	27.00	46.9	31.9		0.024234
4X-1, 55	27.05	44.3	36.4		0.023023
4X-1, 60	27.10	43.7	36.1		0.020811
4X-1, 65	27.15	31.9	39.7		0.024083
4X-1, 70	27.20	32.5	34		0.024716
4X-1, 75	27.25	39.3	27		0.020611
4X-1, 80	27.30	40.6	34.1		0.018564
4X-1, 85	27.35	38.1	40.9		0.020521
4X-1, 90	27.40	41.9	36.7		0.018249
4X-1, 95	27.45	46.7	50.1		0.014409
4X-1, 100	27.50	44.1	54.2		0.013357
4X-1, 105	27.55	52	28.6		0.006898
4X-1, 110	27.60	-71.7	129.6		0.003728
4X-1, 115	27.65	-45.3	95.8		0.012772
4X-1, 120	27.70	-50.4	63.5		0.006727
4X-1, 125	27.75	48.2	4.7		0.004267
4X-1, 130	27.80	52.9	38.4		0.016958
4X-1, 135	27.85	49.8	45.2		0.026873
4X-1, 140	27.90				
4X-1, 145	27.95				
4X-1, 150	28.00				
4X-2	28.00				
4X-2, 5	28.05				
4X-2, 10	28.10				
4X-2, 15	28.15	44.5	41.7		0.02283
4X-2, 20	28.20	48.9	45.7		0.021379
4X-2, 25	28.25	41.8	44.3		0.021577
4X-2, 30	28.30	39.5	43.4		0.020019
4X-2, 35	28.35	42.9	45		0.017474
4X-2, 40	28.40	43.8	46.7		0.017344
4X-2, 45	28.45	42.6	38.7		0.023387
4X-2, 50	28.50	65.4	29		0.027221
4X-2, 55	28.55				
4X-2, 60	28.60				
4X-2, 65	28.65				

Table T11 (continued).

Core, section, interval (cm)	Depth (mbsf)	Inclination (°)	Declination (°)	FlexIt-corrected declination (°)	Intensity (A/m)
5X-1	35.60				
5X-1, 5	35.65				
5X-1, 10	35.70				
5X-1, 15	35.75	46	72.2		0.004513
5X-1, 20	35.80	45.4	59.2		0.007596
5X-1, 25	35.85	72.6	73		0.013891
5X-1, 30	35.90				
5X-1, 35	35.95				
5X-1, 40	36.00				
6X-1	45.00				
6X-1, 5	45.05				
6X-1, 10	45.10				
6X-1, 15	45.15	61.6	53.9		0.034468

Blank cells indicate depth levels where data were either not available (i.e., FlexIt-corrected declination data for nonoriented cores) or removed because of disturbance, voids, or measurement edge effects. Only a portion of this table appears here. The complete table is available in [ASCII](#).

Table T12. NRM inclination, declination, and intensity data after 20 mT peak field AF demagnetization, Hole U1388C. (Continued on next three pages.)

Core, section, interval (cm)	Depth (mbsf)	Inclination (°)	Declination (°)	FlexIt-corrected declination (°)	Intensity (A/m)
339-U1388C-					
2R-1	205				
2R-1, 5	205.05				
2R-1, 10	205.1				
2R-1, 15	205.15				
2R-1, 20	205.2	52.8	161.3		0.006113
2R-1, 25	205.25	59	164.5		0.003455
2R-1, 30	205.3	68.7	159.6		0.002239
2R-1, 35	205.35	66.1	144.5		0.002079
2R-1, 40	205.4	58.9	145.7		0.003044
2R-1, 45	205.45	54	156.2		0.003974
2R-1, 50	205.5	53.5	128.8		0.004299
2R-1, 55	205.55	51.2	70.5		0.004836
2R-1, 60	205.6	75.3	337		0.004742
2R-1, 65	205.65	63	237.3		0.006159
2R-1, 70	205.7	59.3	209.4		0.006805
2R-1, 75	205.75	78.7	8.2		0.004972
2R-1, 80	205.8	57.3	337.9		0.006745
2R-1, 85	205.85	51.8	284.7		0.007943
2R-1, 90	205.9	53.2	269.5		0.007954
2R-1, 95	205.95	56.4	267.6		0.005534
2R-1, 100	206	64.4	272.4		0.003558
2R-1, 105	206.05	65.4	272.4		0.002657
2R-1, 110	206.1	64.5	271.5		0.002577
2R-1, 115	206.15	60.1	272.5		0.002649
2R-1, 120	206.2				
2R-1, 125	206.25				
2R-1, 130	206.3				
3R-1	214.5				
3R-1, 5	214.55				
3R-1, 10	214.6				
3R-1, 15	214.65	65.5	31.1		0.015627
3R-1, 20	214.7	81.7	213.5		0.00576
3R-1, 25	214.75	86.8	343.3		0.002888
3R-1, 30	214.8	66.6	105.3		0.002958
3R-1, 35	214.85	56.5	52.5		0.00323
3R-1, 40	214.9	64.7	358.3		0.00264
3R-1, 45	214.95	65.6	113.5		0.002335
3R-1, 50	215	68.6	114.6		0.002412

Table T12 (continued). (Continued on next page.)

Core, section, interval (cm)	Depth (mbsf)	Inclination (°)	Declination (°)	Flexlt- corrected declination (°)	Intensity (A/m)
3R-1, 55	215.05	81.1	286.5		0.002168
3R-1, 60	215.1	88.6	21.2		0.002097
3R-1, 65	215.15	74	215.5		0.002238
3R-1, 70	215.2	74.6	313.7		0.002255
3R-1, 75	215.25	60.8	19.2		0.00245
3R-1, 80	215.3	69.4	149.8		0.002166
3R-1, 85	215.35	58.1	164.1		0.002084
3R-1, 90	215.4	61.5	84.2		0.002159
3R-1, 95	215.45	52.2	44.3		0.002581
3R-1, 100	215.5	53.2	63.6		0.002613
3R-1, 105	215.55	66.6	56		0.002327
3R-1, 110	215.6	71.7	296.7		0.002228
3R-1, 115	215.65	66.4	309.7		0.002383
3R-1, 120	215.7	87	332		0.002199
3R-1, 125	215.75	85.8	200		0.002142
3R-1, 130	215.8	76.1	33		0.001984
3R-1, 135	215.85	59.6	31.3		0.002324
3R-1, 140	215.9				
3R-1, 145	215.95				
3R-1, 150	216				
3R-2	216				
3R-2, 5	216.05				
3R-2, 10	216.1				
3R-2, 15	216.15	43.9	140.3		0.01508
3R-2, 20	216.2	72.5	163.1		0.004552
3R-2, 25	216.25	45.2	352.2		0.002944
3R-2, 30	216.3	56.3	10.8		0.002771
3R-2, 35	216.35	77.3	226.3		0.003549
3R-2, 40	216.4	64.9	198.1		0.003315
3R-2, 45	216.45	60.3	137.4		0.003296
3R-2, 50	216.5	63.3	78		0.003034
3R-2, 55	216.55	65.5	348.5		0.00322
3R-2, 60	216.6	75.5	0.5		0.003568
3R-2, 65	216.65	71.9	111.4		0.003533
3R-2, 70	216.7	80.3	170.4		0.00334
3R-2, 75	216.75	83.5	194.9		0.003287
3R-2, 80	216.8	78.3	92.2		0.003007
3R-2, 85	216.85	75.5	150		0.00327
3R-2, 90	216.9	68.6	52.1		0.004968
3R-2, 95	216.95	56	45.3		0.006993
3R-2, 100	217	82.7	49.1		0.005678
3R-2, 105	217.05	71.8	150.9		0.005147
3R-2, 110	217.1	63.3	171.9		0.002984
3R-2, 115	217.15	60.1	217.3		0.001742
3R-2, 120	217.2	63.5	208.2		0.001979
3R-2, 125	217.25	65.6	174.4		0.002879
3R-2, 130	217.3	68	108.2		0.002808
3R-2, 135	217.35	72.2	83		0.003027
3R-2, 140	217.4				
3R-2, 145	217.45				
3R-2, 150	217.5				
3R-3	217.5				
3R-3, 5	217.55				
3R-3, 10	217.6				
3R-3, 15	217.65	66.4	12.7		0.013542
3R-3, 20	217.7	76.1	8.3		0.0088
3R-3, 25	217.75	58	277.7		0.00578
3R-3, 30	217.8	50.9	276.5		0.003401
3R-3, 35	217.85	77.2	163.6		0.002219
3R-3, 40	217.9	72.5	170.2		0.002274
3R-3, 45	217.95	77.2	233.4		0.002074
3R-3, 50	218	77.8	275.7		0.002143
3R-3, 55	218.05	72.6	44.3		0.00222
3R-3, 60	218.1	69.1	13.8		0.00224
3R-3, 65	218.15	73.1	201.4		0.0022
3R-3, 70	218.2	57.7	166.7		0.002153
3R-3, 75	218.25	25.3	99.2		0.004379

Table T12 (continued). (Continued on next page.)

Core, section, interval (cm)	Depth (mbsf)	Inclination (°)	Declination (°)	Flexlt- corrected declination (°)	Intensity (A/m)
3R-3, 80	218.3	36.8	101.7		0.008139
3R-3, 85	218.35	30.7	263.7		0.062123
3R-3, 90	218.4	64.4	272.7		0.1816
3R-3, 95	218.45	30.4	85.1		0.23199
3R-3, 100	218.5	50.2	79.7		0.023829
3R-3, 105	218.55	9.7	268.3		0.015791
3R-3, 110	218.6	13.7	266.9		0.006775
3R-3, 115	218.65	26.9	266.7		0.003543
3R-3, 120	218.7	34.5	272.6		0.002633
3R-3, 125	218.75	43.3	279.7		0.001884
3R-3, 130	218.8	73.4	238.7		0.001282
3R-3, 135	218.85	74.4	232.4		0.001212
3R-3, 140	218.9				
3R-3, 145	218.95				
3R-3, 150	219				
3R-4	219				
3R-4, 5	219.05				
3R-4, 10	219.1				
3R-4, 15	219.15	59.8	64.3		0.001646
3R-4, 20	219.2	63	22.4		0.001583
3R-4, 25	219.25	71.1	320.1		0.001501
3R-4, 30	219.3	68.6	272.1		0.001448
3R-4, 35	219.35	71.4	265.9		0.001247
3R-4, 40	219.4	63	169.8		0.001236
3R-4, 45	219.45	55.7	163.5		0.001534
3R-4, 50	219.5	62	153.2		0.001674
3R-4, 55	219.55	68.5	79		0.001568
3R-4, 60	219.6	77.2	81.5		0.001443
3R-4, 65	219.65	66.6	133.4		0.001414
3R-4, 70	219.7	75.5	201.3		0.001272
3R-4, 75	219.75	62	255.8		0.00145
3R-4, 80	219.8	59.4	257.4		0.001574
3R-4, 85	219.85	67.8	239.7		0.001338
3R-4, 90	219.9	73	290.9		0.0007623
3R-4, 95	219.95	16.2	55.3		0.001548
3R-4, 100	220	38.9	53.7		0.001183
3R-4, 105	220.05	67.6	298.7		0.0008144
3R-4, 110	220.1	83.7	199.4		0.0006512
3R-4, 115	220.15	60.5	116.2		0.0006556
3R-4, 120	220.2	70.5	69.4		0.0005905
3R-4, 125	220.25	58.2	47.6		0.0007036
3R-4, 130	220.3	57.1	106.3		0.0007686
3R-4, 135	220.35	60.2	131.6		0.0008902
3R-4, 140	220.4				
3R-4, 145	220.45				
3R-4, 150	220.5				
3R-5	220.5				
3R-5, 5	220.55				
3R-5, 10	220.6				
3R-5, 15	220.65	64.4	304.2		0.001152
3R-5, 20	220.7	64.9	165.7		0.001439
3R-5, 25	220.75	72.3	113.4		0.001456
3R-5, 30	220.8	77.5	278.3		0.001205
3R-5, 35	220.85	74.5	168.5		0.001182
3R-5, 40	220.9	60.1	129		0.001133
3R-5, 45	220.95	63.1	75		0.001013
3R-5, 50	221	75.3	47.8		0.0009846
3R-5, 55	221.05	73.4	154.4		0.001092
3R-5, 60	221.1	78	87.4		0.001118
3R-5, 65	221.15	77.7	316.5		0.001096
3R-5, 70	221.2	59.6	330.5		0.001158
3R-5, 75	221.25	55.1	39		0.001208
3R-5, 80	221.3	64.4	49.5		0.00163
3R-5, 85	221.35	68.8	1.3		0.002857
3R-5, 90	221.4	73.4	298.8		0.003582
3R-5, 95	221.45	75.1	127.6		0.004156
3R-5, 100	221.5	53	90.4		0.006232

Table T12 (continued).

Core, section, interval (cm)	Depth (mbsf)	Inclination (°)	Declination (°)	FlexIt-corrected declination (°)	Intensity (A/m)
3R-5, 105	221.55	43.4	92.6		0.005559
3R-5, 110	221.6	72.9	62.5		0.001631
3R-5, 115	221.65	41.3	303.4		0.001008
3R-5, 120	221.7	42.8	290.3		0.0004953
3R-6	221.71	73.4	296.7		0.0002426
3R-6, 5	221.76	67.1	217.8		0.000453
3R-6, 10	221.81	76.4	211.6		0.0004401
3R-6, 15	221.86	80.6	181.6		0.0004908
3R-6, 20	221.91	61.2	73.6		0.0007777
3R-6, 25	221.96	63.8	43		0.0007902
3R-6, 30	222.01	71.3	13.4		0.0007286
3R-6, 35	222.06	55.6	349		0.000904
3R-6, 40	222.11	82.6	7.3		0.0008267
3R-6, 45	222.16	61.2	152.7		0.00102
3R-6, 50	222.21	80.4	159.4		0.0009486
3R-6, 55	222.26	59.2	74.5		0.001061
3R-6, 60	222.31				
3R-6, 65	222.36				
3R-6, 70	222.41				
4R-1	224.1				
4R-1, 5	224.15				
4R-1, 10	224.2				
4R-1, 15	224.25	55.2	123.8		0.003917
4R-1, 20	224.3	63.6	130.4		0.003991
4R-1, 25	224.35	59	127.9		0.00445
4R-1, 30	224.4	55.8	127.9		0.004817
4R-1, 35	224.45	59	122.3		0.00454
4R-1, 40	224.5	50.5	112.6		0.005126
4R-1, 45	224.55	54.2	111.6		0.005309
4R-1, 50	224.6	71.9	268.8		0.005094
4R-1, 55	224.65	50.3	268.1		0.006325
4R-1, 60	224.7	49.7	267.8		0.006163
4R-1, 65	224.75	52.7	262		0.005771
4R-1, 70	224.8	60.8	171.8		0.004622
4R-1, 75	224.85				
4R-1, 80	224.9				
4R-1, 85	224.95				

Blank cells indicate depth levels where data were either not available (i.e., FlexIt-corrected declination data for nonoriented cores) or removed because of disturbance, voids, or measurement edge effects.

Table T13. Headspace sample hydrocarbon concentrations, Holes U1388A–U1388C.

Core, section	Depth (mbsf)	Concentration (ppmv)		
		Methane	Ethene	Ethane
339-U1388A-1H-3	2.81	10.38	—	—
339-U1388B-4X-2	28.00	4.19	—	—
6X-2	46.50	1,796.75	—	—
9X-1	73.68	12,071.15	—	—
10X-2	83.60	26,685.56	—	0.92
12X-5	107.30	50,377.78	—	1.12
13X-7	118.56	54,833.61	—	1.27
14X-6	127.90	35,916.65	—	1.29
15X-6	137.40	26,584.37	—	0.93
16X-6	147.00	36,265.22	0.65	1.45
17X-2	150.60	41,816.47	0.69	1.64
18X-2	160.10	65,682.64	0.82	2.75
19X-7	177.00	15,084.71	0.57	1.02
20X-6	185.07	16,709.09	—	1.40
21X-1	187.40	5,414.54	—	—
22X-2	198.25	6,943.99	0.81	0.99
23X-4	211.00	7,981.99	—	1.04
24X-7	224.81	6,738.78	—	0.82
339-U1388C-3R-6	221.71	4,861.44	0.71	1.49

— = no data.

Table T14. Results from coulometric and CHNS analysis on whole-round squeezecake samples, Holes U1388A–U1388C.

Core, section	Depth (mbsf)	CaCO ₃ (wt%)	Inorganic carbon (wt%)	Total carbon (wt%)	Nitrogen (wt%)	Organic carbon (wt%)	C/N
339-U1388A-1H-2	2.65	30.100	3.609	3.69	0.02	0.08	4.0
339-U1388B-4X-2	28.50	29.089	3.488	3.87	0.05	0.38	7.6
5X-CC	36.34	26.462	3.173	3.49	0.02	0.32	16.0
6X-2	46.98	17.988	2.157	2.78	0.08	0.62	7.8
7X-1	55.34	21.064	2.526	3.28	0.09	0.75	8.3
9X-1	73.61	20.974	2.515	3.27	0.08	0.76	9.5
10X-2	84.57	29.894	3.584	4.24	0.06	0.66	11.0
12X-4	107.11	25.953	3.112	3.66	0.08	0.55	6.9
13X-6	117.93	26.657	3.196	3.48	0.06	0.28	4.7
14X-6	129.06	24.925	2.988	3.61	0.06	0.62	10.3
15X-6	138.70	24.589	2.948	3.37	0.06	0.42	7.0
16X-5	146.83	25.835	3.097	3.65	0.08	0.55	6.9
18X-2	160.90	24.614	2.951	3.72	0.09	0.77	8.6
19X-6	176.89	29.753	3.567	4.49	0.10	0.92	9.2
20X-6	185.57	22.484	2.696	3.21	0.09	0.51	5.7
21X-CC	188.37	23.636	2.834	3.39	0.09	0.56	6.2
22X-1	198.06	29.736	3.565	4.10	0.06	0.53	8.8
23X-3	210.75	22.389	2.684	3.35	0.11	0.67	6.1
24X-5	223.41	20.551	2.464	3.27	0.13	0.81	6.2
339-U1388C-3R-4	220.14	20.689	2.481	3.09	0.11	0.61	5.5
4R-1	224.74	22.835	2.738	3.46	0.11	0.72	6.5

Table T15. Interstitial water major and trace elements, Site U1388.

Core, section, interval (cm)	Depth (mbsf)	Alkalinity (meq/L) TITRA_AUTO	NH ₄ ⁺ (μM) SPEC	B (μM) 208.956 nm ICPAES	Ba (μM) 455.403 nm ICPAES	Ca ²⁺ (mM) IC	Cl ⁻ (mM) TITRA_AUTO	Fe (μM) 239.563 nm ICPAES	Li (μM) 670.784 nm ICPAES	Mg ²⁺ (mM) IC	pH ISE	K ⁺ (mM) IC	Si (μM) 288.158 nm ICPAES	Na ⁺ (mM) IC	Sr (μM) 421.552 nm ICPAES	SO ₄ ²⁻ (mM) IC
339-U1388A- 1H-2, 126–131	2.76	4.7	378	490.0		12.6	585.6	0.8	55.3	55.5	8.2	11.9	113.5	510.8	95.5	29.3
339-U1388B- 6X-1, 145–150	46.45	6.2	3863	493.5	19.7	4.5	640.8	1.7	35.0	36.4	7.8	7.4	166.8	524.0	92.1	0.0
9X-1, 123–128	73.73	6.1	4585	455.8	31.8	6.7	683.3	1.4	32.8	42.2	7.8	8.1	236.1	632.7	93.2	0.0
10X-1, 146–151	83.56	6.6	5267	461.3	37.7	5.5	663.1	0.8	40.2	38.3	7.9	7.0	347.0	566.0	101.8	0.0
12X-4, 145–150	107.25	6.4	6063	348.3	52.5	6.1	673.4	1.5	46.6	37.0	7.8	6.8	256.8	552.5	109.5	0.0
13X-6, 145–150	118.51	5.8	5913	347.1	56.9	6.6	668.6	1.9	43.3	37.4	8.0	6.8	253.8	570.4	114.5	0.0
14X-5, 145–150	127.85	4.9	6352	329.8	52.8	6.9	684.3	1.3	38.8	37.5	8.0	6.6	179.0	578.6	112.4	0.0
16X-5, 145–150	146.95	4.8	7671	322.3	39.0	6.3	704.9	2.8	38.4	37.5	7.8	6.7	192.9	590.3	107.0	0.0
17X-1, 145–150	150.55	5.2	7555	324.7	35.0	6.7	690.6	1.2	41.8	40.6	7.8	6.5	250.7	615.8	112.6	0.0
18X-1, 145–150	160.05	7.4	6701	235.7	26.7	7.7	736.2	15.6	47.4	43.4	7.7	6.1	539.6	619.0	114.5	0.0
19X-6, 125–130	176.95	9.2	8404	233.5	22.2	7.8	750.3	4.5	58.1	44.2	7.7	6.4	646.8	634.5	113.5	0.0
20X-5, 122–127	185.02	8.1	8183	209.8	19.7	7.7	761.0	2.5	57.0	46.1	7.8	6.6	362.0	654.2	114.7	0.0
23X-3, 140–145	210.90	6.8	7989	241.3	27.6	7.3	802.8	7.8	53.1	50.0	7.9	5.7	206.6	687.5	147.5	0.0

TITRA_AUTO = automatic titration, SPEC = spectrometer, IC = ion chromatograph, ICPAES = inductively coupled plasma–atomic emission spectrometer, ISE = ion-selective electrode.



Table T16. Interstitial water oxygen and hydrogen isotopes, Site U1388.

Core, section, interval (cm)	Depth (mbsf)	$\delta^{18}\text{O}$ (‰, VSMOW)	δD (‰, VSMOW)
339-U1388A- 1H-2, 126–131	2.81	0.78	6.47
339-U1388B-			
6X-1, 145–150	46.5	1.31	9.19
9X-1, 123–128	73.78	1.40	8.69
10X-1, 146–151	83.6	1.20	8.86
12X-4, 145–150	107.3	1.32	8.21
13X-6, 145–150	118.56	1.32	7.44
14X-5, 145–150	127.9	1.20	7.87
15X-5, 145–150	137.4	1.33	8.19
16X-5, 145–150	148.5	1.25	8.40
17X-1, 145–150	150.6	1.09	7.55
18X-1, 145–150	160.1	1.31	7.62
19X-6, 125–130	177	1.41	8.09
20X-5, 122–127	185.07	1.06	7.38
23X-3, 140–145	211	1.22	7.43

VSMOW = Vienna standard mean ocean water.